Stability and Control Derivatives Identification for an Unmanned Aerial Vehicle with Low Cost Sensors Using an Extended Kalman Filter Algorithm

By

Hady Benyamen

Submitted to the graduate degree program in Aerospace Engineering and the Graduate Faculty of the University of Kansas in partial fulfillment of the requirements for the degree of Master of Science.

Chair: Dr. Shawn Keshmiri

Dr. Ray Taghavi

Dr. Weizhang Huang

Date Defended: 30 January 2019

The thesis committee for Hady Benyamen certifies that this is the approved version of the following thesis:

Stability and Control Derivatives Identification for an Unmanned Aerial Vehicle with Low Cost Sensors Using an Extended Kalman Filter Algorithm

Chair: Dr. Shawn Keshmiri

Dr. Ray Taghavi

Dr. Weizhang Huang

Date Approved: 30 January 2019

Abstract

Unmanned aerial systems (UASs) tend to be autonomous vehicles. Thus, they require control algorithms. More advanced control algorithms can be developed when high quality UAS dynamic models are available. It is common to develop dynamic models for UAS using low fidelity theoretical methods. In this thesis, a higher fidelity approach which has been used for manned aircraft over the past 40-50 years is applied to the SkyHunter UAS. That approach is system identification. In this approach, the aircraft dynamic model is developed based on flight data. This thesis focuses particularly on identifying the longitudinal stability and control derivatives of the UAS. Such derivatives are important in developing UAS dynamic models.

An extended Kalman filter (EKF) algorithm was used to identify the derivatives. The algorithm is appealing since it can potentially allow online system identification. The SkyHunter analyzed in this thesis weighs about 10 lb. (4.5 kg) and its wing span is about 82 in (2 m.) Like many UASs, the SkyHunter uses relatively low-cost sensors. Therefore, the data contains high noise levels. Several flight portions from three different flights were analyzed and the results are presented. These flight portions were selected carefully based on criteria that make the flight data more suitable for system identification.

The identified derivatives showed reasonable results in several instances. However, a large degree of variation was observed when comparing derivatives identified from the different flight portions. The inconsistency is caused by unsteady aerodynamics, sensor noise, inability of the EKF to capture aircraft dynamics due to the use of simplified equations of motion, along with other reasons discussed in the thesis. The unsteady aerodynamics were investigated through: (A) Calculation of reduced frequency and (B) Measuring the effect of the propeller on empennage aerodynamics. This is relevant since the propeller is directly in front of the empennage.

Acknowledgments

I would like to extend my deep gratitude to Dr. Keshmiri. Thank you very much for all that you have done for me while working on this thesis and degree. I was truly blessed to have you as my advisor. I learned so much from you and from the opportunities you provided. I appreciate your genuine care, your understanding of aerospace engineering, your constant support and availability. You are not just an advisor and a teacher to me and to other students, but you are a father. What I write here is not enough to express my appreciation for you.

I want to thank Dr. Taghavi for his support during my master's degree and bachelor's degree. Thank you, Dr Taghavi, for serving on my committee. I also appreciate your guidance as my advisor during my undergraduate degree.

I want to thank you, Dr Huang, for serving on my committee and for teaching me differential equations.

To my team mates, Aaron B., Bella, Daksh, Grant, Thomas and Dustin, I enjoyed being with you these past years and I couldn't have finished this thesis without your work. It was fun to be with you and I learned many things from you.

To my parents, I could not have started nor finished this thesis without your continual support and encouragement. I deeply appreciate you and your never-ending support for me. I also want to thank my sister and her husband for their support and the fun they added to my life while working on this thesis. To my friends and family, thank you for your support during this past time.

Above all, I want to thank God for his grace, mercy and strength that allowed me to start, work on and finish this thesis.

Table of Contents

List of Figures

List of Tables

List of Acronyms

AAA	Advanced Aircraft Analysis
CFD	Computational Fluid Dynamics
CG	Center of Gravity
EKF	Extended Kalman Filter
IMU	Inertial Measurement Unit
KF	Kalman Filter
LTI	Linear time-invariant
RC	Radio Controlled
UAS	Unmanned Aerial System
UAV	Unmanned Aerial Vehicle
UKF	Unscented Kalman Filter
USD	United States Dollar
$\boldsymbol{\alpha\beta}$***-EKF***	Angle of attack and angle of side slip Extended Kalman Filter (Acronym points to the EKF used for estimating the air flow angles mentioned in Chapter 8)

1 Introduction

Different aircraft behave differently during flight. A large transport aircraft flies in a different manner than a fighter jet. A business jet flies in a different manner than a small unmanned aerial vehicle (UAV). Even two different transport aircraft fly differently. Things like the mass of the aircraft, the geometry of the wings, the distribution of mass in the aircraft, the type of propulsion, the shape of the control surfaces and many other factors affect how a certain aircraft behaves during flight. It is important to be able to understand how a certain aircraft flies. This topic is studied in depth in the field of flight dynamics.

Over the years, in flight dynamics, a common approach was developed to describe aircraft flight characteristics. That is to describe aircraft dynamics using stability and control derivatives. One of the early efforts in using this approach can be seen in the work of Bryan [1] in the early 20th century [2]. This approach can now be found in standard flight dynamics textbooks [3], [4].

These stability and control derivatives allow us to study how the forces and moments change during flight. For example, if the inclination of the aircraft with respect to the airflow changes by one degree, how much more lift force is generated? If the pilot commands a control surface to deflect an extra degree downwards, what is the additional moment that would be generated? These questions can be discussed using stability and control derivatives.

1.1 The SkyHunter: The UAS studied in this thesis

This thesis focuses on estimating the stability and control derivatives of the SkyHunter UAS. An image of the UAS is presented in the following figure. The University of Kansas Flight Systems Team owns several SkyHunter aircraft that it uses for research purposes. It is a commercially available UAS. Some modifications were made to the aircraft in house with the

purpose of improving its control and structural integrity. More information about the UAS is presented in Chapter 3 of the thesis.

Figure 1-1: The SkyHunter

1.2 Methods for estimating aircraft behavior

There are three well-known methods to estimating aircraft stability and control derivatives. These methods can be used to study aircraft dynamics in general not just to obtain stability and control derivatives. The methods are:

1) **Using theory.** This approach depends on physics-based modeling and some empirical data. This approach can be found in references such as [3]–[5]. In recent days, Computational Fluid Dynamics (CFD) have also added capabilities to this approach that make it more reliable [2]. Several programs are also available to obtain stability and control derivatives based on this approach such as [6], [7].
2) **Using wind tunnel experimentation**. By making small-scale models of the aircraft and placing them in the wind tunnel, it is possible to obtain stability and control derivatives of an aircraft.
3) **Using flight data.** This method depends on obtaining data from the aircraft sensors. Then based on this data it is possible to understand how an aircraft flies and how the forces

acting on the aircraft change. Textbooks that specifically address this methodology are available in References [8]–[11].

The first method has the advantage of being the least costly method of the three. Using software such as Advanced Aircraft Analysis [6], it is possible to obtain a full set of stability and control derivatives for an aircraft. Minimal experimentation is needed to use this method. In fact, it is possible to obtain stability and control derivatives for a conceptual aircraft for which no prototype exists. This method is therefore the only one available during early design stage. With that said, the method lacks accuracy and reliability compared to the second and third methods. The use of computational fluid dynamics (CFD) in recent years has added to the reliability of this theoretical method, however [2].

The second method is more expensive than the first one but can be less costly than the third method, at least in some cases. It provides higher accuracy than the first method [2]. However, wind tunnel testing can have several limitations arising from model scaling, Reynold's number, and the interaction between model support and the flow as mentioned in [2], [12]. Wind tunnel models can also be very expensive in some cases.

In this thesis, the third method is used. When it comes to using flight data to estimate stability and control derivatives, this method can be referred to as **aircraft system identification** or parameter identification. This third method requires having the aircraft already built and flight ready. The method has advantage that information is obtained from the actual aircraft not a theoretical model or a scaled down wind-tunnel model. With that said, flight testing also has its own limitations such as sensor inaccuracies, atmospheric disturbances, and higher risk associated with flight. Also, for large aircraft, it can be much more expensive to build an aircraft than to build a wind-tunnel model.

For UASs, evaluating the advantages and disadvantages of the second and third method is a bit different from large aircraft. This is because UASs are usually much cheaper to build than an actual aircraft. Also, since there is no human onboard a UAS, the risk of losing human life is reduced. These factors make flight testing of UASs appealing. However, the small size of the UAS make it possible to test in a wind tunnel without making a scaled model in some cases. Flight testing of UASs can also be difficult since the small size and weight of UASs makes them very susceptible to external disturbances from the environment.

With the above mentioned, it is important to note that all three methods for obtaining stability and control derivatives are useful and needed. The methods complement each other. It is good to use more than one method to validate the results obtained from the other. For example, comparing results from the system identification to wind tunnel results can help capture errors made in wind tunnel calculations, and vice versa [12].

Since this thesis focuses on the third method, it is important to note its specific importance. Even if the available dynamic models for a given aircraft based on theory and wind-tunnel tests are thorough, it is not possible to verify these models until flight test data is analyzed [13]. Despite "the most thorough wind-tunnel and analytical test program in history, the flight data for the space shuttle exhibited significant disagreements with preflight predictions" [12]. Using flight data allow us to see how the aircraft, in its final design performs in the air. This gives the third method a special appeal when it comes to studying aircraft dynamics.

1.3 System Identification as a field

While the term system identification was mentioned already in the previous discussion, it is worth stopping for a brief moment to talk about it. System identification is a field of study that goes beyond aerospace engineering. When considering a system (such as an aircraft) there are

three aspects relating to that system. These aspects are presented in the following figure. First, there is the **system** itself and its dynamics. This can be an aircraft, a car, a factory, the economy of the United States, etc. Then, there is the **input** that is given to that system. For example, a pilot command, pressing the car brake pedal, increasing the flow rate of a pipe, lowering the interest rate on bonds, etc. When this input is given to the system, the resultant is the **output** or the response of the system. Again, to complete the examples, the output can be, the aircraft starting to rotate upwards, the car slowing down, the concentration of a substance changing or a change in investor behavior, etc.

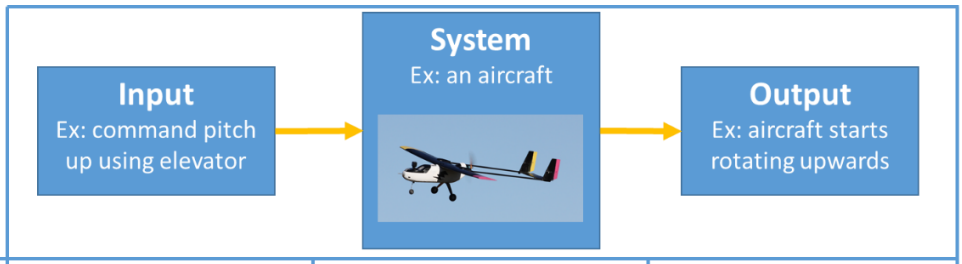

Control	Unknown	Known	Known
Simulation	Known	Known	Unknown
System Identification	Known	Unknown	Known

Figure 1-2: The three aspects to look at when studying a system and the three scenarios when studying the system.

With these three components in place, there can be three different scenarios in studying a system. In each of these cases two aspects relating to the system are known while the third one is unknown, and we are trying to know it. These three scenarios are presented in the last three rows of the previous diagram and are explained below.

1) **Control**: If we know how a system behaves (i.e. know its dynamics) and we know the output that we desire from that system. Then we want to **control** that system, for example, by commanding the aircraft or taking a certain action. We want to design a good input to obtain the desired response.

2) **Simulation**: If we know how a system behaves and we know the command we want to give to it. Then we want to make a **simulation**. I.e. we want to give the command to the system and observe the output.
3) **System Identification**. If we do not know how a system behaves, but we can give it commands and make observations about its response. Then, in this situation we want to perform **system identification**. I.e. we want to develop understanding about the system dynamics by observing how the system responds to different inputs.

In this thesis, we are performing system identification for an unmanned aerial vehicle. To do so, we fly the aircraft and give the aircraft different pilot commands (inputs). Then we observe how the aircraft reacts (output) using the sensors on board the UAS. Based on these commands and observations (inputs and outputs) we try to identify a model describing the UAS dynamics.

There are many ways to perform such a task. References [2], [8]–[11] can be consulted for an overview of these methods. This task can be performed using data in the frequency domain or the time domain. The task can be performed using different mathematical algorithms. Also, there is a wide array of forms in which the aircraft dynamics can be described. In this thesis, we use a time-domain methodology, use an Extended Kalman Filter algorithm, and aim to identify a certain set of stability and control derivatives to describe the UAS dynamics.

1.4 Why use an Extended Kalman filter and a brief introduction to the algorithm

There are many algorithms available for performing system identification. In this thesis, the Extended Kalman Filter (EKF) algorithm is used. The EKF is a modification of the Kalman Filter that can be used for non-linear models. Similar to the Kalman filter, the algorithm is composed of two steps: 1) Prediction, 2) Correction. First, the filter predicts a given value for the

states being estimated. Then, based on the observations/ sensor measurements, the filter corrects the predictions. The filter performs these two steps at each time point. More in-depth discussion of this filter is presented in Chapter 7.

The EKF is a point-by-point algorithm. At every time stamp, the filter processes the new information and outputs a new estimation of the stability and control derivatives. (This method of data processing is referred to as recursive data processing). This makes the filter suitable for online implementation on an aircraft to obtain real-time estimation of stability and control derivatives. This is opposed to other methods that depend on batch processing where the algorithm processes all data points at once. Such algorithms cannot be applied real-time since they require all data to be gathered beforehand.

The possibility of applying the EKF real-time onboard the SkyHunter UAS was one of the main motivations in using the algorithm for this thesis. Other factors that made the EKF appealing were: the ability of the filter to handle noisy data, the ability of the filter to use nonlinear equations, and the simplicity of the algorithm.

There are some disadvantages to using an EKF algorithm, however. Compared to offline batch processing methods, the EKF may yield lower quality estimates. Reference [8], which is the source of the EKF algorithm used in this thesis mentions that: recursive methods for system identification are “approximations of the more elaborative non-recursive methods.” The reference prefers the use of offline batch processing methods unless there is a need for online estimation.

1.5 What is the use of system identification results

It was mentioned earlier that it is important to obtain an understanding of how a certain aircraft fly. This subsection expounds on this idea. Obtaining stability and control derivatives and developing models that describe aircraft motion is needed for many reasons including:

1) **Developing automatic control**. In order to develop an autopilot for an aircraft, some understanding of how the aircraft flies is necessary. Moreover, when the information available regarding the dynamics of an aircraft increases, the ability to develop more complex autopilots increases. Thus, while an autopilot can be designed without stability and control derivatives, the availability of these derivatives allows developing more advanced autopilots.
2) **Developing simulators.** A good understanding of aircraft flight dynamics is needed in order to develop flight simulators that can be used for pilot training. These simulators require a very accurate model of the aircraft. Flight test data can be the only way to obtain the desired models since some flight conditions cannot be understood well through wind tunnel and analytical models [9].
3) **Making improvements to the design of an aircraft.** When the aircraft dynamics are understood, engineers can suggest improvements to the airframe or evaluate whether a modification achieves a desired improvement.
4) **Understanding the handling qualities of the aircraft.** I.e. understanding how easy or difficult it is for a pilot to control the aircraft and how convenient the ride will be for the passengers.
5) **Understanding the capabilities and limitations of an aircraft.**

1.6 Literature review about UAS system Identification

There are many sources in the literature concerned with UAS system identification. Unmanned Aerial Vehicle (UAV) or Unmanned Aerial System (UAS) can be used to talk about such vehicles. Articles address the different platform types such as helicopter, multirotor, fixed-wing, flapping wing and lighter than air vehicles. Reference [14] contain a literature review of UAS system identification and provides brief insights into articles available in the literature. The reference mentions 28 articles on single-rotor UASs, 27 articles on fixed-wing UASs, and 7 articles on other types of UAS. Of the 27 articles on fixed-wing UAS, just three articles used variations of Kalman Filtering: one of these three articles uses an EKF algorithm[15]. Another one uses an Unscented Kalman Filter (UKF) [16]. The last one uses an observer/Kalman filter identification method (OKID) [17].

The reference that uses an EKF algorithm [15] was published in 2007. It focuses on estimating a state space model that relates to aircraft attitude dynamics. Flight data is obtained from an IMU designed and built at the University of New South Wales at the Australian Defence Force Academy. The estimated state space model has the form of Eq 1-1. This thesis identifies a different model. Namely, this thesis is focused on longitudinal translational and rotational motions. The identified terms are the longitudinal non-dimensional stability and control derivatives.

$$\begin{bmatrix}\dot{p}\\ \dot{q}\\ \dot{r}\end{bmatrix}=\begin{bmatrix}A_{1,1} & A_{1,2} & 0 & 0 & 0 & A_{1,6} & 0 & A_{1,8} & 0 & A_{1,10} & A_{1,11} & A_{1,12}\\ 0 & 0 & A_{2,3} & A_{2,4} & A_{2,5} & 0 & A_{2,7} & 0 & A_{2,9} & 0 & 0 & A_{2,12}\\ A_{3,1} & A_{3,2} & 0 & 0 & 0 & A_{3,6} & 0 & A_{3,8} & 0 & A_{3,10} & A_{3,11} & A_{3,12}\end{bmatrix}\begin{bmatrix}pq\\ qr\\ pr\\ p^2\\ r^2\\ p\\ q\\ r\\ \delta_e\\ \delta_r\\ \delta_a\\ \delta_{th}\end{bmatrix} \quad \text{Eq 1-1}$$

The reference that uses an UKF [16] was published in 2002. It presents an architecture for estimation/identification that can be applied to future autonomous vehicles. The architecture would allow online functionalities such as: “robust state estimation”, “damage assessment” and “model identification”. A simulation of a F-15 aircraft is used as the source for flight data. One of the simulated data contains a flight section where the stabilator encounters 50 % failure. The performance of the UKF in capturing the failure is discussed. Thus, the work in the reference can be applied to UASs. However, the reference did not obtain results for a UAS and used simulated data. This thesis obtains results from flight test data of the SkyHunter UAS.

The reference that uses an OKID [17] was published in 1997. It is an interesting reference since system identification for a UAS was performed using a GPS and airspeed and direction sensors. No inertial sensors were used. The Carrier-Phase Differential GPS (CFGPS) provided position, velocity, attitude and attitude rates. The GPS system had low noise. System identification was performed on the Stanford UAV which has a wing span of 12-feet. Two other algorithms are used for system identification in the reference: a Moshe Idan algorithm and a subspace algorithm. Results from the three algorithms are compared to each other.

The identified model in Reference [17] is a decoupled linear state space model. Several flight data sets were used. Some were used for training and some for testing, some for longitudinal motion and some for lateral motion. Results presented in the reference are in the form of two figures showing how the different algorithms predict aircraft states and how the predictions compared to measurements. Percentage error in results are also presented.

This thesis is different from Reference [17] in that the stability and control derivatives of a nonlinear model are being identified in the thesis instead of a linear state space model in the reference. Sensors used in this thesis have high noise instead of low noise in the reference. The

thesis shows the identified derivatives. In the reference, the identified state space model was not presented. Instead the prediction ability of the model was presented in the reference. The thesis also shows results from many flight portions and evaluates the agreement between them.

1.7 Thesis organization

The thesis chapters are organized as follows. In Chapter 2, the aircraft equations of motion used in this thesis are derived. Chapter 3, then presents the geometry and physical characteristics of the SkyHunter. It also presents the sensors and data acquisition systems. Theoretical dynamic models developed for the SkyHunter are presented at the end of the same chapter.

Chapter 4, discusses the procedure for designing flight maneuvers to obtain good data for system identification. Input signals are specified for the SkyHunter.

The extended Kalman filter (EKF) algorithm used for system identification is presented in Chapter 5. The EKF algorithm was coded based on Reference [8]. An example from that reference was recreated to ensure that the EKF works properly. The recreation of the results was excellent with the recreated results being no farther than 5% from the reference.

Initial system identification results obtained from the SkyHunter are shown and discussed in Chapter 6. It was observed that the initial results were unacceptable. The issues with the results are discussed along with a quick summary of steps taken to remedy them. The following three chapters went into more details concerning the issues and their remedy:

a) One of the observed issues was that the SkyHunter data contains high frequency noise. This issue is presented in Chapter 7. Filters were used to remedy this issue. They are presented in the same chapter and their performance is compared.

b) Next, in Chapter 8, attention is given to improving the airflow angle estimation for the SkyHunter.

c) Although system identification maneuvers were deigned in Chapter 4. These maneuvers were not flown due to several circumstances. Thus, a different approach was used to obtain flight data for analysis. This approach is discussed in Chapter 9. The approach depended on choosing flight portions that match certain criteria.

d) In Chapter 10, the EKF measurement noise covariance matrix is adjusted. Results are presented to show how the adjustment of the matrix improved the state propagation in the EKF.

Following the above-mentioned modifications, Chapter 11 presents the improved system identification results. This Chapter shows extensive comparisons of system identification results obtained from different flight portions, using different filters, using different angle of attack estimation as well as other modifications.

It was observed that the system identification results varied depending on the analyzed flight portion. Chapter 12 presents several identified reasons for this inconsistency. Among these reasons is unsteady aerodynamics. This issue is discussed in more detail in Chapter 13.

Chapter 14 shows an experiment in which the horizontal and vertical tail dynamic pressure ratio was measured during flight. Results from this experiment were in agreement with CFD results obtained from another UAS at the University of Kansas [18]. This agreement is presented in Chapter 14. The significance of dynamic pressure ratio on affecting aircraft derivatives is also discussed in the Chapter.

Finally, conclusions and recommendations are presented in the last two chapters. Appendix A provides additional details concerning part of the derivation of the aircraft equations of motion.

2 Derivation of equations of motion

In this chapter, the aircraft equations of motion are derived. The equations are derived in several formats that are useful for this thesis. Derivation of the equations of motions is based on applying the conservation of linear and angular momentum to the aircraft. Derivation of equations of motion is available in standard flight dynamics text books such as [3], [4]. The NASA report [12] was also referenced for the derivation of the equations of motion used in the Extended Kalman Filter (EKF) used for system identification mentioned in Chapter 5.

2.1 Coordinate systems

To begin the discussion on the aircraft equations of motion, it is first necessary to define some coordinate systems. Four coordinate systems are introduced. One of them is an inertial coordinate system while the other three are not. An inertial coordinate system is one that is not accelerating nor rotating [19]. Newton's laws of motion are valid in inertial coordinate systems [3]. The four coordinate systems are:

1) Earth-fixed coordinate system
2) Body-fixed coordinate System
3) Stability coordinate system (based on Roskam's definition [3])
4) Wind coordinate system

The only inertial coordinate system in the previous list is the earth-fixed coordinate system. The rotational motion of the earth is ignored in order to be able to consider the earth-fixed coordinate system as an inertial one. This assumption is acceptable for even supersonic flight, but not for hypersonic flight [3]. The axes of the earth-fixed coordinate system will be donated the letters $X'Y'Z'$ with X' pointing north, Y' pointing East and Z' pointing straight down to complete the right-hand rule.

The body-fixed coordinate system is a coordinate system whose origin is fixed at the aircraft center of mass. Its axes are denoted the letters XYZ. The X axis points straight out of the nose of the aircraft along the aircraft center line. The Y axis is at a right angle to the X axis and points towards the right wing. The Z axis points in the direction that completes the right-hand rule (This would be downwards if the aircraft is in level flight).

The stability coordinate system (according to the definition presented by Roskam [3]) is obtained by rotating the body coordinate system by the trim angle of attack, α_{trim}, about the body Y axis. In order to obtain this coordinate system, a trim condition needs to be defined. Then, the angle of attack required for the aircraft to fly in this trim condition (α_{trim}) is used to define the rotation of the stability coordinate system compared to the body coordinate system. The stability coordinate system is denoted the letters $X_s Y_s Z_s$.

The wind coordinate system can be obtained by first rotating the body coordinate system by the current angle of attack, α, about the body Y axis. (Call this new coordinate system $X_{s'} Y_{s'} Z_{s'}$.) Then, rotate the new coordinate system by the current side slip angle, β, about the $Z_{s'}$ axis. The coordinate system obtained after these two rotations is the wind coordinate system and its axes are $X_w Y_w Z_w$. In the wind coordinate system, X_w always points in the direction of the incoming wind. More discussion on this and a presentation of the rotation matrix between the wind and body coordinate systems is presented in Section 2.4.

2.2 Definition of some variables in the body-fixed coordinate system

Before applying the conservation of momentum equations, it is useful to list the definition of several variables first. These variables are used in the following sections. <u>All the variables defined in this section are in the body-fixed coordinate system.</u>

To start with, an aircraft flying in the air has a velocity relative to the air. This velocity can be decomposed into three components, one component along each of the body coordinate system axes. The component along the body X axis is denoted the letter u, the component along the Y axis is denoted the letter v, The component along the body Z axis is denoted the letter w. Thus, the total aircraft velocity vector, $\vec{V}$, can be written as shown in the following equation. The subscript B indicates that the vector is written in the body coordinate system.

$$\vec{V}_B = \begin{bmatrix} u \\ v \\ w \end{bmatrix} \quad \text{Eq 2-1}$$

Similarly, the aircraft rotational speed can be broken down into three components. The components are denoted the letters P,for rotation about body X axis, Q, for rotation about body Y axis, and R, for rotation about body Z axis. Thus, the total rotation vector, $\vec{\omega}$, can be written as:

$$\vec{\omega}_B = \begin{bmatrix} p \\ q \\ r \end{bmatrix} \quad \text{Eq 2-2}$$

The linear acceleration in the body coordinate system can be written as shown in the following equation.

$$\dot{\vec{V}}_B = \begin{bmatrix} \dot{u} \\ \dot{v} \\ \dot{w} \end{bmatrix} \quad \text{Eq 2-3}$$

The angular acceleration in the body coordinate system can be written as:

$$\dot{\vec{\omega}}_B = \begin{bmatrix} \dot{p} \\ \dot{q} \\ \dot{r} \end{bmatrix} \quad \text{Eq 2-4}$$

The forces acting on the aircraft while in flight can be put into three categories: gravity forces (subscript g), aerodynamic forces (subscript A)and thrust forces (subscript T). These are the common forces that act on an aircraft in usual situations. The force vectors can be written as shown in the following three vectors:

$$\overrightarrow{F_{g_B}} = \begin{bmatrix} F_{g_X} \\ F_{g_Y} \\ F_{g_Z}, \end{bmatrix} \quad \text{Eq 2-5}$$

$$\overrightarrow{F_{A_B}} = \begin{bmatrix} F_{A_X} \\ F_{A_Y} \\ F_{A_Z} \end{bmatrix} \quad \text{Eq 2-6}$$

$$\overrightarrow{F_{T_B}} = \begin{bmatrix} F_{T_X} \\ F_{T_Y} \\ F_{T_Z} \end{bmatrix} \quad \text{Eq 2-7}$$

The force of gravity can be further expanded into:

$$\overrightarrow{F_{g_B}} = m \begin{bmatrix} g_x \\ g_y \\ g_z \end{bmatrix} \quad \text{Eq 2-8}$$

Where m is the mass of the aircraft. g_x, g_y, and g_z are the components of the acceleration due to gravity that act along the body X, Y, and Z axes. These components are further identified in Section 2.5.

The moments acting on the aircraft during flight can be broken down into two categories: Aerodynamic moments and thrust moments. Moment components around the X axis are denoted the letter L. Moment components around the Y axis are denoted the letter M. Moment components around the Z axis are denoted the letter N. Thus, the moment vectors are:

$$\overrightarrow{M_{A_B}} = \begin{bmatrix} L_A \\ M_A \\ N_A \end{bmatrix} \quad \text{Eq 2-9}$$

$$\overrightarrow{M_{T_B}} = \begin{bmatrix} L_T \\ M_T \\ N_T \end{bmatrix} \quad \text{Eq 2-10}$$

A three-dimensional body, like an aircraft, has a certain distribution of mass. This mass distribution will cause the aircraft to have a certain resistance to rotation in different directions. The moment of inertia matrix quantifies this mass distribution. The moment of inertia matrix in the body coordinate system has the following form:

$$I_B = \begin{bmatrix} I_{xx} & -I_{xy} & -I_{xz} \\ -I_{yx} & I_{yy} & -I_{yz} \\ -I_{zx} & -I_{zy} & I_{zz} \end{bmatrix} \quad \text{Eq 2-11}$$

The terms on the diagonal are known as the moment of inertia while the terms off the diagonal are known as the product of inertia. These values are defined mathematically using the integrals shown in the following set of equations. The integrals are calculated by assuming that the entire aircraft is broken down into small mass particles whose x, y, z coordinates are known

$$\begin{array}{ccc} I_{xx} = \int (y^2 + z^2)\, dm & I_{xy} = \int xy\, dm & I_{xz} = \int xz\, dm \\ I_{yx} = \int yx\, dm & I_{yy} = \int (x^2 + z^2)\, dm & I_{yz} = \int yz\, dm \\ I_{zx} = \int zx\, dm & I_{zy} = \int zy\, dm & I_{zz} = \int (x^2 + y^2)\, dm \end{array} \quad \text{Eq 2-12}$$

Looking at the above integrals, it is clear that the products of inertia have the following relations: $I_{xy} = I_{yx}$, $I_{xz} = I_{zx}$ and $I_{yz} = I_{zy}$. Also, most fixed-wing aircraft are symmetric about the XZ plane. Thus, for most aircraft $I_{xy} = I_{yz} = I_{yz} = I_{zy} = 0$ and the moment of inertia matrix simplifies to:

$$I_B = \begin{bmatrix} I_{xx} & 0 & -I_{xz} \\ 0 & I_{yy} & 0 \\ -I_{xz} & 0 & I_{zz} \end{bmatrix} \quad \text{Eq 2-13}$$

Again, all quantities defined in this subsection are in the body coordinate system.

2.3 Transformation from earth-fixed to body-fixed reference frame

It is necessary to be able to transform a vector from the earth-fixed reference frame to the body-fixed reference frame or the opposite. In this section, the transformation between the two systems is described. In addition, the Euler angles that describe an aircraft attitude are defined.

In order to go from the earth-fixed coordinate system to the body-fixed coordinate system the following steps are performed. References [3], [4] can be consulted for a visual description of the below mentioned transformations.

1) Start from the earth-fixed coordinate system. The coordinate system has the X' axis pointing north, the Y' axis pointing east and the Z' axis is obtained using the right-hand rule (it points straight down.)
2) Translate the origin of the coordinate system to the center of gravity of the aircraft. Name this new coordinate system $X_1Y_1Z_1$.

$$\begin{bmatrix} x_1 \\ y_1 \\ z_1 \end{bmatrix} = \overbrace{\begin{bmatrix} 1 & 0 & 0 \\ 0 & 1 & 0 \\ 0 & 0 & 1 \end{bmatrix}}^{R_E^1} \begin{bmatrix} x \\ y \\ z \end{bmatrix}_E \quad \text{Eq 2-14}$$

3) Rotate the coordinate system about $Z_1$by an angle Ψ such that the new X-axis points out of the nose (when looking from above the aircraft). Name the new coordinate system $X_2Y_2Z_2$. The rotation matrix that corresponds to this step is presented below:

$$\begin{bmatrix} x_2 \\ y_2 \\ z_2 \end{bmatrix} = \overbrace{\begin{bmatrix} cos\Psi & sin\Psi & 0 \\ -sin\Psi & cos\Psi & 0 \\ 0 & 0 & 1 \end{bmatrix}}^{R_1^2} \begin{bmatrix} x_1 \\ y_1 \\ z_1 \end{bmatrix} \quad \text{Eq 2-15}$$

4) Rotate the coordinate system about Y_2 by an angle Θ such that the new X-axis points out of the nose (when looking from the side of the aircraft). Name the new coordinate system $X_3Y_3Z_3$. The corresponding rotation matrix is:

$$\begin{bmatrix} x_3 \\ y_3 \\ z_3 \end{bmatrix} = \overbrace{\begin{bmatrix} cos\Theta & 0 & -sin\Theta \\ 0 & 1 & 0 \\ sin\Theta & 0 & cos\Theta \end{bmatrix}}^{R_2^3} \begin{bmatrix} x_2 \\ y_2 \\ z_2 \end{bmatrix} \quad \text{Eq 2-16}$$

5) Rotate the coordinate system about $X_3$by an angle Φ such that the new Y-axis points out of the right wing (when looking straight at the front of the aircraft). The new coordinate system is the body coordinate system(XYZ). The corresponding rotation matrix is:

$$\begin{bmatrix} x \\ y \\ z \end{bmatrix}_B = \overbrace{\begin{bmatrix} 1 & 0 & 0 \\ 0 & cos\Phi & sin\Phi \\ 0 & -sin\Phi & cos\Phi \end{bmatrix}}^{R_3^B} \begin{bmatrix} x_3 \\ y_3 \\ z_3 \end{bmatrix} \quad \text{Eq 2-17}$$

The angles Φ,Θ, Ψ are known as the roll, pitch and yaw angles respectively. All three angles are known as the Euler angles. They describe the attitude (i.e. the orientation) of the aircraft in the air. The notation used for the rotation matrices can be read as follows: R_3^B means the rotation matrix from coordinate system 3 to the body coordinate system. It is possible combine the previous rotations and arrive at a single rotation matrix from the body coordinate frame to the earth-fixed coordinate frame, R_E^B:

$$\begin{bmatrix} x \\ y \\ z \end{bmatrix}_B = R_3^B R_2^3 R_1^2 R_E^1 \begin{bmatrix} x \\ y \\ z \end{bmatrix}_E \quad \text{Eq 2-18}$$

$$\begin{bmatrix} x \\ y \\ z \end{bmatrix}_B = \begin{bmatrix} 1 & 0 & 0 \\ 0 & cos\Phi & sin\Phi \\ 0 & -sin\Phi & cos\Phi \end{bmatrix} \begin{bmatrix} cos\Theta & 0 & -sin\Theta \\ 0 & 1 & 0 \\ sin\Theta & 0 & cos\Theta \end{bmatrix} \begin{bmatrix} cos\Psi & sin\Psi & 0 \\ -sin\Psi & cos\Psi & 0 \\ 0 & 0 & 1 \end{bmatrix} \begin{bmatrix} x \\ y \\ z \end{bmatrix}_E \quad \text{Eq 2-19}$$

$$\begin{bmatrix} x \\ y \\ z \end{bmatrix}_B = \begin{bmatrix} cos\Psi cos\Theta & sin\Psi cos\Theta & -sin\Theta \\ cos\Psi sin\Phi sin\Theta - cos\Phi sin\Psi & cos\Psi cos\Phi + sin\Phi sin\Psi sin\Theta & cos\Theta sin\Phi \\ sin\Phi sin\Psi + cos\Phi cos\Psi sin\Theta & cos\Phi sin\Psi sin\Theta - cos\Psi sin\Phi & cos\Phi cos\Theta \end{bmatrix} \begin{bmatrix} x \\ y \\ z \end{bmatrix}_E \quad \text{Eq 2-20}$$

$$R_E^B = \begin{bmatrix} cos\Psi cos\Theta & sin\Psi cos\Theta & -sin\Theta \\ cos\Psi sin\Phi sin\Theta - cos\Phi sin\Psi & cos\Psi cos\Phi + sin\Phi sin\Psi sin\Theta & cos\Theta sin\Phi \\ sin\Phi sin\Psi + cos\Phi cos\Psi sin\Theta & cos\Phi sin\Psi sin\Theta - cos\Psi sin\Phi & cos\Phi cos\Theta \end{bmatrix} \quad \text{Eq 2-21}$$

Since we have orthonormal matrices (and a product of orthonormal matrices), it is possible to obtain the inverse rotation by simply transforming the matrix. Thus:

$$R_B^E = (R_E^B)^{-1} = (R_E^B)^T \quad \text{Eq 2-22}$$

$$R_B^E = \begin{bmatrix} cos\Psi cos\Theta & cos\Psi sin\Phi sin\Theta - cos\Phi sin\Psi & sin\Phi sin\Psi + cos\Phi cos\Psi sin\Theta \\ sin\Psi cos\Theta & cos\Psi cos\Phi + sin\Phi sin\Psi sin\Theta & cos\Phi sin\Psi sin\Theta - cos\Psi sin\Phi \\ -sin\Theta & cos\Theta sin\Phi & cos\Phi cos\Theta \end{bmatrix} \quad \text{Eq 2-23}$$

2.4 Transformation from body-fixed coordinate system to wind coordinate system

Transformation from the body reference frame to the wind reference frame is done using two simple angular rotations:

1) Rotating the body coordinate system by the current angle of attack, α, about the body Y axis. (Call this new coordinate system $X_{s'}Y_{s'}Z_{s'}$.) The rotation matrix corresponding to this transformation is presented below:

$$\begin{bmatrix} x \\ y \\ z \end{bmatrix}_{S'} = \overbrace{\begin{bmatrix} cos\alpha & 0 & sin\alpha \\ 0 & 1 & 0 \\ -sin\alpha & 0 & cos\alpha \end{bmatrix}}^{R_B^{S'}} \begin{bmatrix} x \\ y \\ z \end{bmatrix}_B \quad \text{Eq 2-24}$$

2) Rotate the new coordinate system by the current side slip angle, β, about the $Z_{s'}$ axis. The coordinate system obtained after these two rotations is the wind coordinate system. The rotation matrix corresponding to this transformation is presented below:

$$\begin{bmatrix} x \\ y \\ z \end{bmatrix}_{w} = \overbrace{\begin{bmatrix} cos\beta & sin\beta & 0 \\ -sin\beta & cos\beta & 0 \\ 0 & 0 & 1 \end{bmatrix}}^{R_{S'}^{w}} \begin{bmatrix} x \\ y \\ z \end{bmatrix}_{S'} \quad \text{Eq 2-25}$$

Thus, to go from body to wind coordinate system the following equation is used:

$$\begin{bmatrix} x \\ y \\ z \end{bmatrix}_{w} = \overbrace{\begin{bmatrix} cos\beta & sin\beta & 0 \\ -sin\beta & cos\beta & 0 \\ 0 & 0 & 1 \end{bmatrix}}^{R_{S'}^{w}} \overbrace{\begin{bmatrix} cos\alpha & 0 & sin\alpha \\ 0 & 1 & 0 \\ -sin\alpha & 0 & cos\alpha \end{bmatrix}}^{R_B^{S'}} \begin{bmatrix} x \\ y \\ z \end{bmatrix}_B \quad \text{Eq 2-26}$$

Again, in the wind coordinate system, the X_w axis always points in the direction of the incoming wind. Thus, in the wind coordinate system, the velocity vector only has an X_w component:

$$\vec{V}_w = \begin{bmatrix} V \\ 0 \\ 0 \end{bmatrix} \quad \text{Eq 2-27}$$

Also, since we are using orthogonal matrices, the inverse of the above rotations is just equal to the transform of the rotation matrices. Thus, the velocity vector can be transformed from the wind frame to the body frame using the following rotations.

$$\begin{bmatrix} u \\ v \\ w \end{bmatrix} = \overbrace{\begin{bmatrix} cos\alpha & 0 & -sin\alpha \\ 0 & 1 & 0 \\ sin\alpha & 0 & cos\alpha \end{bmatrix}}^{R_{S'}^{B}=\left(R_{B}^{S'}\right)^{T}} \overbrace{\begin{bmatrix} cos\beta & sin\beta & 0 \\ -sin\beta & cos\beta & 0 \\ 0 & 0 & 1 \end{bmatrix}}^{R_{w}^{S'}=\left(R_{S'}^{w}\right)^{T}} \begin{bmatrix} V \\ 0 \\ 0 \end{bmatrix} \quad \text{Eq 2-28}$$

2.5 Obtaining the force of gravity in the body coordinate system

One last step before deriving the equations of motion of the aircraft is to derive the force of gravity acting on the aircraft as sensed in the body coordinate system. It is clear that the force of gravity acting on an aircraft always points straight down towards the earth. It is also known that the force of gravity acting on the aircraft is equal to the product of the aircraft mass times the acceleration due to gravity, g. Thus, the force of gravity in the inertial (or earth-fixed) coordinate system is:

$$\overrightarrow{F_{g}}_{E} = m \begin{bmatrix} 0 \\ 0 \\ g \end{bmatrix} \quad \text{Eq 2-29}$$

Since the aircraft rotates in all directions during flight, the force of gravity vector in the body coordinate frame is not constant. Instead, it changes with the Euler angles. An expression for the force of gravity in the body coordinate frame can be obtained using rotation R_E^B presented earlier:

$$\overrightarrow{F_{g}}_{B} = R_E^B \overrightarrow{F_{g}}_{E} \quad \text{Eq 2-30}$$

$$\overrightarrow{F_{g}}_{B} = m \begin{bmatrix} cos\Psi cos\Theta & sin\Psi cos\Theta & -sin\Theta \\ cos\Psi sin\Phi sin\Theta - cos\Phi sin\Psi & cos\Psi cos\Phi + sin\Phi sin\Psi sin\Theta & cos\Theta sin\Phi \\ sin\Phi sin\Psi + cos\Phi cos\Psi sin\Theta & cos\Phi sin\Psi sin\Theta - cos\Psi sin\Phi & cos\Phi cos\Theta \end{bmatrix} \begin{bmatrix} 0 \\ 0 \\ g \end{bmatrix} \quad \text{Eq 2-31}$$

$$\overrightarrow{F_{g}}_{B} = m \begin{bmatrix} -gsin\Theta \\ gsin\Phi cos\Theta \\ gcos\Phi cos\Theta \end{bmatrix} \quad \text{Eq 2-32}$$

2.6 Conservation of Linear and Angular momentum

In Section 2.1 several coordinate systems were defined. In Section 2.2, several quantities describing the aircraft and its motion were defined in the body coordinate system. Rotation matrices between different coordinate systems was defined in Sections 2.3 and 2.4. Then, the

force of gravity acting on an aircraft was obtained in the body coordinate system in Section 2.5. Now, in this section the conservation of linear and angular momentum equations are used.

The conservation of linear and angular momentum must be applied in an inertial coordinate system. Thus, they must be applied in the earth-fixed coordinate system. However, many of the aircraft measurements and aircraft data are easier to measure and identify in the body coordinate system. Therefore, after applying the conservation equations in the earth-fixed coordinate system, the equations will be transformed to the body coordinate system and the wind coordinate system.

2.6.1 Conservation of Linear momentum

The conservation of linear momentum is simply Newton's second law. The equation is written below. In the equation, $\vec{F}$ are the externally applied force vectors, $\vec{p}$ is the linear momentum vector, m is the aircraft mass, and $\vec{V}$ is the aircraft velocity vector. All the quantities are in the earth-fixed inertial frame.

$$\left[\sum \vec{F}\right]_E = \left[\frac{d\vec{p}}{dt}\right]_E \quad \text{Eq 2-33}$$

$$\left[\sum \vec{F}\right]_E = \left[\frac{d(m\vec{V})}{dt}\right]_E = \frac{dm}{dt}\vec{V}_E + m\left[\frac{d\vec{V}}{dt}\right]_E \quad \text{Eq 2-34}$$

If the aircraft loses less than 5% of its mass per minute, it is suitable to assume the aircraft mass is constant as mentioned in Chapter 1 of Reference [3]. This is usually the case for aircraft. Therefore $\frac{dm}{dt}$ will be set to zero obtaining:

$$\left[\sum \vec{F}\right]_E = m\left[\frac{d\vec{V}}{dt}\right]_E \quad \text{Eq 2-35}$$

Now we need to transform the quantities to the body coordinate system. This can be done as in two steps. **First, transform the forces**. This is done by simple matrix multiplication as shown below.

$$[\sum F]_B = R_E^B[\sum F]_E = \overrightarrow{F_{g_B}} + \overrightarrow{F_{A_B}} + \overrightarrow{F_{T_B}} \quad \text{Eq 2-36}$$

The gravity force $\overrightarrow{F_{g_B}}$ was calculated in Section 2.5. For the aerodynamic force and thrust forces, usually they are already represented in the body frame or the wind frame. Therefore, there is no need to figure out a transformation from inertial frame.

Next, transform the derivative of the velocity vector. When transforming a derivative of a vector between frames, attention needs to be given to the rotation of the coordinate frame with time as well as change in the vector itself with time. Both these components contribute to the derivative of the vector in the inertial frame as shown in the following equation.

$$\left[\frac{d\vec{V}}{dt}\right]_E = \overbrace{\left[\frac{d\vec{V}}{dt}\right]_B}^{\substack{Contribution\ from \\ Vector\ change\ with\ time}} + \overbrace{\omega_B \times \vec{V}_B}^{\substack{Contribution\ from \\ coordinate\ system\ rotation\ with\ time}} \quad \text{Eq 2-37}$$

In order to avoid calculating the cross derivative in the previous equation, the cross derivative equivalent matrix is used. The cross derivative equivalent is defined as follows:

$$\omega_B \times \equiv \widetilde{\omega_B} = \begin{bmatrix} 0 & -r & q \\ r & 0 & -p \\ -q & p & 0 \end{bmatrix} \quad \text{Eq 2-38}$$

Thus,

$$\left[\frac{d\vec{V}}{dt}\right]_E = \left[\frac{d\vec{V}}{dt}\right]_B + \widetilde{\omega_B}\vec{V}_B \quad \text{Eq 2-39}$$

The quantities $\left[\frac{d\vec{V}}{dt}\right]_B$, $\vec{V}_B$, ω_B were already defined in Section 2.2. Substituting these definitions in the previous equation yields:

$$\left[\frac{d\vec{V}}{dt}\right]_E = \begin{bmatrix} \dot{u} \\ \dot{v} \\ \dot{w} \end{bmatrix} + \begin{bmatrix} 0 & -r & q \\ r & 0 & -p \\ -q & p & 0 \end{bmatrix} \begin{bmatrix} u \\ v \\ w \end{bmatrix} = \begin{bmatrix} \dot{u} \\ \dot{v} \\ \dot{w} \end{bmatrix} + \begin{bmatrix} qw - rv \\ ur - pw \\ pv - qu \end{bmatrix} \quad \text{Eq 2-40}$$

$$\left[\frac{d\vec{V}}{dt}\right]_I = \begin{bmatrix} \dot{u} + qw - rv \\ \dot{v} + ur - pw \\ \dot{w} + pv - qu \end{bmatrix} \quad \text{Eq 2-41}$$

Mass, m, is a zero-order tensor (i.e. only has magnitude and no direction). Therefore, it remains the same in any coordinate system and does not require transformation. This is why it has no subscript.

Using the previous two steps, the linear momentum equation becomes:

$$\overrightarrow{F_{g_B}} + \overrightarrow{F_{A_B}} + \overrightarrow{F_{T_B}} = m\begin{bmatrix} \dot{u} \\ \dot{v} \\ \dot{w} \end{bmatrix} + m\begin{bmatrix} qw - rv \\ ur - pw \\ pv - qu \end{bmatrix} \quad \text{Eq 2-42}$$

Expanding the force vectors using Eq 2-6, Eq 2-7 and Eq 2-32 yields:

$$m\begin{bmatrix} -gsin\Theta \\ gsin\Phi cos\Theta \\ gcos\Phi cos\Theta \end{bmatrix} + \begin{bmatrix} F_{A_X} \\ F_{A_Y} \\ F_{A_Z} \end{bmatrix} + \begin{bmatrix} F_{T_X} \\ F_{T_Y} \\ F_{T_Z} \end{bmatrix} = m\begin{bmatrix} \dot{u} \\ \dot{v} \\ \dot{w} \end{bmatrix} + m\begin{bmatrix} qw - rv \\ ur - pw \\ pv - qu \end{bmatrix} \quad \text{Eq 2-43}$$

Rearranging the equation yields the standard translational aircraft equations of aircraft motion.

$$m\begin{bmatrix} \dot{u} + qw - rv \\ \dot{v} + ur - pw \\ \dot{w} + pv - qu \end{bmatrix} = m\begin{bmatrix} -gsin\Theta \\ gsin\Phi cos\Theta \\ gcos\Phi cos\Theta \end{bmatrix} + \begin{bmatrix} F_{A_X} \\ F_{A_Y} \\ F_{A_Z} \end{bmatrix} + \begin{bmatrix} F_{T_X} \\ F_{T_Y} \\ F_{T_Z} \end{bmatrix} \quad \text{Eq 2-44}$$

Writing the above matrix equation in algebraic form and solving them for $\dot{u}, \dot{v}$ and $\dot{w}$ yields:

$$\dot{u} = -qw + rv - gsin\Theta + \frac{F_{A_X} + F_{T_X}}{m} \quad \text{Eq 2-45}$$

$$\dot{v} = -ur + pw + gsin\Phi cos\Theta + \frac{F_{A_Y} + F_{T_Y}}{m} \quad \text{Eq 2-46}$$

$$\dot{w} = -pv + qu + gcos\Phi cos\Theta + \frac{F_{A_Z} + F_{T_Z}}{m} \quad \text{Eq 2-47}$$

The previous equations are the translational equations of aircraft motion in Cartesian coordinate form.

2.6.2 Conservation of angular momentum

The conservation of angular momentum is also known as Euler's law. It is the equivalent of Newton's second law for rotational motion. The equation is written below. In the equation, $\vec{M}$

are the externally applied moment vectors, $\vec{h}$ is the angular momentum vector, I is aircraft moment of inertia matrix, and $\vec{\omega}$ is the aircraft rotational velocity vector. All the quantities are in the earth-fixed inertial frame.

$$\left[\sum \vec{M}\right]_E = \left[\frac{d\vec{h}}{dt}\right]_E \quad \text{Eq 2-48}$$

Now we need to transform the quantities to the body coordinate system. This is done in two steps. **First, transform the moments.** This is done by simple matrix multiplication as shown below.

$$\left[\sum \vec{M}\right]_B = R_E^B \left[\sum \vec{M}\right]_E = \overrightarrow{M_{A_B}} + \overrightarrow{M_{T_B}} \quad \text{Eq 2-49}$$

Next, we transformation the angular momentum vector. This is done similar to the transformation of the linear velocity vector.

$$\left[\frac{d\vec{h}}{dt}\right]_E = \left[\frac{d\vec{h}}{dt}\right]_B + \omega_B \times \vec{h}_B \quad \text{Eq 2-50}$$

$$\left[\frac{d\vec{h}}{dt}\right]_E = \left[\frac{d\vec{h}}{dt}\right]_B + \widetilde{\omega_B}\vec{h}_B \quad \text{Eq 2-51}$$

Thus, the conservation of momentum equation becomes:

$$\left[\sum \vec{M}\right]_B = \left[\frac{d\vec{h}}{dt}\right]_B + \widetilde{\omega_B}\vec{h}_B \quad \text{Eq 2-52}$$

The angular momentum vector is equal to $\vec{h} = I\vec{\omega}$, thus

$$\left[\sum \vec{M}\right]_B = \left[\frac{dI\vec{\omega}}{dt}\right]_B + \widetilde{\omega_B} I_B \overrightarrow{\omega_B} \quad \text{Eq 2-53}$$

By the product rule,

$$\left[\sum \vec{M}\right]_B = \left[\frac{dI_B}{dt}\right]_B \overrightarrow{\omega_B} + I_B \left[\frac{d\overrightarrow{\omega_B}}{dt}\right]_B + \widetilde{\omega_B} I_B \overrightarrow{\omega_B} \quad \text{Eq 2-54}$$

If the aircraft mass distribution changes less than 5% per minute, it is suitable to assume the aircraft moment of inertia matrix is constant. This is mentioned in Chapter 1 of Reference [3]. This is the case for the UAS used in this thesis. Therefore $\frac{dI}{dt}$ will be set to zero yielding:

$$\left[\sum \vec{M}\right]_B = I_B \left[\frac{d\vec{\omega}}{dt}\right]_B + \widetilde{\omega_B} I_B \overrightarrow{\omega_B} \qquad \text{Eq 2-55}$$

I_B, $\left[\frac{d\vec{\omega}}{dt}\right]_B$ and $\overrightarrow{\omega_B}$ were defined in Section 2.2. Using their definitions, the equation becomes:

$$\left[\sum \vec{M}\right]_B = \begin{bmatrix} I_{xx} & 0 & -I_{xz} \\ 0 & I_{yy} & 0 \\ -I_{xz} & 0 & I_{zz} \end{bmatrix} \begin{bmatrix} \dot{p} \\ \dot{q} \\ \dot{r} \end{bmatrix} + \begin{bmatrix} 0 & -r & q \\ r & 0 & -p \\ -q & p & 0 \end{bmatrix} \begin{bmatrix} I_{xx} & 0 & -I_{xz} \\ 0 & I_{yy} & 0 \\ -I_{xz} & 0 & I_{zz} \end{bmatrix} \begin{bmatrix} p \\ q \\ r \end{bmatrix} \qquad \text{Eq 2-56}$$

Using Eq 2-9 and Eq 2-10, we obtain

$$\begin{bmatrix} L_A \\ M_A \\ N_A \end{bmatrix} + \begin{bmatrix} L_T \\ M_T \\ N_T \end{bmatrix} = \begin{bmatrix} I_{xx} & 0 & -I_{xz} \\ 0 & I_{yy} & 0 \\ -I_{xz} & 0 & I_{zz} \end{bmatrix} \begin{bmatrix} \dot{p} \\ \dot{q} \\ \dot{r} \end{bmatrix} + \begin{bmatrix} 0 & -r & q \\ r & 0 & -p \\ -q & p & 0 \end{bmatrix} \begin{bmatrix} I_{xx} & 0 & -I_{xz} \\ 0 & I_{yy} & 0 \\ -I_{xz} & 0 & I_{zz} \end{bmatrix} \begin{bmatrix} p \\ q \\ r \end{bmatrix} \qquad \text{Eq 2-57}$$

Which is equivalent to:

$$\begin{bmatrix} \dot{p}I_{xx} - \dot{r}I_{xz} \\ \dot{q}I_{yy} \\ -\dot{p}I_{zx} + \dot{r}I_{zz} \end{bmatrix} + \begin{bmatrix} -pqI_{xz} + rq(I_{zz} - I_{yy}) \\ pr(I_{xx} - I_{zz}) + (p^2 - r^2)I_{xz} \\ +pq(I_{yy} - I_{xx}) + qrI_{xz} \end{bmatrix} = \begin{bmatrix} L_A + L_T \\ M_A + M_T \\ N_A + N_T \end{bmatrix} \qquad \text{Eq 2-58}$$

These are the standard rotational equations of motion for an aircraft in the body coordinate system. The equations in algebraic form are:

$$\dot{p}I_{xx} - \dot{r}I_{xz} - pqI_{xz} + rq(I_{zz} - I_{yy}) = L_A + L_T \qquad \text{Eq 2-59}$$

$$\dot{q}I_{yy} + pr(I_{xx} - I_{zz}) + (p^2 - r^2)I_{xz} = M_A + M_T \qquad \text{Eq 2-60}$$

$$-\dot{p}I_{zx} + \dot{r}I_{zz} + pq(I_{yy} - I_{xx}) + qrI_{xz} = N_A + N_T \qquad \text{Eq 2-61}$$

2.7 Kinematic Equations

The kinematic equations provide a relationship between Euler angles and body angular rates. They are provided here without derivation. References [3], [4] can be consulted for the derivation.

$$\begin{bmatrix} p \\ q \\ r \end{bmatrix} = \begin{bmatrix} 1 & 0 & -sin\Theta \\ 0 & cos\Phi & cos\Theta sin\Phi \\ 0 & -sin\Phi & cos\Theta cos\Phi \end{bmatrix} \begin{bmatrix} \dot{\Phi} \\ \dot{\Theta} \\ \dot{\Psi} \end{bmatrix} \quad \text{Eq 2-62}$$

The equations can be inverted to obtain:

$$\begin{bmatrix} \dot{\Phi} \\ \dot{\Theta} \\ \dot{\Psi} \end{bmatrix} = \begin{bmatrix} 1 & sin\Phi tan\Theta & cos\Phi tan\Theta \\ 0 & cos\Phi & -sin\Phi \\ 0 & sin\Phi sec\Theta & cos\Phi sec\Theta \end{bmatrix} \begin{bmatrix} p \\ q \\ r \end{bmatrix} \quad \text{Eq 2-63}$$

Note: in the previous inversion, simply transforming the matrix does not work.

Expanding the previous matrix equation into algebraic equations yields:

$$\dot{\Phi} = p + qsin\Phi tan\Theta + rcos\Phi tan\Theta \quad \text{Eq 2-64}$$

$$\dot{\Theta} = q\ cos\Phi - r\ sin\Phi \quad \text{Eq 2-65}$$

$$\dot{\Psi} = qsin\Phi sec\Theta + rcos\Phi sec\Theta \quad \text{Eq 2-66}$$

2.8 Flight path equations

The flight path equations are provided below. They are obtained by rotating the aircraft velocity vector form the body frame to the earth frame using the rotation matrix in equation Eq 2-23. These equations are usually of little importance in system identification. When integrated they allow propagation of aircraft position. Thus, they allow flight path reconstruction. They are more useful for navigational purposes. Note: these equations are only valid when there is no wind. The equations would be modified if wind is present.

$$\begin{bmatrix} \dot{X}' \\ \dot{Y}' \\ \dot{Z}' \end{bmatrix} = \begin{bmatrix} cos\Psi cos\Theta & cos\Psi sin\Phi sin\Theta - cos\Phi sin\Psi & sin\Phi sin\Psi + cos\Phi cos\Psi sin\Theta \\ sin\Psi cos\Theta & cos\Psi cos\Phi + sin\Phi sin\Psi sin\Theta & cos\Phi sin\Psi sin\Theta - cos\Psi sin\Phi \\ -sin\Theta & cos\Theta sin\Phi & cos\Phi cos\Theta \end{bmatrix} \begin{bmatrix} u \\ v \\ w \end{bmatrix} \quad \text{Eq 2-67}$$

2.9 Equations of motion in polar coordinate system

In many cases, it is desirable to use α, β and V in the equations of motion instead of u, v and w (i.e. instead of the body coordinate frame velocity components.) Measurements of α and β are more readily available than measurements of u, v and w. This section presents the derivation of these equations of motion that use α, β and V. The equations are also referred to as

the polar coordinate velocity form of the equations of motion. The derivation is made by the help of Reference [12].

We start by presenting three basic equations that relate α, β and V with u, v and w, wich can be obtained using basic trigonometry.

$$V = \sqrt{u^2 + v^2 + w^2} \quad \text{Eq 2-68}$$

$$\alpha = \tan^{-1}\frac{w}{u} \quad \text{Eq 2-69}$$

$$\beta = \sin^{-1}\frac{v}{V} \quad \text{Eq 2-70}$$

Again, using basic trigonometry, the following three equations can be obtained:

$$u = V\, cos\alpha\, cos\beta \quad \text{Eq 2-71}$$

$$v = V\, sin\beta \quad \text{Eq 2-72}$$

$$w = V\, sin\alpha\, cos\beta \quad \text{Eq 2-73}$$

Now, we take the derivative of Eq 2-68, Eq 2-69 and Eq 2-70.

$$\dot{V} = \frac{1}{V}(u\dot{u} + v\dot{v} + w\dot{w}) \quad \text{Eq 2-74}$$

$$\dot{\alpha} = \frac{u\dot{w} - w\dot{u}}{u^2 + w^2} \quad \text{Eq 2-75}$$

$$\dot{\beta} = \frac{V\dot{v} - v\dot{V}}{V^2\sqrt{1 - \left(\frac{v^2}{V^2}\right)}} = \frac{(u^2 + w^2)\dot{v} - vw\dot{w} - vu\dot{u}}{V^2\sqrt{u^2 + w^2}} \quad \text{Eq 2-76}$$

Next, we return to the Cartesian form of the translational equations of motion of an aircraft (Eq 2-45 to Eq 2-47) and substitute u, v, w with equations Eq 2-71 to Eq 2-73. This yields:

$$\dot{u} = -qV\, sin\alpha\, cos\beta + rV\, sin\beta - gsin\Theta + \frac{F_{A_X} + F_{T_X}}{m} \quad \text{Eq 2-77}$$

$$\dot{v} = -V\, cos\alpha\, cos\beta r + pV\, sin\alpha\, cos\beta + gsin\Phi cos\Theta + \frac{F_{A_Y} + F_{T_Y}}{m} \quad \text{Eq 2-78}$$

$$\dot{w} = -pV\, sin\beta + qV\, cos\alpha\, cos\beta + gcos\Phi cos\Theta + \frac{F_{A_Z} + F_{T_Z}}{m} \quad \text{Eq 2-79}$$

Now, we plug equations for $u, v, w, \dot{u}, \dot{v}$ and $\dot{w}$ into the equations for $\dot{V}, \dot{\alpha}, \dot{\beta}$. I.e we plug Eq 2-71 to Eq 2-73 and Eq 2-77 to Eq 2-79 into Eq 2-74 to Eq 2-76. After algebraic simplifications, we obtain:

$$\dot{V} = \left(\frac{F_{A_X} + F_{T_X}}{m} - gsin\Theta\right) cos\alpha\ cos\beta + \left(\frac{F_{A_Y} + F_{T_Y}}{m} + gsin\Phi cos\Theta\right) sin\beta + \left(\frac{F_{A_Z} + F_{T_Z}}{m} + gcos\Phi cos\Theta\right) sin\alpha\ cos\beta \quad \text{Eq 2-80}$$

$$\dot{\alpha} = \frac{1}{Vcos\beta}\left(\left(\frac{F_{A_Z} + F_{T_Z}}{m} + gcos\Phi cos\Theta\right) cos\alpha - \left(\frac{F_{A_X} + F_{T_X}}{m} - gsin\Theta\right) sin\alpha\right) + q - tan\beta\ (p\ cos\alpha + r\ sin\alpha) \quad \text{Eq 2-81}$$

$$\dot{\beta} = \frac{cos\beta}{V}\left(\frac{F_{A_Y} + F_{T_Y}}{m} + gsin\Phi cos\Theta\right) + psin\alpha - rcos\alpha - \frac{sin\beta}{V}\left(\left(\frac{F_{A_Z} + F_{T_Z}}{m} + gcos\Phi cos\Theta\right) sin\alpha + \left(\frac{F_{A_X} + F_{T_X}}{m} - gsin\Theta\right) cos\alpha\right) \quad \text{Eq 2-82}$$

The previous three equations are the polar form of the translational equations of aircraft motion.

2.10Non-Dimensional force and moment coefficients

It is customary to represents aerodynamic forces and moments using non-dimensional coefficients. These are defined as:

$$F_{A_X} = \bar{q}SC_X \quad \text{Eq 2-83}$$

$$F_{A_Y} = \bar{q}SC_Y \quad \text{Eq 2-84}$$

$$F_{A_Z} = \bar{q}SC_Z \quad \text{Eq 2-85}$$

$$L_A = \bar{q}SbC_l \quad \text{Eq 2-86}$$

$$M_A = \bar{q}S\bar{c}C_m \quad \text{Eq 2-87}$$

$$N_A = \bar{q}SbC_n \quad \text{Eq 2-88}$$

Where $\bar{q} = \frac{1}{2}\rho V^2$,known as the dynamic pressure, $\bar{c}$ is the mean aerodynamic chord of the wing, b is the wing sapn, S is the wing planform area.

Lift and drag act along the $-Z_S$ and $-X_s$ axes that were defined in Section 2.2. Thus, the lift and drag coefficients can be obtained from C_X and C_Z using trigonometry as:

$$C_L = -C_Z cos\alpha + C_X sin\alpha \quad \text{Eq 2-89}$$

$$C_D = -C_X cos\alpha - C_Z sin\alpha \quad \text{Eq 2-90}$$

Another transformation would be useful in simplifying the equations of motion. This transformation obtains the drag and side force coefficients acting along the Wind X_w and Y_w axes:

$$C_{D_{wind}} = C_D cos\beta - C_Y sin\beta \quad \text{Eq 2-91}$$

$$C_{Y_{wind}} = C_Y cos\beta + C_D sin\beta \quad \text{Eq 2-92}$$

2.11 Placing the Non-Dimensional Coefficients in the equations of motion

Having defined the non-dimensional coefficients, we now insert them into the equations of aircraft motion. This is done by plugging Eq 2-83 to Eq 2-89 into the equations of motion as described in the following subsections.

2.11.1 The Cartesian form of the translational equations of motion

Plugging Eq 2-83 to Eq 2-85 into Eq 2-45 to Eq 2-47 yields:

$$\dot{u} = -qw + rv - gsin\Theta + \frac{\bar{q}S}{m}C_X + \frac{F_{T_X}}{m} \quad \text{Eq 2-93}$$

$$\dot{v} = -ur + pw + gsin\Phi cos\Theta + \frac{\bar{q}S}{m}C_Y + \frac{F_{T_Y}}{m} \quad \text{Eq 2-94}$$

$$\dot{w} = -pv + qu + gcos\Phi cos\Theta + \frac{\bar{q}S}{m}C_Z + \frac{F_{T_Z}}{m} \quad \text{Eq 2-95}$$

2.11.2 The rotational equations of motion

Plugging Eq 2-86 to Eq 2-88 into Eq 2-59 to Eq 2-61 yields:

$$\dot{p}I_{xx} - \dot{r}I_{xz} - pqI_{xz} + rq(I_{zz} - I_{yy}) = \bar{q}SbC_l + L_T \quad \text{Eq 2-96}$$

$$\dot{q}I_{yy} + pr(I_{xx} - I_{zz}) + (p^2 - r^2)I_{xz} = \bar{q}S\bar{c}C_m + M_T \quad \text{Eq 2-97}$$

$$-\dot{p}I_{zx} + \dot{r}I_{zz} + pq(I_{yy} - I_{xx}) + qrI_{xz} = \bar{q}SbC_n + N_T \quad \text{Eq 2-98}$$

2.11.3 The kinematic equations

No changes happen to the kinematic equations (Eq 2-64 to Eq 2-66)

$$\dot{\Phi} = p + qsin\Phi tan\Theta + rcos\Phi tan\Theta \quad \text{Eq 2-99}$$

$$\dot{\Theta} = q\ cos\Phi - r\ sin\Phi \quad \text{Eq 2-100}$$

$$\dot{\Psi} = qsin\Phi sec\Theta + rcos\Phi sec\Theta \quad \text{Eq 2-101}$$

2.11.4 Polar form of the translational equations of motion

Plugging Eq 2-83 to Eq 2-85 and Eq 2-89 to Eq 2-92 into Eq 2-80 to Eq 2-82 yields:

$$\dot{V} = -\frac{\bar{q}S}{m}C_{D_{wind}} - gsin\Theta cos\alpha cos\beta + gsin\Phi cos\Theta sin\beta + gcos\Phi cos\Theta sin\alpha\ cos\beta + \frac{F_{T_X}}{m}cos\alpha cos\beta + \frac{F_{T_Y}}{m}sin\beta + \frac{F_{T_Z}}{m}sin\alpha\ cos\beta \quad \text{Eq 2-102}$$

$$\dot{\alpha} = \frac{1}{Vcos\beta}\left(-\frac{\bar{q}S}{m}C_L + gcos\Phi cos\Theta cos\alpha + gsin\Theta sin\alpha + \frac{F_{T_Z}}{m}cos\alpha - \frac{F_{T_X}}{m}sin\alpha\right) + q - tan\beta\ (p\ cos\alpha + r\ sin\alpha) \quad \text{Eq 2-103}$$

$$\dot{\beta} = \frac{1}{V}\left(\frac{\bar{q}S}{m}C_{Y_{wind}} + gsin\Phi cos\Theta cos\beta - gcos\Phi cos\Theta sin\alpha sin\beta + gsin\Theta cos\alpha sin\beta - \frac{F_{T_Z}}{m}sin\alpha sin\beta + \frac{F_{T_Y}}{m}cos\beta - \frac{F_{T_X}}{m}cos\alpha sin\beta\right) + psin\alpha - rcos\alpha \quad \text{Eq 2-104}$$

Chapter 18(Appendix A) provides a step-by-step derivation of the previous three equations.

2.12Adjusting the thrust terms

The thrust force and moment vectors can be written down as follows:

$$\overrightarrow{F_{T_B}} = \begin{bmatrix} F_{T_X} \\ 0 \\ F_{T_Z} \end{bmatrix} = \begin{bmatrix} Tcos(\sigma_T) \\ 0 \\ -Tsin(\sigma_T) \end{bmatrix} \quad \text{Eq 2-105}$$

$$\overrightarrow{M_{T_B}} = \begin{bmatrix} 0 \\ M_T \\ 0 \end{bmatrix} = \begin{bmatrix} 0 \\ T(l_{tx}\sin\sigma_T + l_{tz}\cos\sigma_T) \\ 0 \end{bmatrix} \quad \text{Eq 2-106}$$

This assumes that:

1) The thrust force acts only in the longitudinal plane. I.e. it only has X and Z force components and only has a rotational moment about the Y axis. This is a reasonable assumption for the SkyHunter since it only has one motor providing thrust.
2) There is only one motor on the aircraft. This is true for the SkyHunter
3) We know the total thrust force magnitude, T.
4) The thrust vector is inclined by an angle σ_T above the aircraft body X axis.
5) The location of the motor with respect to the aircraft center of gravity (CG) is known. Positive l_{tx} is the motor location forward of the CG. Positive l_{tz} motor location below the CG. These distances can be measured for a given aircraft.

The following section inserts these modified thrust force and moment vectors into the equations of motion.

2.13Decoupled longitudinal equations of motion

We can simplify the equations of motion by assuming that lateral-directional motion variables do not have a strong effect on longitudinal motion. This is acceptable for some circumstances. The simplification is done by assuming, β, p, r and ϕ are all constant at zero (or small enough to be unimportant) [12]. For this simplification we use the approximation that if angle a is zero (or small enough to be unimportant), then, $\sin(a) \approx 0$ and $\cos(a) \approx 1$.

Under these simplifications, and using the thrust terms from Section 2.12, the longitudinal equations of motion (which are Eq 2-97, Eq 2-100, Eq 2-102 and Eq 2-103), become:

$$\dot{V} = -\frac{\bar{q}S}{m} C_{D_{wind}} - g sin\Theta cos\alpha + g cos\Theta sin\alpha + \frac{T cos(\sigma_T)}{m} cos\alpha + \frac{-T sin(\sigma_T)}{m} sin\alpha \qquad \text{Eq 2-107}$$

$$\dot{\alpha} = \frac{1}{V}\left(-\frac{\bar{q}S}{m}C_L + gcos\Theta cos\alpha + gsin\Theta sin\alpha + \frac{-Tsin(\sigma_T)}{m}cos\alpha - \frac{Tcos(\sigma_T)}{m}sin\alpha\right) + q \quad \text{Eq 2-108}$$

$$\dot{\Theta} = q \quad \text{Eq 2-109}$$

$$\dot{q}I_{yy} = \bar{q}S\bar{c}C_m + T(l_{tx}\sin\sigma_T + l_{tz}\cos\sigma_T) \quad \text{Eq 2-110}$$

Using the trigonometric identities:

$$\sin(\alpha \pm \beta) = \sin(\alpha)\cos(\beta) \pm \cos(\alpha)\sin(\beta) \quad \text{Eq 2-111}$$

$$\cos(\alpha \pm \beta) = \cos(\alpha)\cos(\beta) \mp \sin(\alpha)\sin(\beta) \quad \text{Eq 2-112}$$

The longitudinal equations of motion further simplify to:

$$\dot{V} = -\frac{\bar{q}S}{m}C_{D_{wind}} - gsin(\theta - \alpha) + \frac{T}{m}\cos(\sigma_T + \alpha) \quad \text{Eq 2-113}$$

$$\dot{\alpha} = \frac{1}{V}\left(-\frac{\bar{q}S}{m}C_L + gcos(\theta - \alpha) - \frac{T}{m}\sin(\sigma_T + \alpha)\right) + q \quad \text{Eq 2-114}$$

$$\dot{\Theta} = q \quad \text{Eq 2-115}$$

$$\dot{q}I_{yy} = \bar{q}S\bar{c}C_m + T(l_{tx}\sin\sigma_T + l_{tz}\cos\sigma_T) \quad \text{Eq 2-116}$$

For negligible β, $C_{D_{wind}} = C_D$ as can be seen in Eq 2-91. Using this relation and rearranging the longitudinal equations of motion we obtain:

$$\dot{V} = -\frac{\bar{q}S}{m}C_D + gsin(\alpha - \theta) + \frac{T}{m}\cos(\alpha + \sigma_T) \quad \text{Eq 2-117}$$

$$\dot{\alpha} = -\frac{\bar{q}S}{mV}C_L + q + \frac{g}{V}cos(\alpha - \theta) - \frac{T}{mV}\sin(\alpha + \sigma_T) \quad \text{Eq 2-118}$$

$$\dot{\Theta} = q \quad \text{Eq 2-119}$$

$$\dot{q} = \frac{\bar{q}S\bar{c}}{I_{yy}}C_m + \frac{T}{I_{yy}}(l_{tx}\sin\sigma_T + l_{tz}\cos\sigma_T) \quad \text{Eq 2-120}$$

These are the equations of motion used for system identification in this thesis.

2.14Non-dimensional stability and control derivatives

Now, the next step will be to break down each of the aerodynamic derivatives into a sum of linear terms. For simplicity and to follow the equations used for system identification in Reference [8], it will be assumed that drag and lift coefficients,C_D and C_L, are only functions of

velocity and angle of attack. The pitching moment coefficient, C_m, will be assumed to be a function of velocity, angle of attack, pitch rate and elevator deflection. Thus:

$$C_D = C_{L_0} + C_{D_V}\frac{V}{V0} + C_{D_\alpha}\alpha \quad \text{Eq 2-121}$$

$$C_L = C_{L_0} + C_{L_V}\frac{V}{V0} + C_{L_\alpha}\alpha \quad \text{Eq 2-122}$$

$$C_m = C_{m_0} + C_{m_V}\frac{V}{V0} + C_{m_\alpha}\alpha + C_{m_q}\left(\frac{q\bar{c}}{2V0}\right) + C_{m_{de}}de \quad \text{Eq 2-123}$$

The previous three equations include several simplifications:

1) They assume linear relationships.
2) They assume the derivatives depend only on a limited number of longitudinal terms. In reality, the longitudinal coefficients depend on a larger number of parameters. For example, an important derivative that is omitted is $C_{m_{\dot{\alpha}}}$.
3) The equations also assume that the aircraft is symmetric and flying at zero sideslip and that the lateral-directional motions are small enough to have negligible effect on the longitudinal aerodynamics [12].

3 The SkyHunter

The SkyHunter aircraft is a commercially available unmanned aerial system (UAS). It features a twin tail boom design and is designed to have a pusher propulsion configuration. The aircraft is mostly foam built with the fuselage, main wings, horizontal and vertical tails being made out of foam. The two tail booms are composite. The standard aircraft has ailerons and an elevator as control surfaces. However, the aircraft was modified in house at the University of Kansas to include rudders.

A picture of the SkyHunter is presented below. To improve the structural integrity of the aircraft, some modifications were made to the original airframe. Landing gear were added to avoid the risks involved with hand launching and belly landing of the aircraft. Additionally, the belly of the fuselage and some sections on the main wing, the horizontal tail and the vertical tails were reinforced with fiberglass.

Figure 3-1: The SkyHunter

In this chapter, geometric and physical information about the SkyHunter are presented in Section 3.1. A brief presentation of the sensors used on the SkyHunter is in Section 3.2. Section 3.3 presents the theoretical dynamic models developed for the SkyHunter. A decoupled linear

time-invariant (LTI) model for the SkyHunter is presented in Section 3.4. Lastly, the handling qualities are presented in Section 3.5.

3.1 Physical characteristics of the SkyHunter

The University of Kansas owns several SkyHunter aircraft, each aircraft varies from the other to some degree. Additionally, the aircraft were flown in different configurations and using different avionics. Therefore, the physical characteristics changed from flight to flight. Table 3-1, summarizes the physical characteristics of the SkyHunter in its different flight configurations. In this thesis, only SkyHunter 2 was used for system identification. SkyHunter 3 was used while working on the thesis but no results from it are presented. SkyHunter 4 was used for the experimentation in Chapter 14.

As it can be seen in the table headers, the SkyHunter was flown in some cases with winglets and in some cases without winglets. These winglets changed the aerodynamic characteristics of the aircraft along with the physical characteristics. This should be kept in mind when analyzing flights with and without winglets. The system identification results would be expected to be different to some degree due to the presence of winglets.

Table 3-1: Physical Characteristics of several SkyHunter versions

		SkyHunter 2 w/ winglets	**SkyHunter 3 No winglets**	**SkyHunter 4 No winglets**
S	ft^2	4.819	4.44	4.44
$\overline{\boldsymbol{C}}$	ft	0.7313	0.7550	0.7550
b	ft	6.875	5.896	5.896
AR	~	9.808	7.83	7.83
Mass	lbm	9.84	9.88	8
Flight Time	min	~45	~45	~45
Max Motor Power	W	800	668	800
Aircraft AC X location	In	19.45	19.70	19.69
Aircraft CG X location	In	17.32	17.32	18.00
Static Margin	%	24.26	26.27	18.65

SkyHunter 2 and 4 are equipped with a HiMax HC 4220-770 brushless electric motor. Its maximum power was estimated at 800 W. SkyHunter 3 used a Turnigy G46 Brushless Outrunner 670kv motor. Its estimated maximum power is 668 W. The moments and of inertia and the XZ product of inertia for the SkyHunter are presented in the following table. For simplicity, it was assumed that $I_{XZ} = 0$.

Table 3-2: SkyHunter Moments and XZ product of inertia

		SkyHunter w/ winglets	**SkyHunter No winglets**
$\boldsymbol{I_{xx_{Body}}}$	$slug\ ft^2$	0.44	0.32
$\boldsymbol{I_{yy_{Body}}}$	$slug\ ft^2$	0.54	0.54
$\boldsymbol{I_{zz_{Body}}}$	$slug\ ft^2$	0.35	0.23
$\boldsymbol{I_{xz_{Body}}}$	$slug\ ft^2$	0	0

3.2 Avionics and data acquisition system

Flight data is collected from three sources on the SkyHunter: 1) the sensors in the Pixhawk autopilot, 2) A pressure sensor, 3) A GPS device. The Pixhawk is an open source autopilot that can be used for controlling ground vehicles, air vehicles and submersibles [20]. It contains several sensors inside the main unit, which is shown in the following figure. A pressure sensor is connected to the Pixhawk and is used to obtain airspeed measurements. A GPS device is also connected to the Pixhawk.

Figure 3-2: The Pixhawk [20]

The sensors inside the Pixhawk are:

1) ST Micro L3GD20H 16 bit gyroscope

2) ST Micro LSM303D 14 bit accelerometer / magnetometer
3) Invensense MPU 6000 3-axis accelerometer/gyroscope
4) MEAS MS5611 barometer

They are used to obtain aircraft accelerations (a_x, a_y, a_z), rotation rates (p, q, r), Euler angles (ϕ, θ, ψ) and barometer altitude. Using the pressure sensor connected to the Pixhawk and a pitot tube, airspeed (V) is obtained. The pilot commands given to the pixhawk are also recorded in the flight logs. They are the elevator, aileron, rudder and thrust commands ($\delta_e, \delta_a, \delta_r, \delta_T$).

The SkyHunter uses an estimation algorithm to estimate airflow angles, i.e. angle of attack and side slip angle (α, β). This estimation algorithm uses the information from the pixhawk sensors but runs on a separate onboard computer.

All sensors variables are recorded in the flight log at a sampling rate of 20 Hz. The highest frequency of aircraft dynamic modes is usually no more than 5 Hz [21]. Therefore, using a sampling rate of 20 Hz is suitable since it is higher than the Nyquist frequency, ($f_N = 2 \times 5\ Hz = 10\ Hz$).

The following table shows an estimate of the cost of the sensors on board the SkyHunter. The table was assembled based on prices found online. As it can be seen, the total cost of the sensors is about 175 USD. This is clearly much lower than the cost of instrumentation used on manned aircraft. Thus, it would not be strange if the quality of data is lower than that of manned aircraft.

Table 3-3: Estimated Cost of SkyHunter Sensors

Item	**Cost in USD**
Pixhawk + GPS	121
Pressure sensor + Pitot tube	53
Total Cost	174

3.3 Theoretical dynamic model

A theoretical dynamic model for the SkyHunter was developed using Advanced Aircraft Analysis (AAA) software. [6] This model provides a base for evaluating the system identification results presented later in the thesis. AAA uses physics based methods as well as semi-empirical methods in developing the theoretical model of aircraft [22]. In Table 3-4, the stability and control derivatives obtained from the AAA model for the SkyHunter are presented. Several models were developed to reflect the changes between the different configurations of the SkyHunter. The derivatives obtained from these different models are presented in the table. Also, the trim conditions for which these stability and control derivatives are obtained are listed in the table. All models are developed for straight-line wings level flight trim condition. Thus, $\Phi_{trim} = P_{trim} = Q_{trim} = R_{trim} = \beta_{trim} = 0$.

The exact airfoil of the SkyHunter wing was not known. Therefore, it was estimated. Two airfoils were selected as potential candidates: the GEO 438 airfoil and the Clark Y airfoil. Section 3.3.1, discusses how the airfoils were selected.

Stability and control derivatives obtained based on the different airfoils are presented in Table 3-4 for the SkyHunter 2 with winglets. The differences between these two models are more than just the airfoil choice. However, it can be seen that depending on the airfoil choice and depending on the other decisions made in the modeling process, the stability and control derivatives obtained from AAA would vary.

Therefore, when evaluating the system identification results and comparing them to AAA, it should be clear that the AAA values are not the “truth”. They are useful in showing where the expected stability and control derivatives should generally be. However, they are

likely not a true representation of reality. In reality, the derivatives are probably higher or lower to a certain extent.

Table 3-4: Theoretical Estimates for the SkyHunter stability and control derivatives obtained from AAA.

Quantity	**Units**	**SkyHunter 2 w/ winglets**		**SkyHunter 3 No winglets**	**SkyHunter 4 No winglets**
Estimated wing airfoil		**GOE 438**	**Clark Y**	**Clark Y**	**Clark Y**
Trim Velocity, $\boldsymbol{V_{trim}}$	ft/s	50.6	50.6	50.6	50.6
Trim angle of attack, $\boldsymbol{\alpha_{trim}}$	$deg.$	2.73	6.38	7.82	5.09
Trim elevator deflection, $\boldsymbol{de_{trim}}$	$deg.$	1.5	-0.79	-1.58	2.8
Trim aileron deflection, $\boldsymbol{da_{trim}}$	$deg.$	0	0	0	0
Trim rudder deflection, $\boldsymbol{dr_{trim}}$	$deg.$	0	0	0	0
Trim throttle, $\boldsymbol{dT_{trim}}$	%	0.632	0.688	0.706	0.624
$\boldsymbol{C_{D_0}}$	~	0.0265	0.0246	0.0261	0.0260
$\boldsymbol{C_{D_u}}$	~	0	0	0	0
$\boldsymbol{C_{D_\alpha}}$	rad^{-1}	0.2402	0.2301	0.2526	0.1886
$\boldsymbol{C_{L_0}}$	~	0.5046	0.4231	0.4065	0.4065
$\boldsymbol{C_{L_u}}$	~	0.0012	0.0015	0.0016	0.0013
$\boldsymbol{C_{L_\alpha}}$	rad^{-1}	5.7774	3.7005	3.6332	3.6277
$\boldsymbol{C_{L_q}}$	rad^{-1}	6.3370	5.0577	5.3183	4.6251
$\boldsymbol{C_{L_{de}}}$	rad^{-1}	0.2931	0.3060	0.3405	0.3376
$\boldsymbol{C_{m_0}}$	~	0.0442	0.0574	0.0688	0.0985
$\boldsymbol{C_{m_u}}$	~	0.000189	0.000355	0.000397	0.000319
$\boldsymbol{C_{m_\alpha}}$	rad^{-1}	-0.8888	-0.8978	-0.9559	-0.6768
$\boldsymbol{C_{m_q}}$	rad^{-1}	-15.233	-14.5737	-15.1839	-14.2746
$\boldsymbol{C_{m_{de}}}$	rad^{-1}	-1.0266	-1.1318	-1.2194	-1.1839

3.3.1 Estimating the wing airfoil

Two processes were used to estimate the SkyHunter airfoil. The first process resulted in choosing the GEO 438 airfoil. However, the lift aircraft lift coefficient obtained based on this airfoil seemed high. So, the selection of airfoil was revisited and the second process arrived at the Clark Y airfoil. Both processes are presented below. Again, the airfoil was estimated since the actual airfoil was unknown.

3.3.1.1 The first process

The first process depended mostly on visually matching the SkyHunter wing tip shape with a known airfoil. To do so, the wing tip of the SkyHunter was traced on a piece of paper and a picture of that trace was then taken (see following figure.)

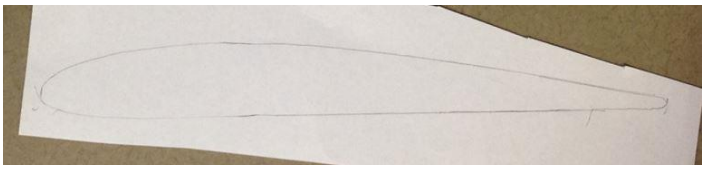

Figure 3-3: Trace of SkyHunter wingtip

Then, the airfoil database in AAA was consulted. AAA allows users to scroll through visuals of many airfoils. While scrolling through these pictures, airfoils that seemed similar to the SkyHunter were identified. After sifting through the different airfoils, eight airfoils were selected for final comparison. Table 3-5, shows how these airfoils compared to the SkyHunter wing tip.

From these eight airfoils, three airfoils were selected for closer comparison. The GOE 438. Waspsm and NACA M5 airfoils. Some airfoil characteristics were compared to arrive at the final airfoil selection. These characteristics are airfoil maximum thickness, maximum camber and the location of these two quantities along the chord of the airfoil. All quantities were obtained as percentage chord. Table 3-6, presents these values for the SkyHunter wing tip and the different airfoils.

Table 3-5: Potential airfoil matches, compared to the SkyHunter wingtip

Airfoil	Shape	SkyHunter Wingtip
Goe 438	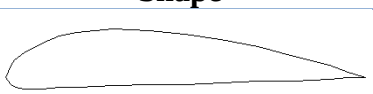	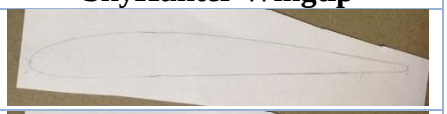
Goe 55		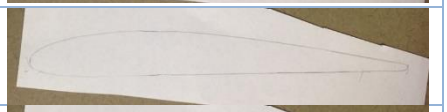
S4110		
USA-35B	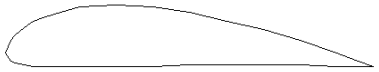	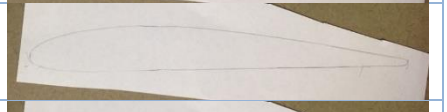
USA49		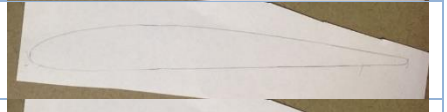
Wasp smoothed	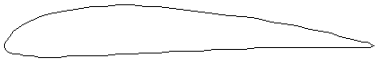	
M4		
M5		

Table 3-6: Geometric characteristics of considered airfoils and of SkyHunter wingtip. All values are as % of chord.

	SkyHunter Wingtip	**GOE 438**	**Wasp smoothed**	**NACA M5**
Maximum thickness, t_{max}	11.9-12.2%	11 %	9.4%	8.2%
t_{max} ***location along airfoil chord***	26.5%	29.8%	27.1%	30.1%
Maximum camber, c_{max}	3.4%	3.7%	3%	2.1%
c_{max} ***location along airfoil chord***	38.8%	39.8%	37.9%	30.1%
Reference	Measured	[23]	[24]	[25]

Comparing the values in the table, the GOE 438 was seen as the closest match to the SkyHunter wing tip airfoil.

3.3.1.2 The second process

It was observed that the lift coefficient for the SkyHunter was too high in the model using the GOE 438 airfoil. Therefore, the airfoil choice was revisited. The maximum thickness and camber of the SkyHunter were measured again along with their location. Then the airfoil tools website [26] was used to search for an airfoil with similar characteristics. Two airfoils seemed

appealing, the Clark YH and the Clark Y. The Clark Y airfoil was chosen for a reason related to reducing modeling error as described in the following paragraph. It was printed on paper and was seen to match the actual wing airfoil to an acceptable degree. Table 3-7 presents the re-measured SkyHunter airfoil characteristics and the Clark Y characteristics.

Table 3-7: Geometric characteristics of SkyHunter wingtip airfoil and ClarkY airfoil. All values are as % of chord.

	SkyHunter Wingtip Re-measured	**Clark Y**
Maximum thickness, t_{max}	11.8%	11.7%
t_{max} location along airfoil chord	29%	28%
Maximum camber, c_{max}	3.4%	3.4%
c_{max} location along airfoil chord	31.5%	42%
Reference	Measured	[27]

The reason behind choosing the Clark Y airfoil was that aerodynamic characteristics for that airfoil are already available in AAA. (Characteristics like airfoil lift curve slope, c_{l_α}, and zero lift angle of attack, c_{l_0}). This meant that there would be no need to obtain airfoil characteristics by hand from airfoil graphs. Instead, AAA would provide these values. This seemed simpler and that it may yield more reliable modeling.

3.4 Decoupled LTI model for the SkyHunter

Based on the AAA model, a set of two decoupled state-space models were developed to describe the SkyHunter motion. The first state-space model is concerned with the longitudinal motion of the SkyHunter. The second state space model is concerned with the lateral-directional motion of the aircraft. Both state space models are linear time invariant (LTI). In this thesis, only the longitudinal model is used. It is used in Chapter 4 to design special maneuvers for system identification.

The LTI models are based on small perturbation theory and they contain several simplifying assumptions. They are developed in the stability coordinate system mentioned in Section 2.1. Reference [3], especially Chapter 5 in it, can be consulted for the methodology of

obtaining the state space models. For the longitudinal model, one addition was made to the methodology presented in the reference. It was the addition of thrust control in the model instead of only having elevator control.

When using the state space models, the variables appearing in the model are the perturbed values. Thus, if the total angle of attack is 5 degrees and the trim angle of attack is 3 degrees, then the value used in the state space model is the perturbation ($5 - 3 \ = 2$ °). This same discussion applies to the other variables in the model. The trim values for the model are presented in Table 3-4: Theoretical Estimates for the SkyHunter stability and control derivatives obtained from AAA.

For longitudinal motion, the state space model has the format:

$$\dot{x_{Long}} = A_{Long}\, x_{Long} + B_{Long}\, u_{Long} \qquad \text{Eq 3-1}$$

where, x_{Long} is the 4x1 state vector and u_{Long} is the 2x1 control vector. A_{Long} is a 4x4 matrix and B_{Long} is a 4x2 matrix. The dot notation means the time derivative. The state and control vectors are as defined below:

$$x_{Long} = \begin{bmatrix} \Delta u \\ \Delta \alpha \\ \Delta \theta \\ \Delta q \end{bmatrix} \qquad \text{Eq 3-2}$$

$$u_{Long} = \begin{bmatrix} \Delta \delta_T \\ \Delta \delta_e \end{bmatrix} \qquad \text{Eq 3-3}$$

In these vectors, Δu is the forward speed perturbation in ft/s, $\Delta \alpha$ is the angle of attack perturbation in rad , $\Delta \theta$ is the pitch angle perturbation in rad, Δq is the pitch rate perturbation in rad/s, $\Delta \delta_T$ is the thrust perturbation as a fraction of 1, $\Delta \delta_e$ is the elevator perturbation in rad.

For lateral motion, the state space model has the format:

$$\dot{x_{Lat}} = A_{Lat}\, x_{Lat} + B_{Lat}\, u_{Lat} \qquad \text{Eq 3-4}$$

where, x_{Lat} is the 4x1 state vector and u_{Lat} is the 2x1 control vector. A_{Lat} is a 4x4 matrix and B_{Lat} is a 4x2 matrix. The dot notation means the time derivative. The state and control vectors are as defined below:

$$x_{Lat} = \begin{bmatrix} \Delta\beta \\ \Delta\phi \\ \Delta p \\ \Delta r \end{bmatrix} \quad \text{Eq 3-5}$$

$$u_{Lat} = \begin{bmatrix} \Delta\delta_a \\ \Delta\delta_r \end{bmatrix} \quad \text{Eq 3-6}$$

In these vectors, $\Delta\beta$ is the side slip angle perturbation in rad,$\Delta\phi$ is the perturbation in roll angle in rad, Δp is the perturbation in the roll rate in rad/s, Δr is the perturbation in yaw rate in rad/s, $\Delta\delta_a$ is the aileron perturbation in rad, $\Delta\delta_r$ is the rudder perturbation in rad.

The state space model for the SkyHunter 2 with winglets model that uses the GOE 438 airfoil is presented below.

$$\begin{bmatrix} \dot{\Delta u} \\ \dot{\Delta\alpha} \\ \dot{\Delta\theta} \\ \dot{\Delta q} \end{bmatrix} = \begin{bmatrix} -0.1240 & 19.0662 & -32.1974 & 0 \\ -0.0250 & -6.2646 & -0.0080 & 0.9405 \\ 0 & 0 & 0 & 1.0000 \\ 0.0224 & -14.6920 & 0.0051 & -2.7085 \end{bmatrix} \begin{bmatrix} \Delta u \\ \Delta\alpha \\ \Delta\theta \\ \Delta q \end{bmatrix} + \begin{bmatrix} 5.9203 & -0.7755 \\ -0.0544 & -0.3158 \\ 0 & 0 \\ 0.2737 & -19.4782 \end{bmatrix} \begin{bmatrix} \Delta\delta_T \\ \Delta\delta_e \end{bmatrix} \quad \text{Eq 3-7}$$

$$\begin{bmatrix} \dot{\Delta\beta} \\ \dot{\Delta\phi} \\ \dot{\Delta p} \\ \dot{\Delta r} \end{bmatrix} = \begin{bmatrix} -0.6048 & 0.6359 & -0.0153 & -0.9797 \\ 0 & 0 & 1.0000 & 0 \\ -35.6302 & 0 & -8.2173 & 2.4916 \\ 34.3722 & 0 & -1.3352 & -2.1524 \end{bmatrix} \begin{bmatrix} \Delta\beta \\ \Delta\phi \\ \Delta p \\ \Delta r \end{bmatrix} + \begin{bmatrix} 0 & 0.2484 \\ 0 & 0 \\ 74.0768 & 3.8109 \\ 0.2435 & -26.3714 \end{bmatrix} \begin{bmatrix} \Delta\delta_a \\ \Delta\delta_r \end{bmatrix} \quad \text{Eq 3-8}$$

3.5 Dynamic modes and flying qualities of the SkyHunter models

The characteristics of the dynamic modes for the SkyHunter models is presented in the following table. This includes the frequencies, ω and damping ratios, ζ, of the second order modes and the time constants, τ, of the first order modes. Negative time constants or damping ratios mean that the dynamic mode is unstable.

Table 3-8: Characteristics of SkyHunter dynamic modes

Aircraft Model	**Units**	**SkyHunter 2 w/ winglets**		**SkyHunter 3 No winglets**	**SkyHunter 4 No winglets**
Estimated wing airfoil		GOE 438	Clark Y	Clark Y	Clark Y
Longitudinal modes					
ω_{SP}	rad/s Hz	5.627 0.896	5.0013 0.796	4.9643 0.7901	4.5597 0.7257
ζ_{SP}		0.806	0.613	0.592	0.701
$\omega_{Phugoid}$	rad/s Hz	0.7168 0.114	0.7864 0.125	0.7933 0.1263	0.7437 0.1184
$\zeta_{Phugoid}$		0.013	-0.001	-0.003	0.005
Lateral modes					
ω_{DR}	rad/s Hz	6.4085 1.020	6.6511 1.059	8.3009 1.3211	8.019 1.2763
ζ_{DR}		0.174	0.152	0.069	0.085
τ_{Spiral}	S	-63.291	-21.946	4.01	3.428
τ_{Roll}	s	0.114	0.149	0.121	0.127

Looking at the previous table, it can see that the SkyHunter 2 has unstable spiral mode. Depending on the model used for SkyHunter 2, the phugoid mode can also be unstable. It can be seen that the highest dynamic mode frequency for SkyHunter 2 is 1.059 (Dutch roll mode, in model using Clark Y airfoil). Attention will be directed to the dynamic mode frequencies again in Chapter 7, which deals with data filtering.

The following table present the flying qualities for the SkyHunter. These flying qualities were evaluated using the aid of AAA software. It can be seen in the table that SkyHunter 2 has good short period damping. It also has good Dutch roll handling qualities. The spiral mode is either level 1 or level 2 depending on the AAA model. The short period frequency is level 1 or level 2 depending on the AAA model. The phugoid is level 2 or 3, again, depending on the AAA model.

Table 3-9: Handling qualities of the SkyHunter

Aircraft Model	**SkyHunter 2 w/ winglets**		**SkyHunter 3 No winglets**	**SkyHunter 4 No winglets**
Estimated wing airfoil	GOE 438	Clark Y	Clark Y	Clark Y
Longitudinal				
ω_{SP} *Level*	1	2	2	1
ζ_{SP} *Level*	1	1	1	1
Phugoid Level	2	3	3	2
Lateral				
ω_{DR} *Level*	1	1	1	1
ζ_{DR} *Level*	1	1	2	1
$\zeta_{DR_{23}}$ *Level*	Met	Met	Met	Met
$\omega_{DR}\zeta_{DR}$ *Level*	1	1	3	3
Spiral Level	1	2	Stable	Stable

4 Input Design

One of the first steps in the system identification process is to collect good data from the aircraft. During the flight, appropriate input signals need to be applied to cause the aircraft flight modes to be excited. This section discusses the process of designing the appropriate input signals. To design the input signals, a priory knowledge of the aircraft dynamic model is needed. As presented in Chapter 3, an aircraft a priory dynamic models were developed using Advanced Aircraft Analysis software. These models are used for input signal design. Work presented in this input design section is based on Reference [8].

Note: Due to several circumstances, the maneuvers designed in this chapter were not flown. This chapter was kept in the thesis since it can provide useful information on input signal design and since the flight maneuvers designed for the SkyHunter can be flown in the future.

There are two approaches to work on input signal design: 1) Input design based on estimation error analysis. 2) Design of Multistep input signals. In this thesis, focus is only given to the second approach. In the second approach, the input signal consists of multiple step inputs that are joined together to form one multi-step signal. An arbitrary input signal can be designed using this approach.

Different signal designs would excite the aircraft differently. Thus, the designed input signal affects the quality of the collected flight data. The gathered flight data will either be “rich” or “poor” in information content for parameter estimation purposes depending on the applied input signal. Thus, the input signal needs to be designed properly to obtain rich data.

In the multistep input signal design approach, the design process is made to answer the following questions:

1) How long should a certain input step command be applied?

2) In what order should the input step commands be applied?

3) What magnitude should each input step command have?

The first and second questions are answered by analyzing the frequency response of the dynamic model and by looking at energy density plots. The third question was answered through dynamic model simulations.

4.1 Frequency response of dynamic model

The design of an input signal that results in "rich" data content is addressed in two steps. The first step focuses on the dynamics of the aircraft. The second step focuses on the properties of different multistep input signals. In the first step, attention is given to understand the dynamic model through the use of bode diagrams. This understanding is used to decide which frequencies need to be excited in order for each parameter of the dynamic model to be identifiable from the gathered data. In the second step, focus is given to design a multi-step input that excites the frequencies specified in the first step. The following diagram illustrates this two-step procedure.

Step 1: Specify frequencies that excite aircraft apropriately	Step 2: Design an input signal that excites the specified frequencies
•Bode diagrams are used in this step •Each parameter of the dynamic model can be detected only at certain input signal frequency ranges •These ranges are specified	•Spectral density plots are used to identify the frequencies excited by a certain multi-step input signal •An input signal is selected that excites the frequencies specified in Step 1

4.1.1 Step 1: Specify frequencies that excite aircraft appropriately:

As mentioned before in Chapter 3, dynamic models have been developed for the SkyHunter using the Advanced Aircraft Analysis tool. The developed dynamic models were assumed to have the following form for the longitudinal direction in this chapter.

$$\begin{bmatrix}\dot{u}\\ \dot{\alpha}\\ \dot{\theta}\\ \dot{q}\end{bmatrix}=\begin{bmatrix}X_u & X_\alpha & X_\theta & X_q\\ Z_u/U_0 & Z_\alpha/U_0 & Z_\theta & Z_q\\ 0 & 0 & 0 & 1\\ M_u & M_\alpha & M_\theta & M_q\end{bmatrix}\begin{bmatrix}u\\ \alpha\\ \theta\\ q\end{bmatrix}+\begin{bmatrix}X_{\delta T} & X_{\delta e}\\ Z_{\delta T} & Z_{\delta e}\\ 0 & 0\\ M_{\delta T} & M_{\delta e}\end{bmatrix}\begin{bmatrix}\delta_T\\ \delta_e\end{bmatrix} \quad \text{Eq 4-1}$$

In the above matrix, u is the aircraft airspeed in the body X axis, α is the angle of attack, θ is the pitch angle, q is the pitch rate and U_0 is the aircraft trim speed. $X_0, Z_0 \; and \; M_0$ all stand for the dimensional stability and control derivatives in the body X axis, Z axis and about the Y axis (pitching moment) respectively. δ_T and δ_e are the thrust and elevator control inputs respectively. The above state space model is a linear time invariant model: the dimensional derivatives are constant values. Loosely speaking, the goal of the system identification process is to identify each of the dimensional derivatives.

For this chapter, the used SkyHunter LTI model was:

$$\begin{bmatrix}\dot{u}\\ \dot{\alpha}\\ \dot{\theta}\\ \dot{q}\end{bmatrix}=\begin{bmatrix}-0.1629 & 19.0817 & -32.1978 & 0\\ -0.0250 & -6.3325 & -0.0074 & 0.9390\\ 0 & 0 & 0 & 1\\ 0.0250 & -15.6379 & 0.0049 & -2.7904\end{bmatrix}\begin{bmatrix}u\\ \alpha\\ \theta\\ q\end{bmatrix}+\begin{bmatrix}6.7895 & -0.7849\\ -0.0627 & -0.3162\\ 0 & 0\\ 0.2504 & -19.5022\end{bmatrix}\begin{bmatrix}\delta_T\\ \delta_e\end{bmatrix} \quad \text{Eq 4-2}$$

Here, we can use the following analogy to illustrate the process presented in the following paragraphs: When listening to a track of music, the different instruments play different pieces with varying sound volume along the track timeline. If we try to identify all the instruments included in a certain orchestral track, we need to listen to the entire track or more specifically to enough portions of the track such that all instruments play a role in these portions.

Likewise, in the system identification process, we can design the input signal to have varying frequencies. Each input signal frequency causes the aircraft to be excited differently. Thus, the terms of the dynamic model may be more or less identifiable. In fact, we can consider the terms unidentifiable at certain input frequencies. Therefore, it is important to specify a set of frequencies that excite all components of the dynamic model to an identifiable degree. This is the goal of the first step of the input signal design. After that, the second step of the input design

(discussed in the following subsection) focuses on designing an input signal that excites this specified set of frequencies.

To understand the range of frequencies at which each term in the dynamic model is identifiable, we do the following: First, we isolate each term in the dynamic model in a separate state space model. In that state space model, the term we are isolating is the only observation. Then, a bode diagram is constructed for each isolated system. Mathematically, this is done as follows:

Considering the state space model of the following form:

$$\dot{x} = Ax + Bu \qquad \text{Eq 4-3}$$

$$y = Cx + D\,u \qquad \text{Eq 4-4}$$

The first equation encompasses the system dynamics. The second equation encompasses the observation equation. The A and B matrices are as defined in the first 2 paragraphs of this subsection. They will be the same for all the new isolated dynamic models. The C and D matrices will be different for each isolated state space model.

Focusing on the moment equation, we desire to have an isolated system for each term in that last row of the dynamic model.[1] This is done as follows:

1) To isolate $\dot{q}$ we use → $C = [M_u \quad M_\alpha \quad M_\theta \quad M_q]$, $D = [M_{\delta T} \quad M_{\delta e}]$
2) To isolate contribution of M_u on pitching motion we use →$C = [M_u \quad 0 \quad 0 \quad 0]$, $D = [0 \quad 0]$
3) To isolate contribution of M_α on pitching motion we use → $C = [0 \quad M_\alpha \quad 0 \quad 0]$, $D = [0 \quad 0]$

[1] For X and Z forces we would focus on the first and second rows respectively and perform the same process.

4) To isolate contribution of M_θ on pitching motion we use→ $C = [0 \quad 0 \quad M_\theta \quad 0]$, $D = [0 \quad 0]$
5) To isolate contribution of M_q on pitching motion we use→ $C = [0 \quad 0 \quad 0 \quad M_q]$, $D = [0 \quad 0]$
6) To isolate contribution of $M_{\delta T}$ on pitching motion we use→ $C = [0 \quad 0 \quad 0 \quad 0]$, $D = [M_{\delta T} \quad 0]$
7) To isolate contribution of $M_{\delta e}$ on pitching motion we use→ $C = [0 \quad 0 \quad 0 \quad 0]$, $D = [0 \quad M_{\delta e}]$

Next, on the same plot, the bode diagram of each isolated system is constructed. The following figure shows the bode diagram for the SkyHunter. The figure was constructed for the elevator as the input. A similar plot can be made for the thrust as the input. The plots were created using MATLAB.

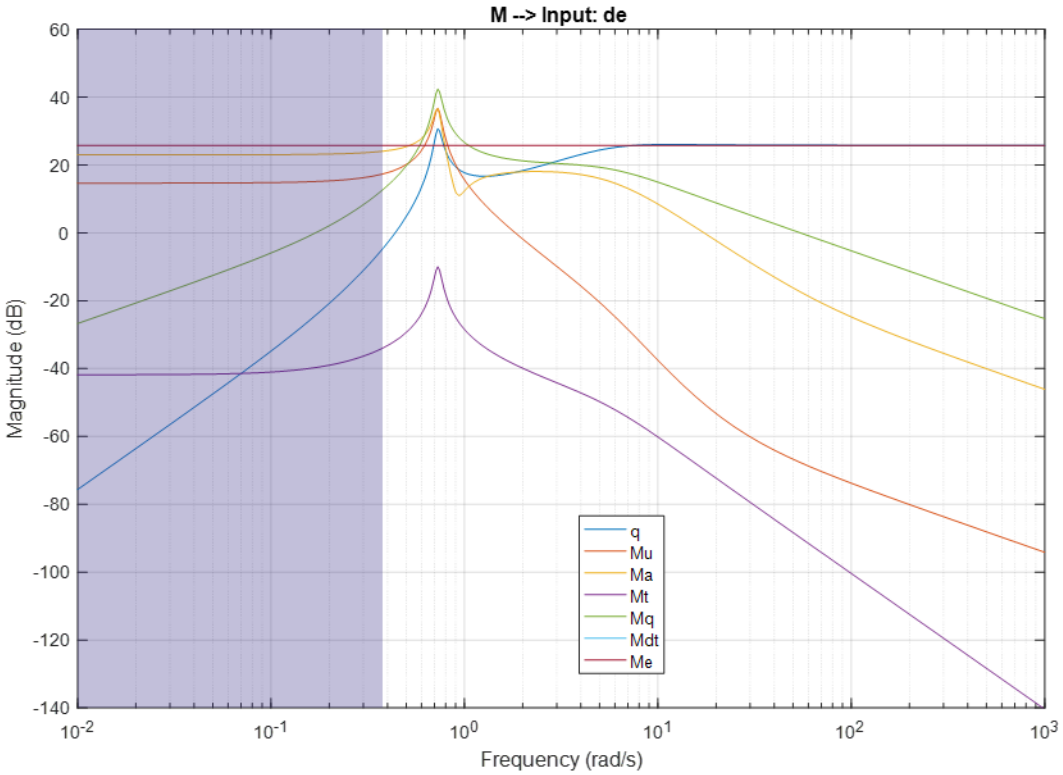

Figure 4-1: Bode diagram of dynamic models related to pitching moment with elevator as the input.

The developed bode diagram can be used to specify the frequencies at which each moment dimensional derivative is identifiable. This can be done as follows: first we note that

based on the diagram, at each frequency, we can make one of three judgments concerning each term (ex: $Mu, M_{\alpha}, ...$):

1. The term is **identifiable** at that frequency
2. The term is **identifiable only as a ratio of other terms** at that frequency
3. The term is **not identifiable** at that frequency

A term is **identifiable** when:

(a) its magnitude is at least 10 % of the largest magnitude at that frequency

(b) its magnitude is greater than -3 dB

(c) the inertial term is larger than -3 dB.

A term is **identifiable as a ratio** when:

(a) its magnitude is at least 10 % of the largest term

(b) its magnitude is greater than -3 dB

(c) But the inertial term magnitude is less than -3 dB.

Other than these 2 conditions, the term is **not identifiable**. The reasoning used to know if a term is identifiable or not is obtained from References [8] and [28]. The -3dB was not specified numerically in these references. Instead it was mentioned that the magnitude has to be large enough. The following tree diagram presents the decision process.

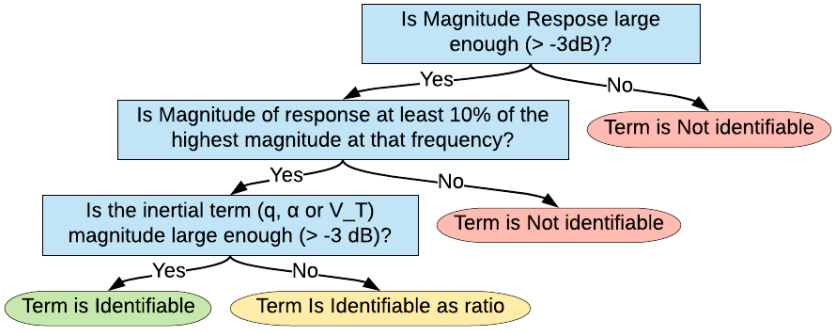

Figure 4-2: Tree diagram for deciding if a term is (a) identifiable, (b) identifiable as a ratio or (c) not identifiable, at a given frequency

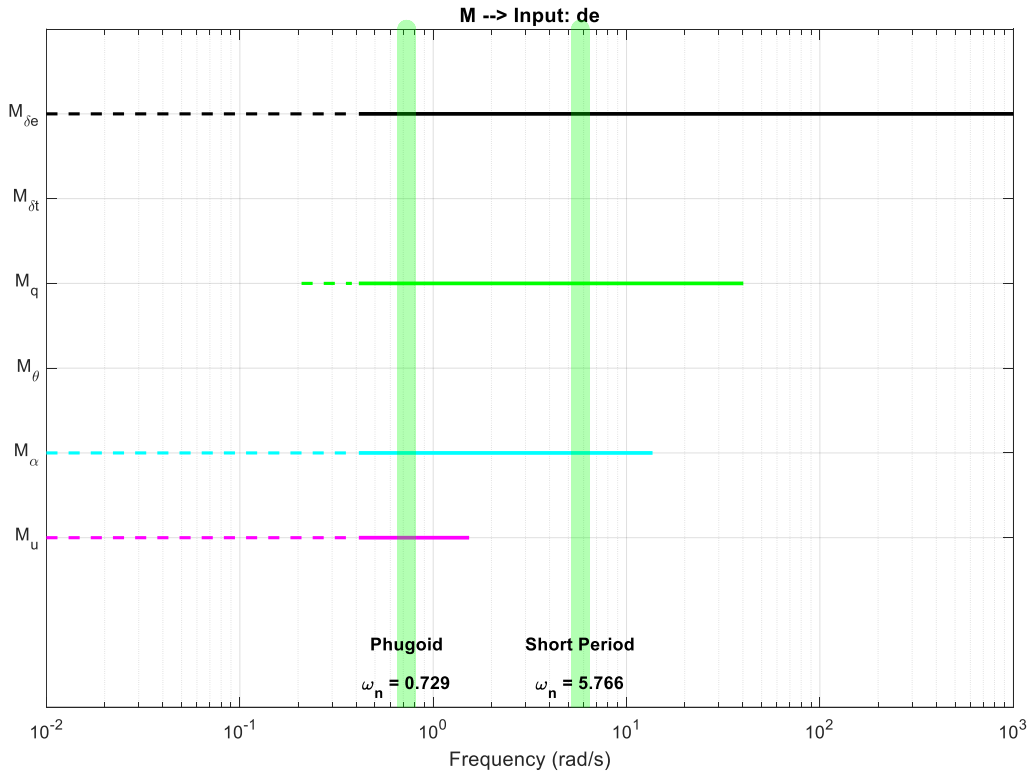

Figure 4-3: Diagram indicating frequencies at which moment derivatives are (a) identifiable [solid line], (b) identifiable as a ratio [broken line] (c) not identifiable [no line].

Figure 4-3 identifies the frequencies at which each moment term is identifiable. The way the plot can be understood is as follows. On the Y axis, the different dimensional derivatives are listed. On the X-axis is frequency in rad/s. Solid lines and broken lines run horizontally next to each derivative. A solid line indicates the derivative it is running next to is identifiable over the frequencies the solid line runs over. A broken line indicates the term is identifiable as a ratio of other terms. When no line is drawn, the term is not identifiable at that frequency.

For example, for the derivative M_q, No line is drawn at the frequencies 0.01 to 0.2 rad/s. This means the term cannot be identified when the aircraft is excited at that frequency. A broken line is drawn from 0.02 to 0.04 rad/s. Thus, the M_q derivative can be identified as a ratio of other derivatives (M_{de}, M_α, M_u) if the aircraft is excited at this frequency range. A solid line runs from

0.04 to 40 rad/s. Thus, the term is identifiable when the aircraft is excited at that range. The term will not be identifiable at higher frequencies since the no line is drawn.

It can be seen that all moment dimensional derivatives are identifiable in the region between about 0.4 to 10 rad/s. To add further perspective in the above figure, the phugoid mode and short period mode frequencies are marked using green lines. These frequencies are a bit different than ones in Section 3.5 since they were obtained from a different dynamic model version.

From the figure, a significant observation can be pointed out: all moment terms are identifiable if the system is exited at both the phugoid and short period frequencies. As Reference [8] points out, this is not surprising since “we know that the system excited at its natural mode will exhibit dominant dynamic motion”.

In fact, it is not just all the moment terms that are identifiable at the dynamic modes frequencies, all X and Z terms are also identifiable at these frequencies. This can be seen in the bode and identifiability diagrams of the X and Z axes. The plots were obtained following the same procedure used for the pitching moment discussed earlier. They are presented in the following four figures.

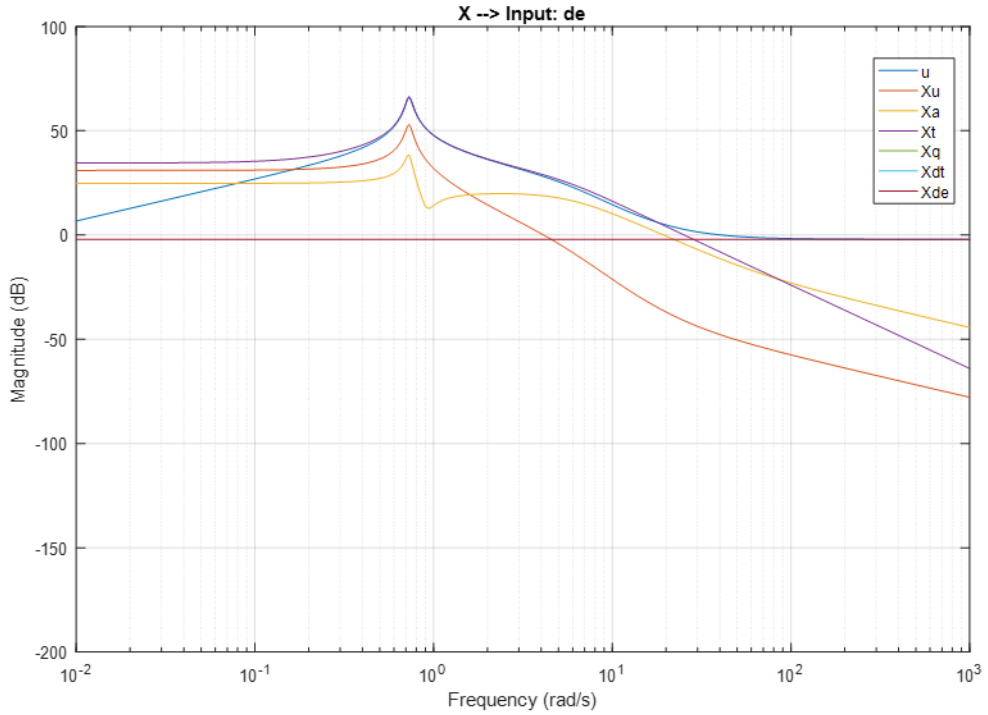

Figure 4-4: Bode diagram of dynamic models related to X-axis forces with elevator as the input.

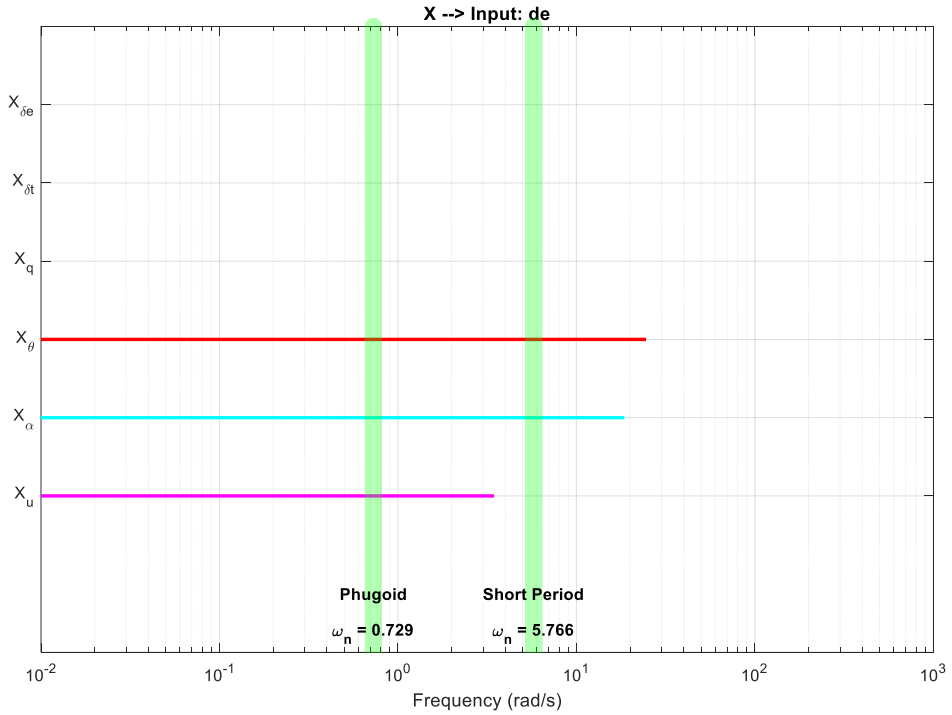

Figure 4-5: Diagram indicating frequencies at which X-axis derivatives are (a) identifiable [solid line], (b) identifiable as a ratio [broken line] (c) not identifiable [no line].

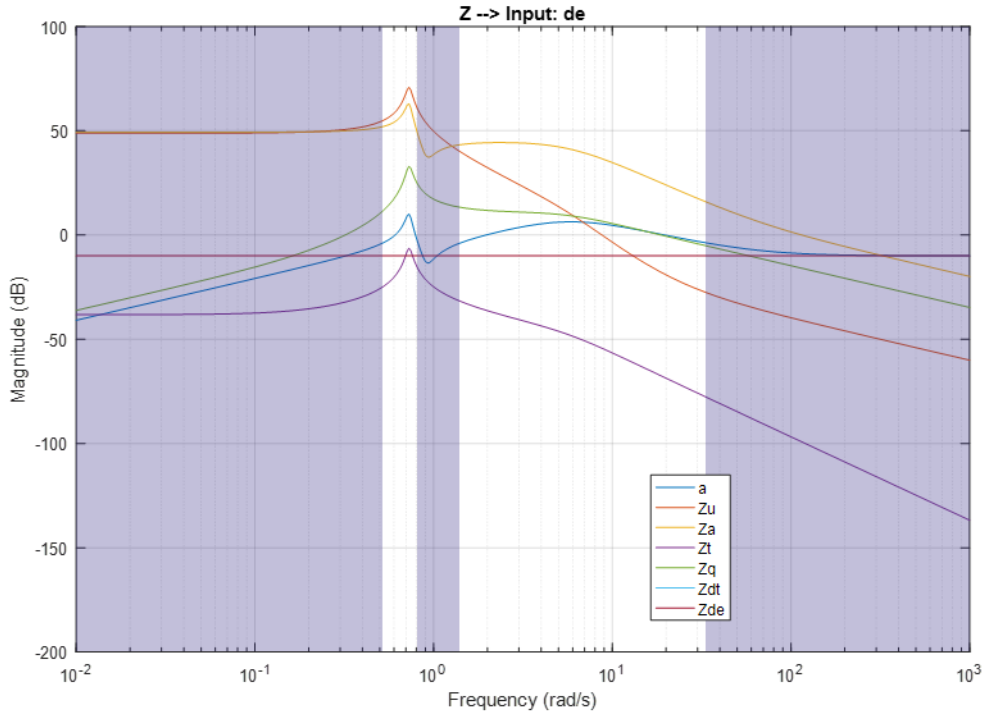

Figure 4-6: Bode diagram of dynamic models related to Z-axis forces with elevator as the input.

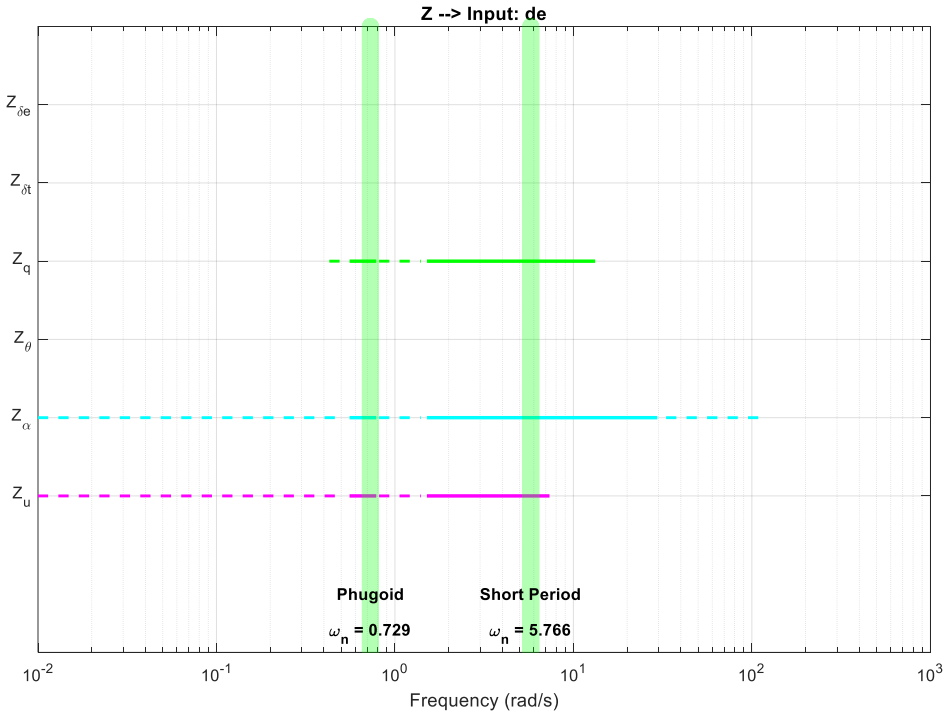

Figure 4-7: Diagram indicating frequencies at which Z-axis derivatives are (a) identifiable [solid line], (b) identifiable as a ratio [broken line] (c) not identifiable [no line].

In the bode diagram of Figure 4-1, the shaded region indicates that the inertial term (q) is less than -3 dB. Thus, the terms are either identifiable as a ratio or not identifiable in this region.

Based on the above discussion for the SkyHunter, to identify all the terms of the LTI model, the following conclusion is made:

Step 1 conclusion:

EXCITE THE SKYHUNTER AT THE PHUGOID FREQUENCY (0.729 RAD/S) AND THE SHORT PERIOD FREQUENCY (5.766 RAD/S)

4.1.2 Step 2: Design input signal that excites specified frequencies

At this point, the frequencies that the aircraft needs to be exited at are known. The second step discussed here is: what the multistep input signal should look like to excite these frequencies. Reference [8] discusses this in detail and the following is a much less detailed presentation. Three input signals are discussed below.

First, the simplest of input signal designs: **a pulse input**. This constitutes of a small sudden change in the input, then holding that input constant for a time Δt, then suddenly bringing the input to the original amplitude and holding it there. The energy spectrum of such input is concentrated about zero rad/s. Changing the Δt duration has an effect of increasing or decreasing the range of excited frequencies. When the range of excited frequencies increases the energy level decreases, and vice versa. (A diagram of the pulse input is available in Table 4-1)

Another simple input signal is the **doublet**. It constitutes of a small sudden increase in amplitude to +Δu, followed by a small sudden decrease in amplitude to -Δu ,then bringing the amplitude suddenly to the original value. Here Δu is the magnitude of deviation from the original control input. Thus, the maximum amplitude (+Δu) and minimum amplitude (-Δu) have the same deviation from the original input value but they go at opposite directions. Each of the first 2

input changes are held for the same duration, Δt. When the duration Δt changes, the frequency at which energy is concentrated varies. As Δt gets smaller higher frequencies get excited. However, the energy spreads over a larger frequency range and the peak energy gets lower. The choice of Δt when designing a signal is made such that the frequency we desire to excite satisfies the equation: $\omega\Delta t = 2.3$. Here ω is the frequency we desire to excite in rad/s. (A diagram of the doublet input is available in Table 4-1)

A bit more complex signal is the **"3-2-1-1" signal**. The name of that signal is derived from its shape. The signal constitutes of suddenly changing the signal with value Δu, suddenly bringing it down by value $2\Delta u$, then up $2\Delta u$, then down Δu to return to the original signal value. All changes are instantaneous. The duration each change is maintained is $3\Delta t, 2\Delta t, \Delta t, \Delta t$ – Thus, the name of the signal 3-2-1-1. A main advantage of the 3-2-1-1 signal is the spread of the power spectrum. Choice of Δt for the signal is made such that the frequency the signal is designed to excite lies at the middle or at the upper third of the bandwidth. These two points correspond to $(\omega\Delta t)_{mid} = 1.6$ and $(\omega\Delta t)_{2/3} = 2.1$. (A diagram of the 3-2-1-1 input is available in Table 4-1)

Table 4-1 summarizes the discussed input signals and presents the advantages and disadvantages of each. The previous discussion was constrained only to three widely used input signals. However, other input signals have been used and studied in the literature.

Since a pulse input excites low frequencies, it is suitable for exciting the phugoid mode. Modes with higher frequencies, such as the short period mode, would be better excited using a doublet input or a 3-2-1-1 input. Reference [8] recommends using a 3-2-1-1 signal for exciting the short period and a doublet input for exciting the Dutch roll mode. The reference makes this recommendation for the Dutch roll mode instead of the 3-2-1-1 since the Dutch roll mode is

more lightly damped compared to the short period mode. Thus, a doublet input is adequate for exciting it. Also, the reference states that the duration and exact shape of the doublet maneuver for exiting the Dutch roll mode is of secondary importance.

Table 4-1: Comparison between advantages and disadvantages of each input type.

Input Signal	**Signal Shape**	**Advantages**	**Disadvantages**
Pulse		• Simple	• System excited asymmetrically • Input is less fitting for exciting high frequency modes
Doublet		• Simple • System excited symmetrically • Frequency at which energy is concentrated varies with Δt	• Small bandwidth (1:3)
3-2-1-1	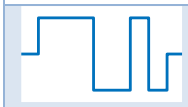	• Large bandwidth • Frequency at which energy is concentrated varies with Δt	• During first section ($3\Delta T$) aircraft may go far from trim • Hard to implement input manually on a UAS when time step is small (<1 sec)

Now, back to discussion on the doublet and 3-2-1-1 signals. It was mentioned that there are specific equations that are used when designing a doublet or 3-2-1-1 signal. For a doublet input, if we desire to excite the frequency ω, then we choose Δt such that it satisfies the following equation.

$$\omega \Delta t = 2.3 \qquad \text{Eq 4-5}$$

Similarly, for a 3-2-1-1 input, if we desire to excite the frequency ω, we choose Δt such that is satisfies either of the following two equations.

$$(\omega \Delta t)_{mid} = 1.6 \qquad \text{Eq 4-6}$$

$$(\omega \Delta t)_{2/3} = 2.1 \qquad \text{Eq 4-7}$$

Note: in the previous equations, ω is frequency in rad/s.

For example, to excite the short period frequency, ω_{SP}, using a doublet signal, we use the following Δt:

$$\Delta t = \frac{2.3}{\omega_{SP}} \qquad \text{Eq 4-8}$$

The following table shows the design Δt needed to excite the short period mode for the SkyHunter using a doublet or a 3-2-1-1 input.

Table 4-2: Time step for doublet and 3-2-1-1 maneuvers.

	Short Period Frequency	Period of Oscillation	$\boldsymbol{\Delta t_{doublet}}$ (Using Eq 4-5)	$\boldsymbol{\Delta t_{3211}}$ (Using Eq 4-6)	$\boldsymbol{\Delta t_{3211}}$ (Using Eq 4-7)
	rad/s	s	s	s	s
SkyHunter	5.76	1.091	0.40	0.28	0.36

The following table shows the design Δt to excite the Dutch roll mode for the SkyHunter.

Table 4-3: Time step for doublet and 3-2-1-1 maneuvers.

	Dutch Roll Frequency	Period of Oscillation	$\boldsymbol{\Delta t_{doublet}}$ (Using Eq 4-5)	$\boldsymbol{\Delta t_{3211}}$ (Using Eq 4-6)	$\boldsymbol{\Delta t_{3211}}$ (Using Eq 4-7)
	rad/s	s	s	s	s
SkyHunter	6.40	0.982	0.36	0.25	0.33

4.1.3 Magnitude

The previous section specified the time durations for the input signals used for system identification. In this section the magnitude at which the input signals should be applied is discussed. For example, when exciting the short period motion, how many degrees should the elevator be deflected up and down during the 3-2-1-1 maneuver?

To answer this question, simulation was made using the SkyHunter analytical model developed using AAA. Two pieces of information were found in Reference [8]:

1) In the short period excitation, "input amplitude should be such as to result in about $\pm 3°$ to 4° variation in angle of attack about the trimmed value, or in terms of the load factor the variation should be typically $\pm 0.4\ g$ to $0.5\ g$."
2) In the Dutch roll excitation, "the resulting maximum peak-to-peak variation in the angle of sideslip is typically of the order of $\pm 4°$ or $0.1\ g$ lateral acceleration"

These two points were used to specify a magnitude for the short period and Dutch roll maneuvers. The LTI models for the SkyHunter developed based on AAA modeling were simulated. The elevator angle was found to be about 3 degrees for the short period maneuver. The rudder angle was found to be about 1.5 degrees.

4.2 Input design Conclusions

In conclusion, to obtain good system identification results, it is important to gather good data from flight tests. The aircraft should be excited properly during the flight for the derivatives to be identifiable. To achieve this, specific flight maneuvers are designed for system identification.

For the SkyHunter longitudinal motion, the following is recommended:

EXCITE THE SKYHUNTER AT THE PHUGOID FREQUENCY (0.729 RAD/S) AND THE SHORT PERIOD FREQUENCY (5.766 RAD/S)

TO EXCITE THE SHORT PERIOD FREQUENCY (5.76 RAD/S):

APPLY A 3-2-1-1 SIGNAL OF $\Delta T = 0.3$ S ***TO THE ELEVATOR.***

THE CHANGE IN ELEVATOR ANGLE SHOULD BE ABOUT 3 ° ***IN EACH DIRECTION.***

EXCITING THE PUGOID MODE CAN BE DIFFICULT FOR THE SKYHUNTER. HOWEVER, A PULSE INPUT MAY BE A GOOD CHOICE FOR EXCITING IT.

This thesis focuses on longitudinal motion system identification. However, a Dutch roll maneuver that can be useful for lateral-directional system identification is presented below.

TO EXCITE THE DUTCH ROLL FREQUENCY (6.40 RAD/S):

APPLY A DOUBLET SIGNAL OF $\Delta T = 0.4$ S ***TO THE RUDDER***

THE CHANGE IN RUDDER ANGLE SHOULD BE ABOUT 1.5° ***IN EACH DIRECTION.***

5 EKF algorithm used for system identification

Several algorithms are available for aircraft parameter identification. References [2], [8]–[11] can be consulted for an overview of these methods. Some of the available algorithms are batch processing algorithms while other algorithms are recursive. Batch processing algorithms use all the available flight data at once to identify the aircraft model parameters. Recursive algorithms, aka sequential algorithms; use the available data point-by-point. In this thesis, an Extended Kalman Filter algorithm is used. It belongs to the recursive algorithms category. A main motivation in choosing the EKF algorithm was its potential to be used for online system identification since it is a recursive algorithm.

The EKF algorithm used in this thesis is obtained from Reference [8] and is presented in Section 5.1. Before using the EKF to obtain stability and control derivatives for the SkyHunter, verification that the EKF works properly was done by recreating the results of an example in Reference [8]. The recreation of this example is presented in Section 5.2.

5.1 Extended Kalman Filter Algorithm

This section presents the EKF algorithm including the main EKF equations, the postulated dynamic model, the measurement equations, the process and measurement noise covariance matrices and values used for initializing the filter.

5.1.1 Postulated Model

The postulated aerodynamic model used in the EKF is presented below. These equations were derived in Chapter 2. The goal of the system identification process is to estimate the stability and control derivatives written in bold in Eq 5-5 to Eq 5-7.

$$\dot{V} = -\frac{\bar{q}S}{m}C_D + \ gsin(\alpha - \theta) + \frac{F_T}{m}\cos(\alpha + \sigma_t) \qquad \text{Eq 5-1}$$

$$\dot{\alpha} = -\frac{\bar{q}S}{mV}\, C_L + q + \frac{g}{V}\cos(\alpha - \theta) - \frac{F_T}{mV}\sin(\alpha + \sigma_T) \quad \text{Eq 5-2}$$

$$\dot{\theta} = q \quad \text{Eq 5-3}$$

$$\dot{q} = \frac{\bar{q}S\bar{c}}{I_{yy}} C_m + \frac{F_T}{I_{yy}}(l_{tx}\sin\sigma_T + l_{tz}\cos\sigma_T) \quad \text{Eq 5-4}$$

Where,

$$C_D = \boldsymbol{C_{D_0}} + \boldsymbol{C_{D_V}}\frac{V}{V_0} + \boldsymbol{C_{D_\alpha}}\alpha \quad \text{Eq 5-5}$$

$$C_L = \boldsymbol{C_{L_0}} + \boldsymbol{C_{L_V}}\frac{V}{V_0} + \boldsymbol{C_{L_\alpha}}\alpha \quad \text{Eq 5-6}$$

$$C_m = \boldsymbol{C_{m_0}} + \boldsymbol{C_{m_V}}\frac{V}{V_0} + \boldsymbol{C_{m_\alpha}}\alpha + \boldsymbol{C_{m_q}}\frac{q\bar{c}}{2V_0} + \boldsymbol{C_{m_{\delta e}}}\delta_e \quad \text{Eq 5-7}$$

In the previous equations, V is the total velocity, α is the angle of attack, θ is the pitch angle and q is the pitch rate. $\bar{q}$ is the dynamic pressure, S is the wing reference area, m is the aircraft mass and g is the acceleration due to gravity. F_T is the thrust force, σ_T is the inclination of the thrust force from body X axis, l_{tx} is the x distance from propeller center to airplane center of gravity (CG) and l_{tx} is the z distance from propeller center to airplane CG. V_0 is the trim airspeed, which is taken to be the average airspeed over the analyzed flight portion. The dot notation means the time derivative (ex: $\dot{V}$ is the time derivative of V.) Work has been done to expand the above model to calculate more derivatives such as $C_{L_{\delta e}}, C_{L_q}$. This is discussed in Section 11.5.

5.1.2 Measurement Equations

There are 7 measurement equations used in the filter. They are listed below:

$$V_m = V \quad \text{Eq 5-8}$$

$$\alpha_m = \alpha \quad \text{Eq 5-9}$$

$$\theta_m = \theta \quad \text{Eq 5-10}$$

$$q_m = q \quad \text{Eq 5-11}$$

$$\dot{q}_m = C_m\frac{\bar{q}S\bar{c}}{I_{yy}} + \frac{F_T}{I_{yy}}(l_{tx}\sin\sigma_T + l_{tz}\cos\sigma_T) \quad \text{Eq 5-12}$$

$$a_{xm} = \frac{\bar{q}S}{m}\ C_X + \frac{F_T}{m}\cos\sigma_t \quad \text{Eq 5-13}$$

$$a_{zm} = \frac{\bar{q}S}{m}\ C_Z - \frac{F_T}{m}\sin\sigma_t \quad \text{Eq 5-14}$$

Where,

$$C_X = C_L \sin\alpha - C_D \cos\alpha \quad \text{Eq 5-15}$$

$$C_Z = -C_L \cos\alpha - C_D \sin\alpha \quad \text{Eq 5-16}$$

The subscript "m" stands for measurement. a_{x_m} and a_{z_m} are the measured accelerations in the airplane body X and Z axes. C_X and C_Z are the non-dimensional force coefficients in the aircraft body X and Z axes.C_L and C_D are the aircraft lift and drag coefficients.

5.1.3 EKF Equations

The EKF equations are presented below. Reference [8] can be consulted for a derivation of these equations.

Prediction step:

$$\tilde{x}(k+1) = \hat{x}(k) + \int_{t_k}^{t_{k+1}} f[\hat{x}(t), \bar{u}(k)]\, dt \quad \text{Eq 5-17}$$

$$\tilde{P}(k+1) \approx \Phi(k+1)\hat{P}(k)\Phi(k+1) + \Delta t Q \quad \text{Eq 5-18}$$

Initial Conditions:

$$\hat{x}(1) = x_0 \quad \text{Eq 5-19}$$

$$\hat{P}(1) = P_0 \quad \text{Eq 5-20}$$

Where,

$$\Phi(k+1) = e^{A(k)\Delta t} \quad \text{Eq 5-21}$$

$$A(k) = \left.\frac{\partial f[x(t), u(t)]}{\partial x}\right|_{x=\hat{x}(k)} = \begin{bmatrix} \partial f/\partial x & \partial f/\partial \Theta \\ 0 & 0 \end{bmatrix} \quad \text{Eq 5-22}$$

Correction step:

$$\tilde{y}(k) = g[\tilde{x}(k), u(k)] \quad \text{Eq 5-23}$$

$$K(k) = \tilde{P}(k)C^T[C\tilde{P}(k)C^T + R]^{-1} \quad \text{Eq 5-24}$$

$$\hat{x}(k) = \tilde{x}(k) + K(k)[z(k) - \tilde{y}(k)] \quad \text{Eq 5-25}$$

$$\hat{P}(k) = [I - K(k)C]\tilde{P}(k)[I - K(k)C]^T + K(k)RK^T(k) \quad \text{Eq 5-26}$$

Where

$$C(k) = \left.\frac{\partial g[x(t), u(t)]}{\partial x}\right|_{x=\tilde{x}(k)} = \left[\frac{\partial g}{\partial x} \quad \frac{\partial g}{\partial \Theta}\right]_{x=\tilde{x}(k)} \quad \text{Eq 5-27}$$

In the previous equations,˜ denotes predicted value.ˆ denotes updated value. ¯ denotes average of time steps k and $k+1$. The state vector, x, and the measurement vector, y, are defined as follows:

$$x = \begin{bmatrix} V \\ \alpha \\ \theta \\ q \\ C_{D0} \\ C_{DV} \\ C_{D\alpha} \\ C_{L0} \\ C_{LV} \\ C_{L\alpha} \\ C_{m0} \\ C_{mV} \\ C_{m\alpha} \\ C_{mq} \\ C_{m\delta e} \end{bmatrix}_{15\,X\,1}, \; y = \begin{bmatrix} V_m \\ \alpha \\ \theta_m \\ q_m \\ \dot{q_m} \\ a_{xm} \\ a_{zm} \end{bmatrix}_{7X1} \quad \text{Eq 5-28}$$

Notice that the state vector x consists of four aircraft motion states: V, α, θ and q. Following that are the 11 parameters we intend to estimate. In order to estimate the stability and control derivatives they were augmented to the state vector and the dynamic equations given to the EKF were also augmented with 11 equations. These equations are:

$$\dot{C_{D_0}} = 0, \dot{C_{D_V}} = 0, \ldots, \dot{C_{m_{\delta e}}} = 0 \quad \text{Eq 5-29}$$

In other words, it was assumed that the stability and control derivatives of the aircraft are constant over the duration of the analyzed flight portion.

5.1.4 Initial Process and measurement noise matrices

The process noise matrix, Q, used in this thesis was obtained from the code provided with Reference [8]:

$$Q = \begin{bmatrix} 1.2856 & 0 & 0 & 0 & 0 & \cdots & 0 \\ 0 & 0.0000059 & 0 & 0 & 0 & \vdots & \vdots \\ 0 & 0 & 0.00000020035203 & 0 & 0 & \vdots & \vdots \\ 0 & 0 & 0 & 0.00000301987933 & 0 & \vdots & \vdots \\ 0 & 0 & 0 & 0 & 0 & \vdots & \vdots \\ \vdots & \vdots & \vdots & \vdots & \vdots & 0 & \vdots \\ 0 & 0 & 0 & 0 & 0 & 0 & 0 \end{bmatrix}_{15\times 15} \quad \text{Eq 5-30}$$

The initial measurement noise matrix. $R,$ used in this thesis was obtained from the code provided with Reference [8] as follows:

$$R = \begin{bmatrix} 1.758\times 10^{-2} & 0 & 0 & 0 & 0 & 0 & 0 \\ 0 & 9.902\times 10^{-7} & 0 & 0 & 0 & 0 & 0 \\ 0 & 0 & 1.977\times 10^{-7} & 0 & 0 & 0 & 0 \\ 0 & 0 & 0 & 3.384\times 10^{-7} & 0 & 0 & 0 \\ 0 & 0 & 0 & 0 & 3.168\times 10^{-5} & 0 & 0 \\ 0 & 0 & 0 & 0 & 0 & 4.191\times 10^{-4} & 0 \\ 0 & 0 & 0 & 0 & 0 & 0 & 2.020\times 10^{-2} \end{bmatrix}_{7\times 7} \quad \text{Eq 5-31}$$

The measurement noise matrix was later modified for the SkyHunter as presented in Section 10.

5.1.5 Initializing the EKF

Two quantities need to be initialized for the EKF. These are the initial state vector x_0 and the initial covariance matrix P_0. For the SkyHunter, the initial state vector used by the EKF was obtained in one of 2 ways. For the first four states (V, α, θ, q) the initial value was set to be equal to the measured state at the initial time stamp of the analyzed flight data. For the stability and control derivatives, the initial state was set to be the estimate obtained from AAA.

The initial covariance matrix on the other hand was set to be a diagonal matrix with all elements on the diagonal equal to 10. This was done since the confidence in the initial state vector estimates was not high. Accordingly, the values in the initial covariance matrix needed to be large.

5.1.6 Measurements

The measurements for the observation vector were obtained from the sensors onboard the SkyHunter. An exception to this is the time derivative of the pitch rate, $\dot{q}$. This value was not measured. Instead, it was obtained by numerical differentiation from the pitch rate measurements.

5.2 Recreation of reference results using developed EKF

Reference [8] includes an example problem where flight data is provided and the above EKF formulation was used to estimate the stability and control (S&C) derivatives. This resource was used to verify that the EKF, independently coded for this thesis, was functioning properly. This was simply done by using the independently coded EKF to recreate the stability and control derivatives results presented in the reference. If the recreated results match the reference, then this gives confidence that the EKF was coded properly. If the recreated results do not match, then this indicates that there is some error. Indeed, the recreated results turned out to be matching to the reference estimates providing evidence that the EKF was coded properly. This comparison is presented in the following.

A table is provided below showing the final results from the coded EKF as compared to the final results presented in the reference. As can be seen, the developed EKF results were less than 5% different. The percentage difference is calculated using the following formula:

$$\%\, Differnce = 100 \times \frac{Devloped\ EKF - Refernce\ Final\ Value}{Refernce\ Final\ Value} \qquad \text{Eq 5-32}$$

Table 5-1: Recreation of example in Reference [8] was successful. The difference in values between recreated results and reference results is less than 5 %.

	Developed EKF	Reference Final Value	% Difference
C_{D_0}	0.124	0.124	0.00
C_{D_V}	-0.0657	-0.0652	0.77
C_{D_α}	0.3191	0.319	0.03
C_{L_0}	-0.0889	-0.0853	4.22
C_{L_V}	0.1493	0.144	3.68
C_{L_α}	4.2812	4.303	-0.51
C_{m_0}	0.1120	0.112	0.00
C_{m_V}	0.0047	0.0046	2.17
C_{m_α}	-0.9770	-0.971	0.62
C_{m_q}	-35.5059	-34.937	1.63
$C_{m_{\delta e}}$	-1.5529	-1.533	1.30

The data obtained from the reference included sensor measurements for 60 seconds from a German HFB-320 aircraft. In the above table, the values presented in the "Developed EKF" column are the results of the EKF at the end of the 60 seconds. In the following figures, the derivative estimates throughout the 60 seconds are presented. As the legends describe, the results from the EKF developed in this thesis are compared to the final time point result presented in Reference [8] which are presented in the second column of the above table.

C_D Derivatives:

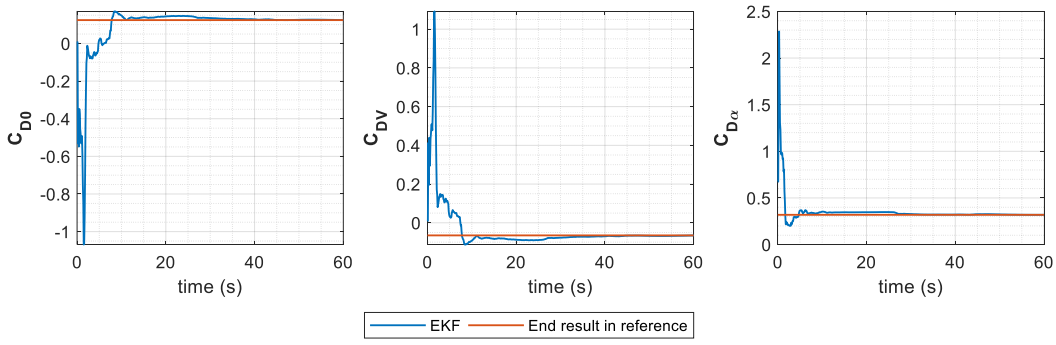

Figure 5-1: Drag stability and control derivatives recreated acceptably.

C_L Derivatives:

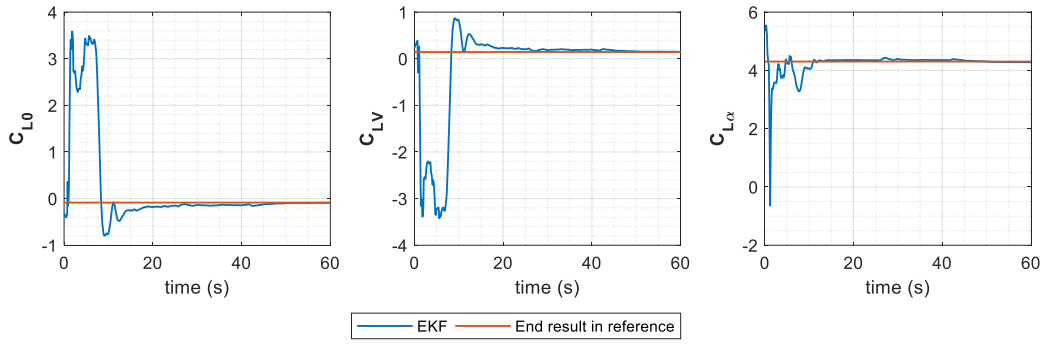

Figure 5-2:Lift stability and control derivatives recreated acceptably.

C_m Derivatives:

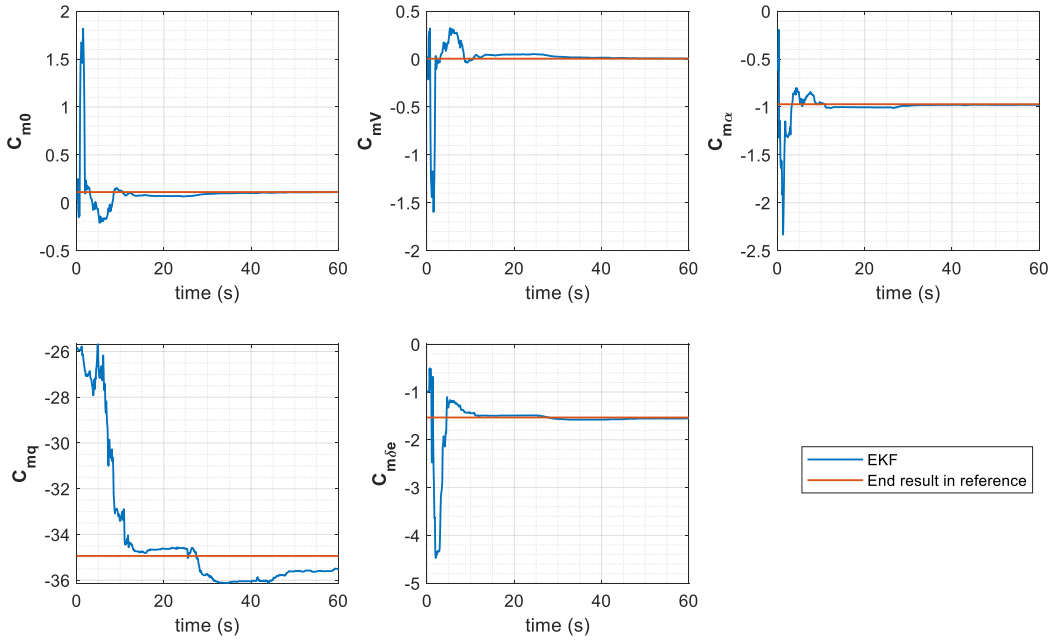

Figure 5-3: Pitching moment stability and control derivatives recreated acceptably.

It can be seen that the estimates start off being incorrect, but as the EKF runs, the derivative estimates converge and become very close to the reference estimates. This is an acceptable behavior for the EKF since it is a recursive algorithm. Therefore, the estimation gets better after a few points.

6 Initial system identification results for the SkyHunter

After validating that the EKF works properly by recreating the results of Reference [8], the EKF was applied to the SkyHunter. This Chapter presents the initial system identification results obtained from the SkyHunter. Section 6.1 Presents some of the initial results obtained from the SkyHunter. Section 6.2 then presents a discussion of these results and talks of the steps taken to improve the EKF results.

6.1 Initial SkyHunter System Identification results

The following table presents the EKF results for a flight portion from the SkyHunter. These are one of the first stability and control derivatives estimates for the SkyHunter. Figure 6-1 shows the EKF state estimation for the same flight portion.

Table 6-1 One of first system identification results obtained for SkyHunter

	AAA	**EKF**
C_{D0}	0.0265	0.41525
C_{DV}	0.1139	-0.3938
$C_{D\alpha}$	-0.346	0.58506
C_{L0}	0.5046	1.5735
C_{LV}	1.1735	-1.0354
$C_{L\alpha}$	5.8154	0.83875
C_{m0}	0.0442	7.3132
C_{mV}	0.0171	-15.932
$C_{m\alpha}$	-0.9749	-21.624
C_{mq}	-15.233	-355.02
C_{mde}	-1.0266	-69.338

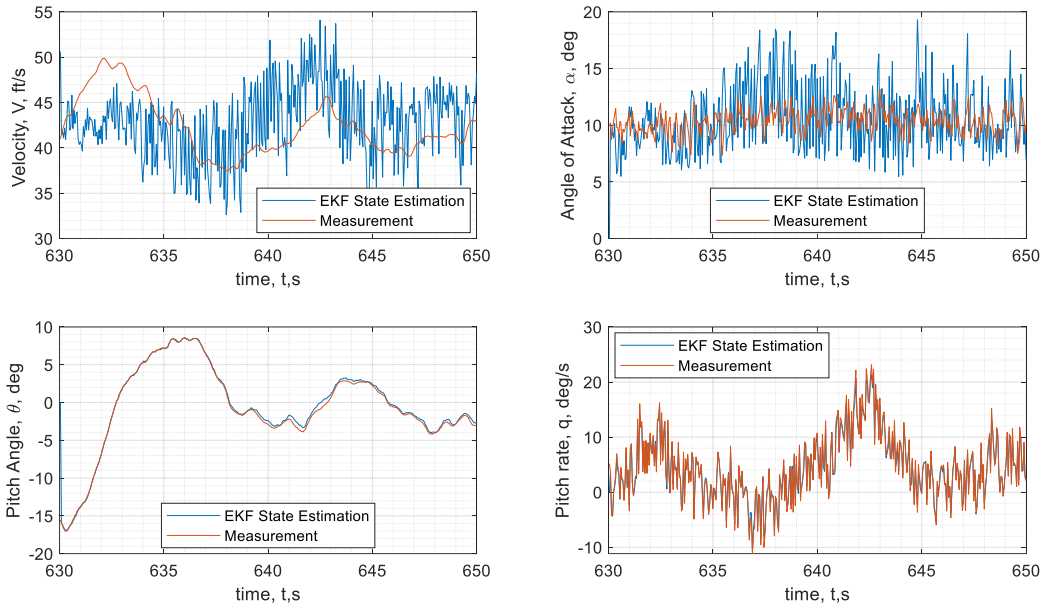

Figure 6-1: First results for SkyHunter had poor EKF state recreation.

In the following table, the results obtained from two additional flight portions are presented. This is done to evaluate whether the EKF yields consistent estimates from different flight portions

Table 6-2: Evaluation of EKF estimates from different flight portions

Source/ Flight Date	**AAA model**	**April 28 2018**	**April 28 2018**	**April 28 2018**
Flight No.		1	1	2
Analyzed Duration		20 s	104.5 s	6.5 s
Initial Time		630 s	695.5 s	324 s
Final Time		650 s	800 s	330.5 s
Flight Mode		RC	Auto	RC
Derivatives				
C_{D0}	0.0265	0.41525	5.7593	12.236
C_{DV}	0.1139	-0.3938	-5.8844	-12.289
$C_{D\alpha}$	-0.346	0.58506	1.5535	12.618
C_{L0}	0.5046	1.5735	31.351	32.71
C_{LV}	1.1735	-1.0354	-31.921	-32.747
$C_{L\alpha}$	5.8154	0.83875	6.9544	33.55
C_{m0}	0.0442	7.3132	-4.0577	-3.9621
C_{mV}	0.0171	-15.932	3.9312	3.5019
$C_{m\alpha}$	-0.9749	-21.624	-1.7997	-2.449
C_{mq}	-15.233	-355.02	-81.601	-55.937
C_{mde}	-1.0266	-69.338	-4.1111	-2.9717

6.2 Discussion of the initial results and outline of steps taken to improve them

Looking at the previous results, it can be seen that they are not acceptable. This can be seen in the following observations:

1) Looking at the results in Table 6-1, the estimated derivatives do not make sense in several cases. For example, $Cma = -21\,rad^{-1}$, $Cmq = -355\,rad^{-1}$, $Cmde = -69\,rad^{-1}$, $CmV = -15$ and $Cm0 = 7$. These values are very different from estimates based on AAA and are outside of expected bounds. (Expected bounds are presented in Section 11.1.3)
2) There is no consistency in the results. The stability and control estimates varied greatly depending on which flight portion was analyzed.
3) The EKF was not capable of recreating the measured states, as seen Figure 6-1.

In addition to inacceptable results observed in the EKF estimates. Two more observations were seen in the flight data.

4) The angle of attack measurements are very high (around 10°). This indicated that the angle of attack estimation algorithm may not be giving good estimation. Chapter 8 addresses this issue.
5) The data is noisy as seen in the plot of α and q. Chapter 7 discusses this issue in more detail.

To improve the EKF estimation and deal with the above-mentioned issues, several steps were taken. These steps are:

1) The EKF measurement noise covariance matrix, R, was adjusted.
2) Criteria were set in place to select suitable portions of flight to analyze. Note: the best way to perform system identification is to design proper flight maneuvers and analyze

data from these maneuvers. Chapter 4 discusses this process and presents flight maneuvers designed for the SkyHunter. Due to time and resource limitations, the maneuvers were not flown on the SkyHunter. Therefore, a different way was used to attempt to obtain acceptable flight portions. This alternative method is presented in Chapter 9.

3) Filters were used to remove noise form the flight data. This is discussed in Chapter 7.
4) Attempts to improve aircraft airflow angles estimation were made. As mentioned in Section 3.2, the SkyHunter does not have sensors to measure α and β values. Instead, an EKF is used to estimate these values. That αβ-EKF needed to be adjusted to extract more reasonable α values. This is discussed in Chapter 8.
5) Two more stability and control derivatives were estimated ($C_{L_{\delta e}}$ and C_{L_q}). Results were then compared to see if their addition improves the system identification results. This is discussed in Section 11.5.

7 Filtering Flight data

It was observed that some data collected from the SkyHunter contained high frequency noise. Thus, the data from the SkyHunter was filtered to remove this noise and obtain better system identification results. In this section, the raw data obtained from the SkyHunter are presented. The presence of noise is then identified. After that, several filtering techniques are presented. These techniques were compared together to see which is more suitable for application. A good filter would remove high frequency noise while maintaining the aircraft flight dynamics. The energy spectra obtained from the different filters is also presented in this chapter.

7.1 Flight data obtained from the SkyHunter

In this section, a portion of raw flight data from the SkyHunter is presented. The purpose in doing so is to point out the presence of noise in the data. Figures are presented for accelerations, rotation rates, velocity, airflow angles and Euler angles. For each of these measurements a comment is given whether it needs filtering.

7.1.1 Accelerations

The following figure shows the accelerations measured in the body $X, Y\ and\ Z$ axes. The first figure shows data for 12 seconds of flight. The second figure zooms in on the first 2 seconds to better identify the noise.

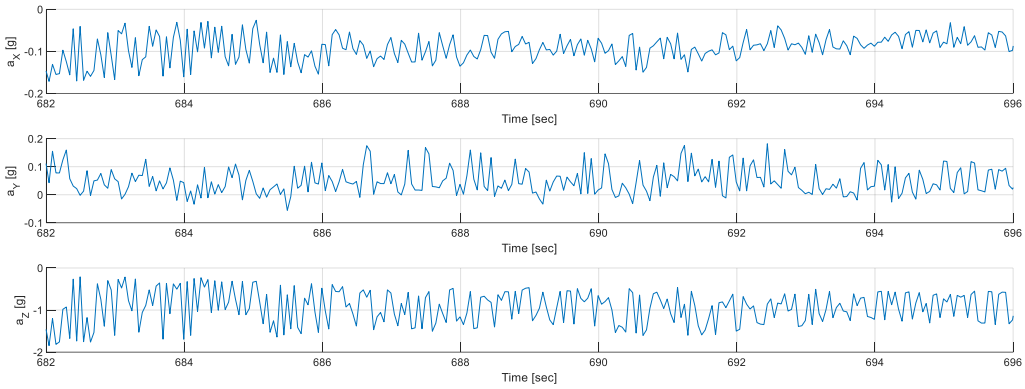

Figure 7-1: Sample of acceleration (a_x, a_y, a_z) flight data.

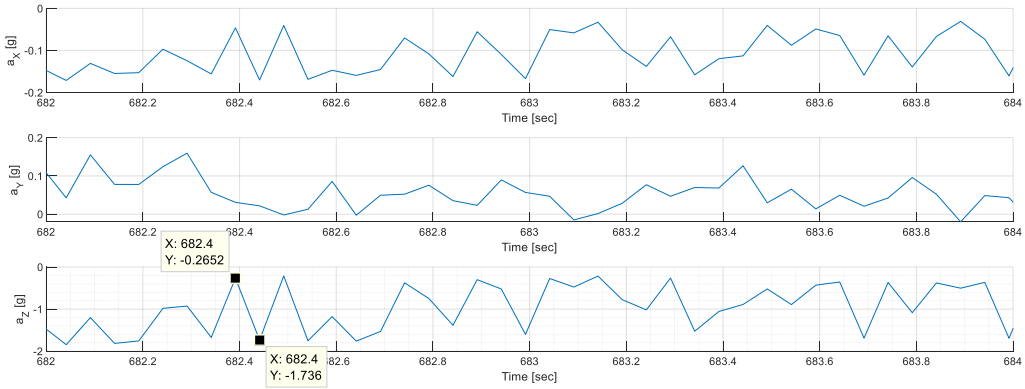

Figure 7-2: A zoomed in view of 2 seconds of acceleration data.

Notice the two identified data points in Figure 7-2. In less than 0.1 second (in 0.05 seconds), the Z axis acceleration went from -0.2652 g to -1.736 g. This is a very large change. 1.47 g change in 0.05 seconds! This indicates that there is high noise in the data and it is occurring at high frequency.

7.1.2 Rotation rates

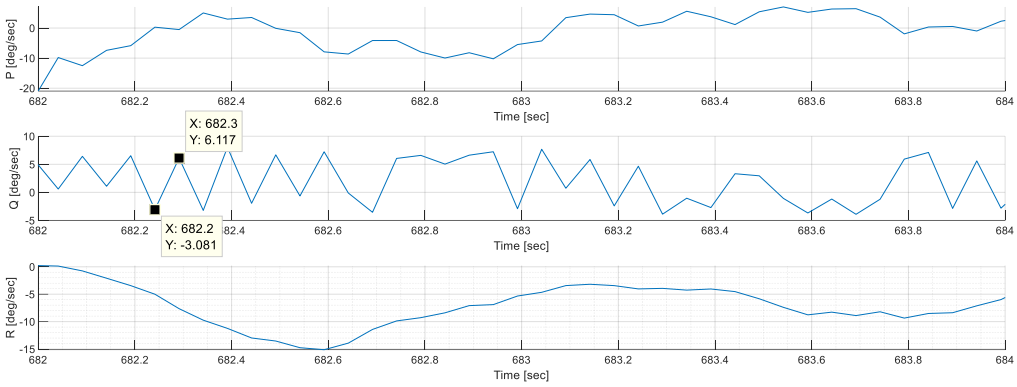

Figure 7-3: Sample of body rotation rates (p, q, r) flight data. High noise observed in q.

The previous figure shows the body rotation rates for the same 2 second time portion. Looking at the pitch rate, the graph shows a zig-zag shape with the vertex points of the zigzag being spaced 1 sample point away from each other (0.05 sec). This corresponds to a frequency of $f = \frac{1}{0.05} = 20\ hz$, which is much higher than the expected dynamic modes frequencies of the SkyHunter or fixed-wing aircraft in general. Fixed-wing aircraft usually have dynamic mode frequencies no higher than 5 Hz [21]. Thus, the pitch rate appears to have high frequency noise. The roll and yaw rates (p and r) do not show the same magnitude of oscillation. At least not in this flight portion.

7.1.3 Airspeed and airflow angles

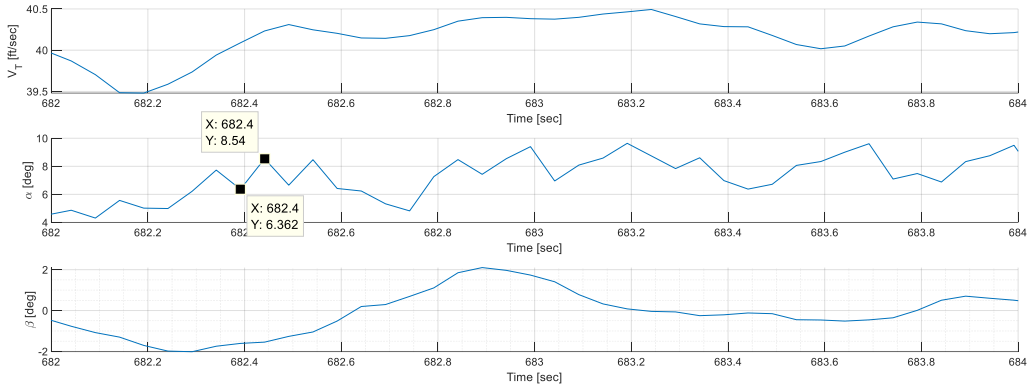

Figure 7-4: Sample of airspeed (V) and airflow angles (α, β) flight data. Angle of attack may have high frequency noise.

In the previous figure, plots for the airspeed and airflow angles are presented. Looking at the airspeed plot, the graph seems smooth. No high noise oscillations are visible. However, looking at the angle of attack plot. High frequency oscillation is visible around the time stamp $t = 682.4\ s$. The angle of attack changes about 2 degrees in 0.05 seconds. This corresponds to a rate of change of $40°/sec$! However, other portions of the angle of attack plot are less oscillatory. Thus, angle of attack was initially filtered. However, later on, it was observed that the system identification results are better when the angle of attack is not filtered as will be presented in Section 11.2.

7.1.4 Euler angles

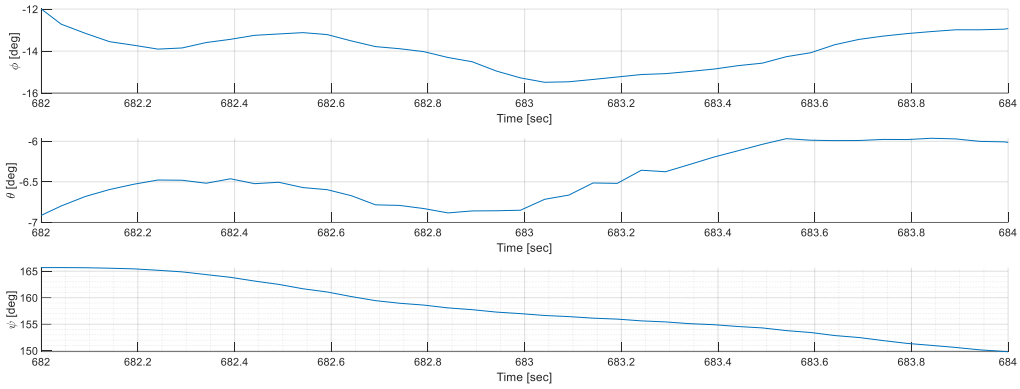

Figure 7-5: Sample of Euler angles (ϕ, θ, ψ) flight data.

The Euler angles are presented in the previous plot. The plots are mostly smooth. Thus, they were not filtered in this thesis.

7.1.5 Summary of analysis

From the above plots, it can be noted that accelerations, rotation rates and airflow angles may require filtering to remove high frequency noise. Airspeed and attitude angle data seem to be acceptable

7.2 Tested filters

Several digital filters were considered to remove the noise from the signals. Care had to be given to choose a suitable filter. We desire only to remove the noise without altering the actual signal. If the actual signal is altered, that means the aircraft dynamics would be altered and the system identification results would not be accurate. Thus, different filters were tested. The following is a list of the tested filters:

1) Spencer filters (15- point and 21-point variants were tested. However, results are only presented for the 15-point filter in this section)
2) Low pass filter

3) Moving average filters (a wide range of window sizes was used including: 15, 21, 31, 41, 51, and 61-point filters. In this thesis, for the most part, results are only presented for the 21-point filter.)

7.2.1 The Spencer filters

The 15 and 21-point Spencer filters were obtained from Reference [8]. The Spencer filters are a kind of low pass filter that belong to the class of weighted moving average filters. More references about these 2 filters are in [29], [30] . The formulas for the 15-point and 21-point filters are presented below. These filters are symmetric filters. This means that the filter uses an equal number of points before and after the current time stamp when calculating filtered values. This can be seen easily in the equations.

Formula for 15-point Spencer filter:

$$y_i = \frac{1}{320}[-3u_{i-7} - 6u_{i-6} - 5u_{i-5} + 3\,u_{i-4} + 21u_{i-3} + 46u_{i-2} + 67u_{i-1} + 74u_i + 67u_{i+1} + 46u_{i+2} + 21u_{i+3} + 3\,u_{i+4} - 5u_{i+5} - 6u_{i+6} - 3u_{i+7}] \quad \text{Eq 7-1}$$

Formula for 21-point Spencer filter:

$$y_i = \frac{1}{350}[-u_{i-10} - 3\,u_{i-9} - 5\,u_{i-8} - 5\,u_{i-7} - 2\,u_{i-6} + 6\,u_{i-5} + 18\,u_{i-4} + 33\,u_{i-3} + 47\,u_{i-2} + 57\,u_{i-1} + 60\,u_i + 57\,u_{i+1} + 47\,u_{i+2} + 33\,u_{i+3} + 18\,u_{i+4} + 6\,u_{i+5} - 2\,u_{i+6} - 5\,u_{i+7} - 5\,u_{i+8} - 3\,u_{i+9} - u_{i+10}] \quad \text{Eq 7-2}$$

In the above equations, y is the filtered quantiy, u is the unfiltered quantity (i.e. the raw measurements), the subscript i indicates the current time stamp, $i + n$ indicates the time stamp n points in the future or n points in the past if n is negative.

7.2.2 The low pass filter

The used low pass filter was designed using MATLAB digital filter design toolbox [31]. It was designed to filter high frequency noise while maintaining low frequencies of interest. The

analytical model for the SkyHunter, developed using AAA software, which was mentioned in Chapter 3, was used to estimate the frequencies of the SkyHunter dynamic modes. For convenience, the following table presents the short period and phugoid frequencies for the different SkyHunter dynamic models.

Table 7-1: Longitudinal frequencies of the different SkyHunter dynamic models. The highest frequency is bolded.

Aircraft Model	**Units**	**SkyHunter 2 w/ winglets**		**SkyHunter 3 No winglets**	**SkyHunter 4 No winglets**
Wing airfoil		GOE 438	Clark Y	Clark Y	Clark Y
ω_{SP}	Hz	0.896	0.796	0.7901	0.7257
$\omega_{Phugoid}$	Hz	0.114	0.125	0.1263	0.1184

From the above table it can be seen that the highest longitudinal mode frequency is 0.896 Hz. Rounding that number to 1 Hz (a conservative rounding) then the Nyquist frequency is 2 Hz (2 times the highest frequency of interest.) Thus, the low pass filter was designed to maintain all frequencies up until 2 Hz. Then the filter was designed to gradually filter out higher frequencies until it reaches 4 Hz. Any frequency above 4 Hz would be filtered out. The following figure shows the designed filter response.

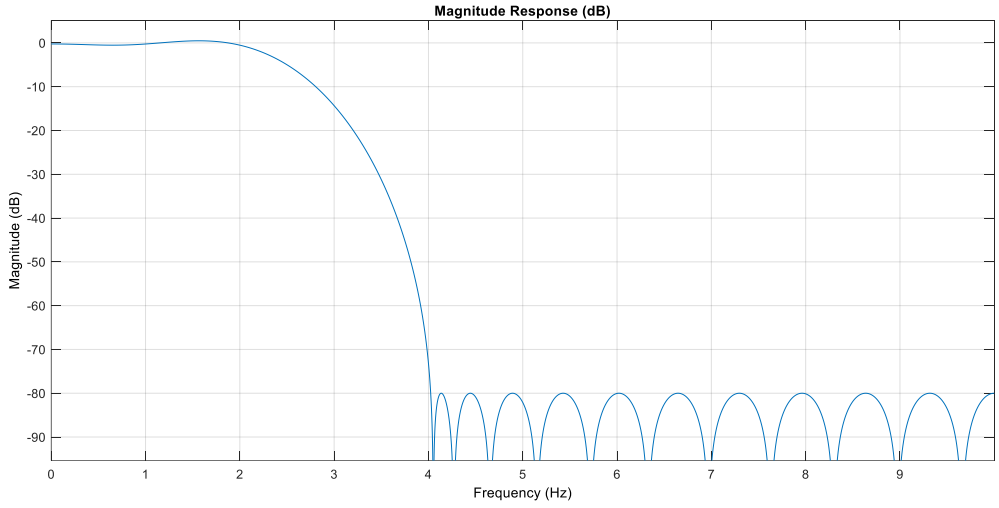

Figure 7-6: Designed magnitude response of the low pass filter.

The formula for such a low pass filter is:

$$\begin{aligned} y_i = \Big[& \frac{49}{58370}u_{i-13} + \frac{370}{103969}u_{i-12} + \frac{22}{2599}u_{i-11} + \frac{83}{6256}u_{i-10} \\ & + \frac{163}{12808}u_{i-9} + \frac{31}{20525}u_{i-8} - \frac{216}{10703}u_{i-7} - \frac{170}{4039}u_{i-6} \\ & - \frac{111}{2437}u_{i-5} - \frac{271}{20659}u_{i-4} + \frac{158}{2707}u_{i-3} + \frac{370}{2459}u_{i-2} \\ & + \frac{1704}{7453}u_{i-1} + \frac{571}{2202}u_i + \frac{1704}{7453}u_{i+1} + \frac{370}{2459}u_{i+2} \\ & + \frac{158}{2707}u_{i+3} - \frac{271}{20659}u_{i+4} - \frac{111}{2437}u_{i+5} - \frac{170}{4039}u_{i+6} \\ & - \frac{216}{10703}u_{i+7} + \frac{31}{20525}u_{i+8} + \frac{163}{12808}u_{i+9} + \frac{83}{6256}u_{i+10} \\ & + \frac{22}{2599}u_{i+11} + \frac{370}{103969}u_{i+12} + \frac{49}{58370}u_{i+13} \Big] \end{aligned} \qquad \text{Eq 7-3}$$

7.2.3 The moving average filters

The moving average filters were designed to be symmetric filters. It is simple to arrive at a formula for a moving average filter. For a $(2n+1)$-point moving average symmetric filter the formula would be:

$$y_i = \frac{1}{2n+1}[u_{i-n} + \cdots + u_{i-2} + u_{i-1} + u_i + u_{i+1} + u_{i+2} + \cdots + u_{i+n}] \qquad \text{Eq 7-4}$$

For example, a 21-point moving average filter will have the formula:

$$\begin{aligned} y_i = \frac{1}{21}[& u_{i-10} + u_{i-9} + u_{i-8} + u_{i-7} + u_{i-6} + u_{i-5} + u_{i-4} + u_{i-3} + u_{i-2} \\ & + u_{i-1} + u_i + u_{i+1} + u_{i+2} + u_{i+3} + u_{i+4} + u_{i+5} + u_{i+6} \\ & + u_{i+7} + u_{i+8} + u_{i+9} + u_{i+10}] \end{aligned} \qquad \text{Eq 7-5}$$

7.3 Application of filters to flight data

The following two figures shows the different filters applied to pitch rate (q) measurements obtained from flight data. The flight portion about 9 seconds long. Figure 7-7, shows the time history of the original signal verses the filtered signals. Figure 7-8, shows the power spectra of these signals. These figures were generated using MATLAB Signal processing toolbox [32].

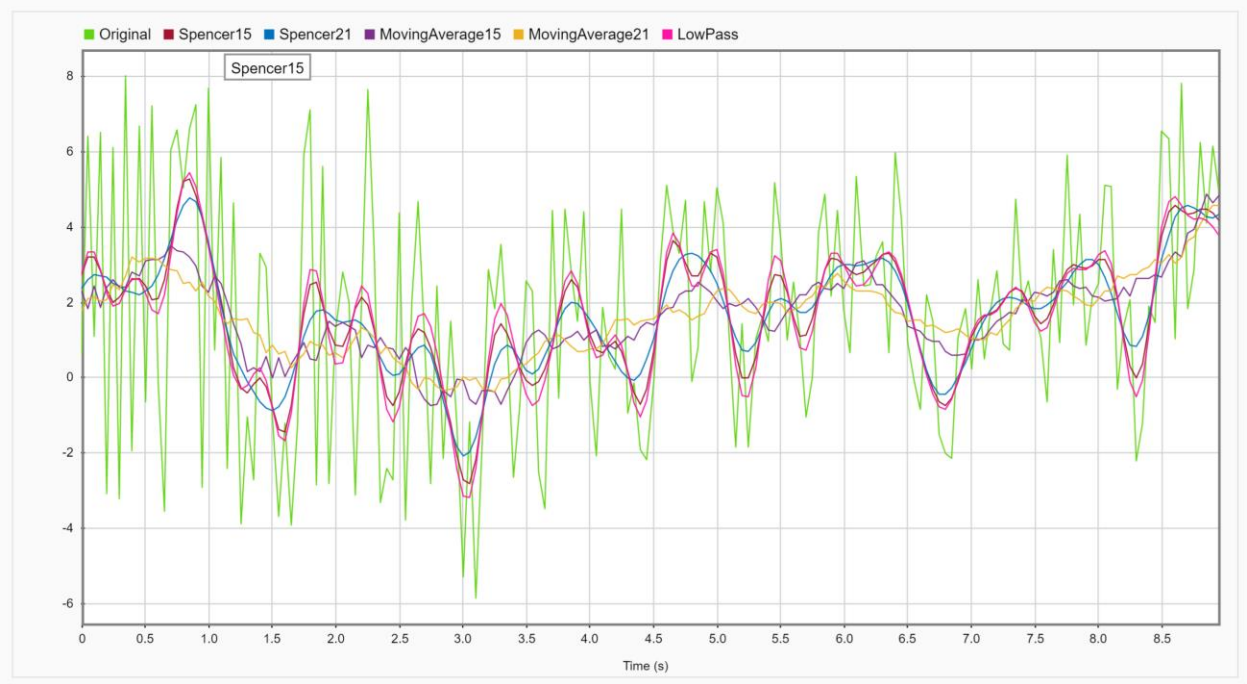

Figure 7-7: Using 9 seconds of pitch rate data, the performance of several filters is compared to the original signal.

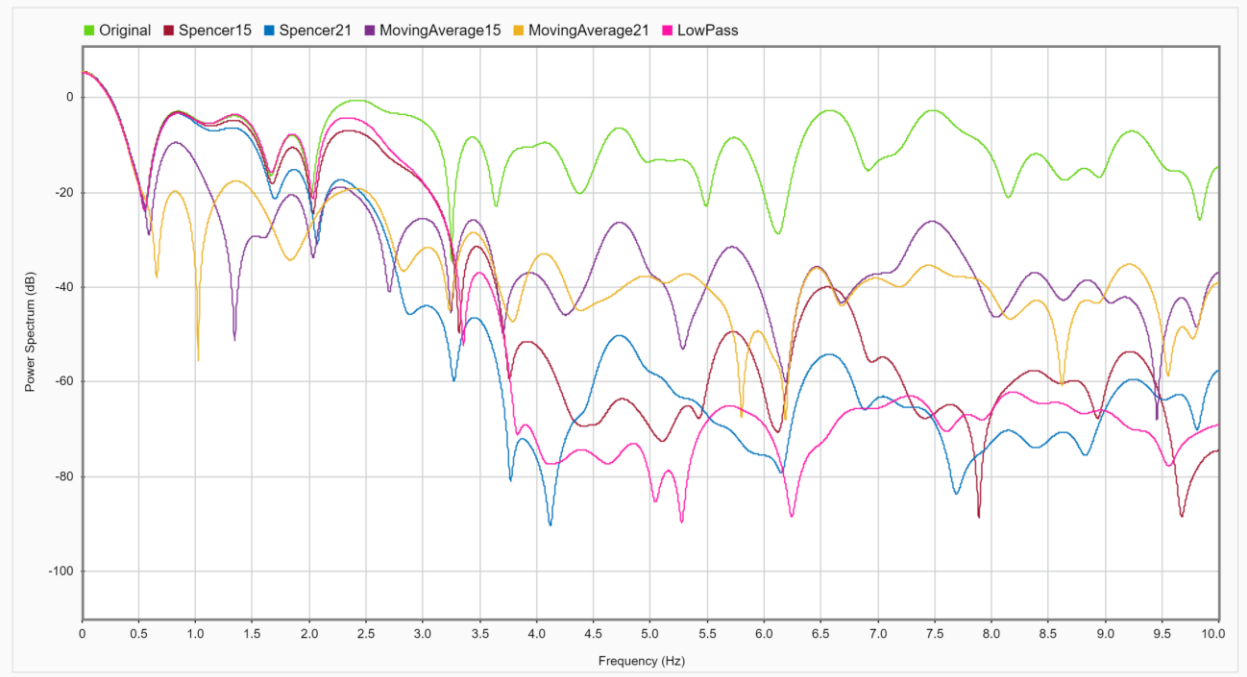

Figure 7-8: The power spectra of the original signal verses the filtered signals. (Same data as previous figure.)

From Figure 7-7, the following can be observed:

1) It can be seen that all filtering methods did reduce the magnitude of the high frequency oscillations.
2) The low pass filter and the Spencer filters show much smoother plots than the moving average filters. In the moving average filters the plots have many sudden changes in slope.
3) In terms of tracking, the Spencer filters and the low pass filter track the original signal more closely. They have higher peaks and lower troughs in order to follow the original signal. The moving average filters on the other hand tracks the signal less closely. This can be clearly seen, for example, around $t = 0.8\ s$ and $t = 3\ s$. In these instances, the moving average filter may be failing to capture the true dynamics of the aircraft.

In the power spectra plots of Figure 7-8, 10 Hz is the maximum value on the X-axis. This is because the sampling frequency is 20 Hz. Hence, the Nyquist frequency is 10 Hz. and it is not possible to properly capture frequencies higher than that. Looking at the plots, it can be seen that:

1) The original signal had noticeable power all the way from 0 Hz to 10 Hz. This again is an indicator of the presence of noise, since aircraft dynamics are usually at 5 Hz or lower [21].
2) The low pass filter works as it was intended to. The filter response is similar to that presented in Figure 7-6, where, starting at 2 Hz the filter starts to cut out the frequencies until it reaches 4 Hz and anything above 4Hz is filtered out.
3) The Spencer filters follow a similar pattern as the low pass filter.
4) The low pass filter does the best job in cutting out frequencies higher than 4 Hz. The spencer 21 starts to cut out low frequencies earlier than the Spencer 15 filter.

5) The moving average filters start cutting out frequencies around 0.5 Hz. This is not a good behavior since frequencies of interest in system identification are being filtered out. In addition, the high frequencies are not well removed by the moving average filter.

Based on the above observations, it can be concluded that:

- The low pass filter and the Spencer filters are better at capturing the aircraft dynamics and filtering out noise.
- The moving average filters are filtering out some potentially important frequencies and are not filtering out the unimportant frequencies well.
- Thus, using the moving average filter may make the system identification results inaccurate.

With that said, system identification results are still presented from the moving average filter since they seemed to be more reasonable in some instances than the low pass and Spencer filters. System identification results obtained from data filtered using the low pass filter, the Spencer 15 filter and the moving average 21 filter are presented in the following sections. The effect of using the different filters on system identification results are discussed in these sections.

8 Modification made to airflow angle estimation.

Many aircraft use estimation techniques to obtain angle of attack estimation. Equipping aircraft with airflow angle sensors and calibrating these sensors can be difficult and the obtained measurements may end-up being inaccurate [33]. Thus, estimation of airflow angles in aerospace engineering is common place.

The SkyHunter uses an Extended Kalman Filter algorithm to estimate airflow angles. This EKF will be referred to as $\alpha\beta$-EKF in this thesis to avoid confusion with the EKF used for system identificaiton. The $\alpha\beta$-EKF mainly uses the following two information sources to estimate the airflow angles:

1) Measured flight data: the algorithm uses acceleration measurements, rotation rate measurements, airspeed measurement and control inputs (elevator, aileron, rudder and thrust).
2) Dynamic model information: this includes the aircraft stability and control derivatives and estimated aircraft trim condition information. The trim condition information includes: trim control surface angles, trim angle of attack and side slip angle, trim rotation rates, trim throttle and trim flight speed.

It was observed that the trim elevator and trim angle of attack in particular can affect the angle of attack estimation of the EKF. Depending on the given trim elevator and angle of attack, the estimated alpha can be shifted higher or lower. Thus, attention was given to use proper values for these two trim values. Section 8.1 presents an analysis related to alpha trim. Section 8.2 Presents an analysis related to elevator trim.

8.1 Trim angle of attack

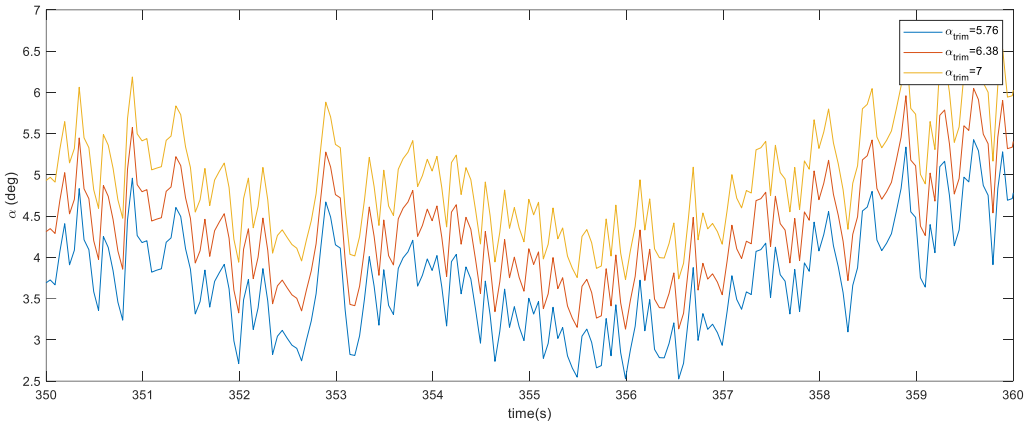

Figure 8-1: Effect of trim angle of attack on angle of attack estimation.

In the previous figure, three different alpha trim values are used. It can be seen that as α_{trim} increases, the estimated angle of attack curve shifts upwards. Thus, a good estimate of α_{trim} for the SkyHunter is needed for proper estimation of angle of attack. One way to obtain such a value is to equip the SkyHunter with an airflow angle sensor to measure the angle of attack then fly the aircraft in trim condition and evaluate the trim angle of attack. While this method may yield good results, it is expensive and difficult to achieve. Another method to estimate the trim angle of attack is to obtain it from the analytical models obtained from AAA and presented in Chapter 3. This second method was used in this thesis.

Table 8-1: Trim angle of attack and elevaor angle for the threoretical models of the SkyHunter. Information, duplicated from Chapter 3

Quantity	**Units**	**SkyHunter 2 w/ winglets**		**SkyHunter 3 No winglets**	**SkyHunter 4 No winglets**
Estimated wing airfoil		GOE 438	Clark Y	Clark Y	Clark Y
Trim angle of attack, α_{trim}	$deg.$	2.73	6.38	7.82	5.09
Trim elevator deflection, de_{trim}	$deg.$	1.5	-0.79	-1.58	2.8

The trim angle of attack obtained from the different AAA models was between 2.5° and 8°, as seen in the previous table. The models based on the updated models that use the Clark Y airfoils have angles between 5° and 8°. In this thesis, all system identification results are based on the SkyHunter 2. As will be seen in Chapter 11, system identification results are presented

with the $\alpha\beta$-EKF using $\alpha_{trim} = 5.76°, 6.38°$ and 7°. The remaining results in that chapter use $\alpha_{trim} = 6.38$, which is the AAA trim value for SkyHunter 2 using Clark Y airfoil.

8.2 Trim elevator angle

Similar to the previous discussion related to alpha trim, the estimated angle of attack depends on the value of trim elevator given to the $\alpha\beta$-EKF. The estimated angle of attack shifts upwards or downwards depending on the trim elevator value. This can be clearly seen in the following figure, which shows estimated angle of attack based on different trim elevator values.

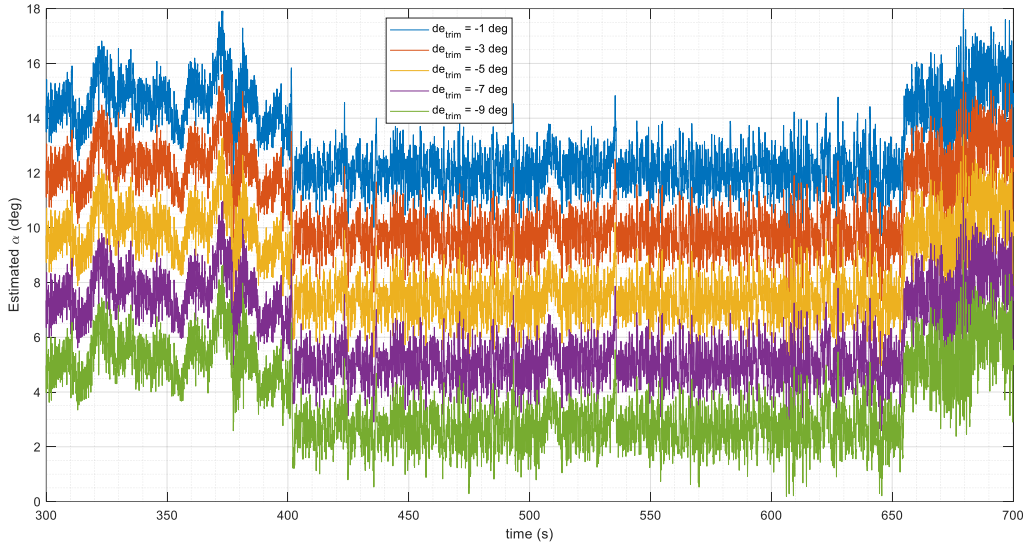

Figure 8-2: Effect of trim elevator angle on angle of attack estimation.

It can be seen that as the trim elevator angle increases (becomes less negative) the estimated angle of attack increases. Table 8-1, shows the trim elevator value obtained from different AAA models of the SkyHunter. The range of trim values in the table is $-1.58° \leq de_{trim} \leq 2.8°$. Flight data showed that the trim elevator value can possibly be $-9°$ sometimes. This is why the previous figure shows α estimation based on large negative trim values.

8.2.1 Using constantly changing de_{trim}

An important thing to consider is that during flight there is usually more than one trim condition. Therefore, there may be a need to constantly update the trim elevator value in order to obtain proper α estimation at all trim conditons. Consider the recorded elevator angle over the duration of a complete flight, shown in the following figure.

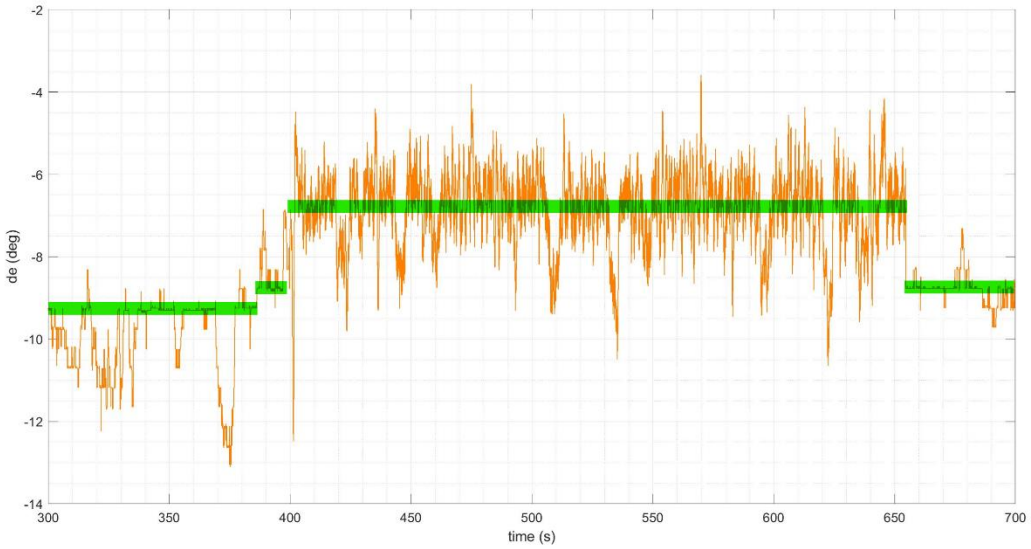

Figure 8-3: Recorded elevator angle over the duration of a complete flight. Green lines are estimation of de_{trim} at different times.

Green lines are drawn on the figure to show where trim elevator values are expected to be. It can be seen that different portions of the flight had different trim elevator angles. A noticeable change in trim value can be seen at $t \approx 400\ s$ and $t \approx 650\ s$. These two values mark the beginning and ending of autopilot flight.

Since the trim elevator is constantly changing during flight, using a single trim elevator angle may be inadequate. To address this issue, a moving window filter was used to obtain the trim elevator value based on the recorded elevator input angle. The window length was a design

parameter. A short window made the elevator trim value always equal to the elevator input. A very large window made the filter incapable of capturing changes in trim value quick enough. The following two figures illustrate these two cases.

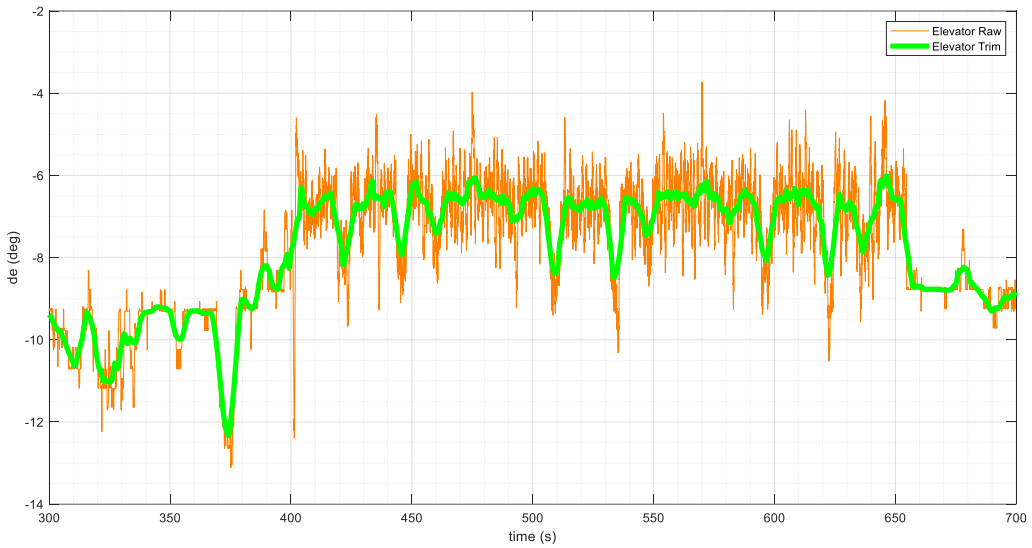

Figure 8-4: Window too small (5 sec). The trim elevator is always equal to the current elevator angle.

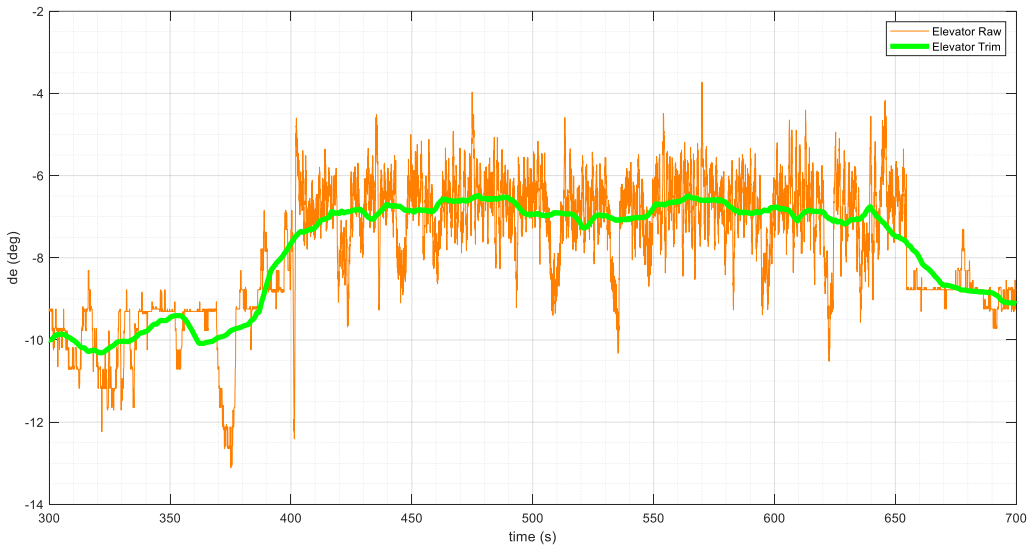

Figure 8-5: Window too large (30 sec). We are not capturing changes in trim elevator quick enough. (As seen in 650 to 700 sec regions, for example.)

For the previous flight, after experimenting with different window sizes, a window size of 20 second was seen to be a good compromise. The trim elevator, based on the 20 second window, is presented in the following figure. It can be seen that the elevator trim value adjusted to be similar to the desired trim value presented using the green lines in Figure 8-3.

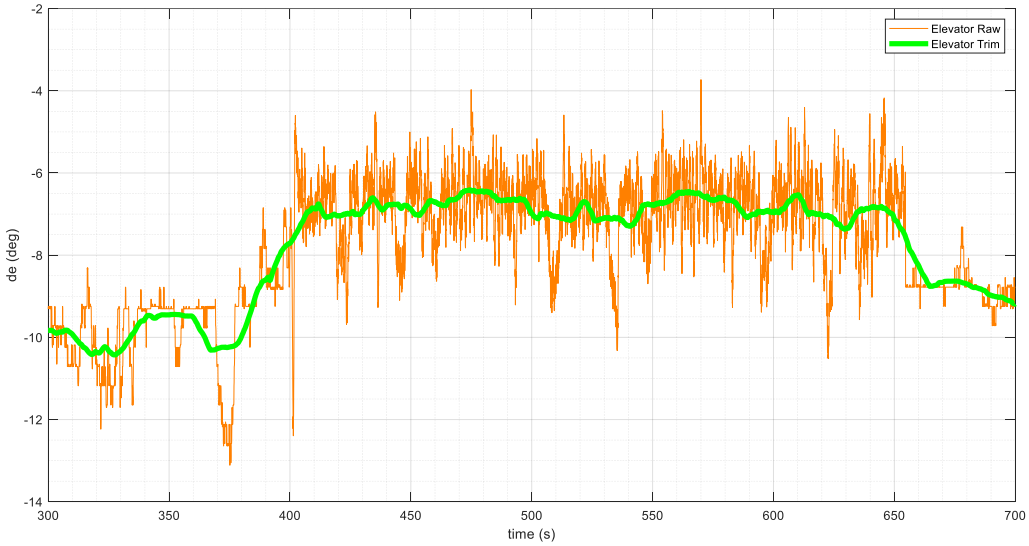

Figure 8-6: Acceptable window size (20 s). A compromise between having a too large or too small window.

The following figure shows the obtained angle of attack estimation when the 20 s moving average was used to get de_{trim}, (see the yellow line). The figure also shows the angle of attack estimation when de_{trim} is a constant value. (The blue line uses de_{trim}=-9°, the red line uses de_{trim}=-7°). It can be seen that the blue and red lines show a sudden drop of about 2 degrees at t=400s then a sudden increase at about t=650s. The yellow estimation remained in the same angle of attack region (oscillating about $\alpha \approx 4.5°$) without showing a sudden drop or rise. The difference in angle of attack can be about 2-4 degrees between the different estimates (as seen in the portion before t=400s. Four degrees can be significant in determining whether the aircraft is near stall or not. If the constant de_{trim} was off by several degrees, the difference in angle of attack can even be higher than 4 degrees.

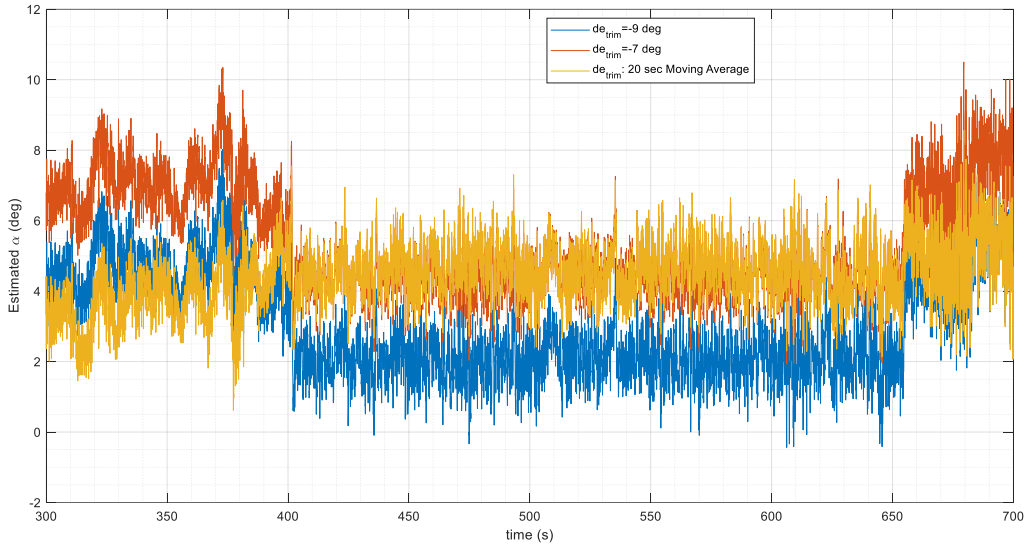

Figure 8-7: Angle of attack estimation obtained when $\alpha\beta$-EKF was using (a) de_{trim}=-9°, (b) de_{trim}=-7°, (c) a moving average trim elevator value.

In the Section 11.2.1, comparison is made between the system identification results using the different alpha estimates.

9 Selecting flight portions for system identification

As mentioned in Section 6.2, the best way to perform system identification is to use flight data from specially designed flight maneuvers. Designing such maneuvers is discussed in Chapter 4. Flight maneuvers for the SkyHunter are also presented in that chapter. Due to several circumstances, the flight maneuvers were not flown on the SkyHunter. An alternative method was used to attempt to obtain suitable flight portions for analysis from flight data that is already available. That method was to set criteria for choosing flight portions to analyze. These criteria are discussed in this chapter.

The model being identified, given in Eq 5-1 to Eq 5-7, is a simplified model as discussed in Chapter 2. It is not possible to identify the stability and control derivatives properly if the aircraft violates the assumptions of the model being identified. Therefore, some criteria needed to be in place when selecting flight portions to analyze… Criteria that allow the flight portions to comply with the simplifying assumptions of the equations of motion. Two sets of criteria were identified for flight portions that are acceptable to analyze. These criteria are presented in the following sections.

9.1 Set of Criteria #1

The first set of criteria is presented in this section. Section 11.2 presents the system identification results obtained based on this set of criteria. The first set of criteria is:

1) **The flight needs to have near constant thrust**

This criterion is used to avoid having errors in the estimated derivatives. Errors may arise due to at least two factors if the thrust was not constant. First, the thrust force is not measured for the SkyHunter. Instead, a thrust model is used to obtain the thrust in lb. from the commanded thrust setting. (Note: the commanded thrust setting is a value between 0 and 1 with 0 being minimum thrust and 1 being maximum thrust.) Inaccuracies in this thrust model would result in

inaccuracy in the thrust force, in lb. Second, during system identification, when evaluating a term like $C_{m_{de}}$, if the thrust changes simultaneously with the elevator, it can be harder to evaluate the effect of $C_{m_{de}}$ independently.

2) The flight needs to have low roll angle ϕ

Actual aircraft dynamics have coupling between lateral motion and longitudinal motion. The simplified equations of motion (Presented in Section 2.13) assume that the lateral and longitudinal motion are decupled. For this to be true, the roll angle needs to be small. Thus, the criterion for low ϕ angle. If the roll angle is high, then the aircraft will be experiencing dynamics that are not captured in the simplified equations of motion.

Looking at the equations of motion used in the EKF, it can be seen that the sine and cosine functions are used with the roll angle, ϕ. Analysis was made to see what ϕ angle range can be considered small enough for using the simplified equations of motion. Figure 9-1, which is a plot of the cosine curve, was made to make this analysis as follows: If we assume that the cosine angle is negligible, i.e. $\phi \approx 0$. Then, this means that $\cos(\phi) \approx 1$ and $\sin(\phi) \approx \phi$. From the figure, the following is noted:

- Up until $15°$, the cosine of an angle is less than 5% different than 1, which is the assumed value of $cos\phi$ under small angle assumption.
- Up until $26\ °$,the cosine of an angle is less than 10% different than 1.

Thus, when selecting flight portions to analyze, $\pm\ 15°$ was taken to be the **ideal** range for ϕ. For simplicity, $\pm\ 25\ °$ was taken as an **acceptable** range for ϕ. This allowed longer flight portions to be acceptable.

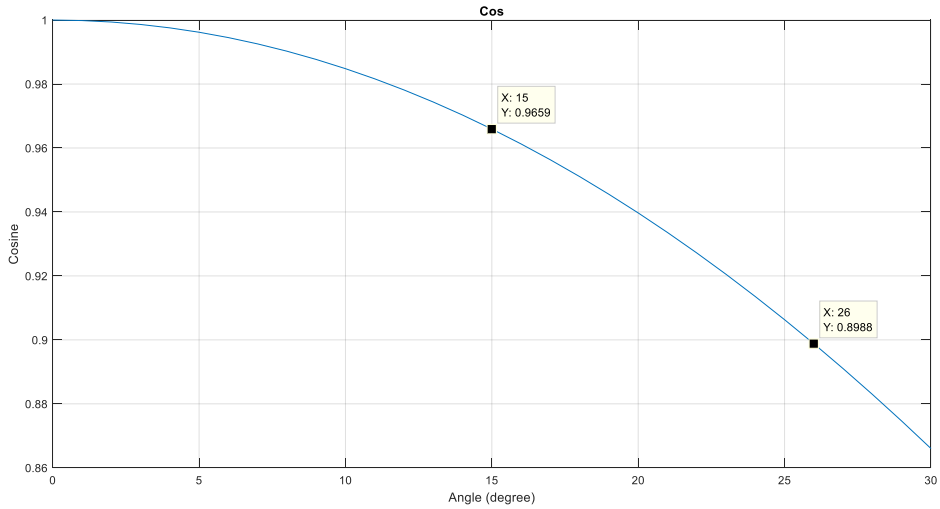

Figure 9-1: Cosine fuction evaluated up till 30°.

3) The flight needs to have small deviation in airspeed

The aircraft stability and control derivatives are only valid for a defined trim condition. If the trim condition changes, the stability and control derivatives change as well. Therefore, the air speed should not be varying significantly. It should be around a trim value. Quantitatively, the criterion of small deviation in airspeeds was set that the airspeed should not have a variation greater than $\pm$ 15 ft/s peak-to-peak.

4) The flight must be in manual mode.

In system identification, we desire to capture the dynamics of the aircraft itself. If an autopilot is constantly in control of the aircraft and adjusting its motion, then we may capture the dynamics of the aircraft and the autopilot together. This is why a criterion was specified to have the flight in manual mode instead of autopilot mode. However, even in manual mode, the pilot is commanding the aircraft and correcting its motion. Thus, we may end up capturing the dynamics of the aircraft and human pilot together. However, assuming that the human pilot is likely to have a lower rate of sending commands to the UAS, we can think that using manual flight may allow us to capture the aircraft dynamics better.

5) **The flight portion must be long enough for analysis.**

It is important for the flight portion to be longer than a few seconds. The EKF needs to have a long enough portion in order to have enough data to converge at a proper estimate.

9.2 Set of Criteria #2

Set of criteria # 2 specify that the flight portion must:

1) **Have low rotation rates** $(\boldsymbol{p}, \boldsymbol{q}, \boldsymbol{r})$ **,** $[\boldsymbol{-20°, 20°}]$**.**
2) **Have low roll angle,** $\boldsymbol{\phi}$ **,** $[\boldsymbol{-30°, 30°}]$**.**
3) **Have low Pitch angle,** $\boldsymbol{\theta}$ **,** $[\boldsymbol{-20°, 20°}]$**.**
4) **Be longer than three seconds.**
5) **Be in manual mode.**

In Section 2.13, the aircraft equations of motion were simplified by assuming the lateral-directional motion variables: β, p, r and ϕ are all constant at zero (or small enough to be unimportant). To satisfy the equations of motion used in system identification, the requirements of low p, r and ϕ were added in the criteria. β is usually not larger than 10 degrees in the SkyHunter flights.

Having low θ makes the aircraft closer to straight line level flight. We want to obtain stability and control derivatives for that flight mode. Low q reduces unsteady aerodynamics. Criterion 4 allows having some continuity in the analyzed flight. Criterion 5 was discussed in the previous section.

Note: the requirements of having near constant thrust and small variation in flight speeds are not part of this second set of criteria. Adding these two criterions would make it difficult to find long enough flight portions that satisfy set of criteria # 2.

System identification results based on flight portions matching this set of criteria are presented in Section 11.3.

9.3 Stitching Flight Data

A code was written to extract all flight portions that match the second set of criteria from a given flight log. Flight portions satisfying set of criteria # 2 were not very long. Many times, the flight portions were less than 5 seconds. Therefore, flight data that matched the criteria were stitched together to form one longer segment of flight. This stitched data was then provided to the EKF for system identification. Only portions satisfying criteria #2 that are longer than 3 seconds were stitched. This is so that there is enough continuity in the data to perform system identification.

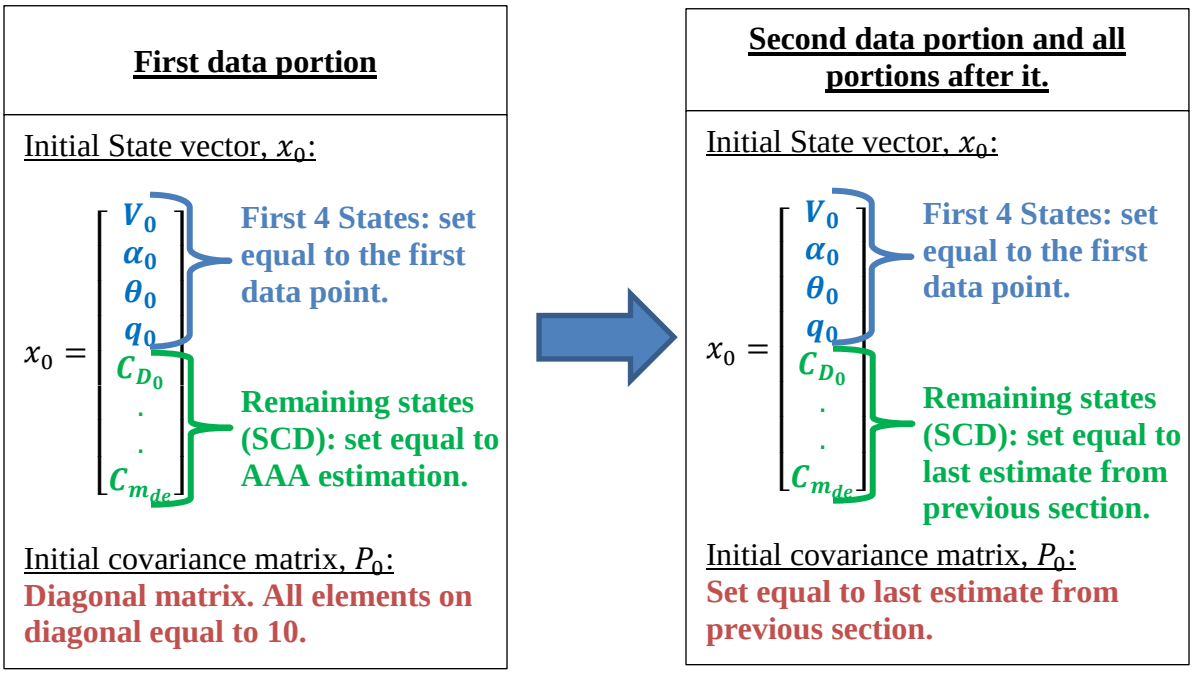

Figure 9-2: How the system Identification EKF functions at stitching points.

Attention was given to how the system identification EKF handles points where data is stitched. The diagram in Figure 9-2 explains the process. For the first data portion, the EKF runs as it would normally and as described in Section 5.1.5. Then at every point where a new section starts, the EKF is initialized a bit differently. The first four states in x_0 are initialized to be equal to the flight data. The remaining states (the derivatives) are set to be equal to the last estimates

from the previous section. The covariance matrix P_0 is also set to be equal to the last covariance P from the previous data section. Using this method allowed having continuity in EKF results between stitched portions.

The following sections present the data used for stitching in this thesis. Three flights are presented, and the flight portions used for system identification are shown. The system identification results based on these stitched data is then presented in Section 11.4.

9.3.1 Stitched data obtained from Flight A

The following figure shows the altitude plot of a SkyHunter 2 flight. This was the first flight for the SkyHunter on April 28, 2018. This flight will be referred to as Flight A. In the figure, the green parts are the parts that were chosen for stitching. These were parts that matched set of criteria # 2 and were longer than 3 seconds.

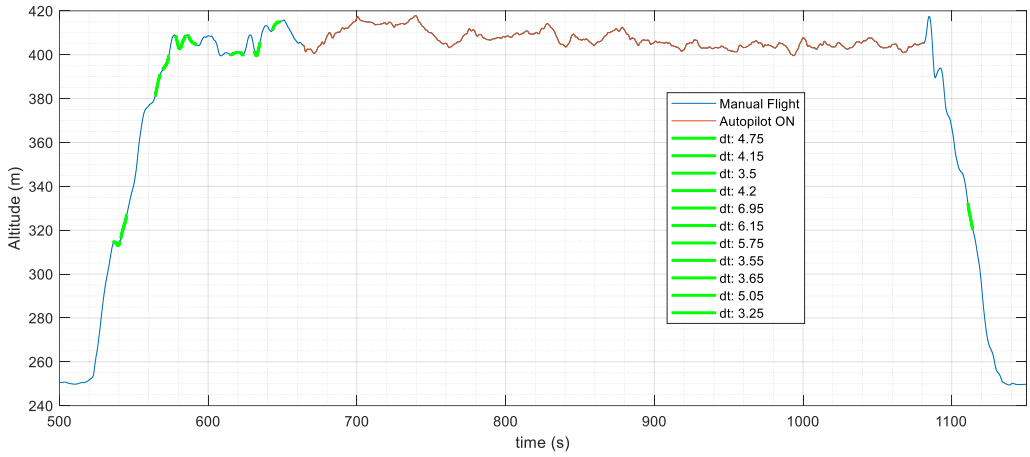

Figure 9-3: Altitude plot of Flight A. Green portions are the ones satisfying Criteria # 2 and used for stitching.

Table 9-1:Portions of Flight A satisfying Criteria #2 and used for stitching.

Part	**1**	**2**	**3**	**4**	**5**	**6**	**7**	**8**	**9**	**10**	**11**
Initial time, t_0	536.09	541.19	564.29	569.44	578.09	585.84	614.54	620.49	631.24	643.24	1110.84
Final time, t_f	540.84	545.34	567.79	573.64	585.04	591.99	620.29	624.04	634.89	648.29	1114.09
Duration, Δt	4.75	4.15	3.50	4.20	6.95	6.15	5.75	3.55	3.65	5.05	3.25

The previous table shows the start and end times for each of the portions selected for stitching. The duration of each portion is presented in the table as well as the legend of Figure

9-3. The following two figures show how the data looked like when stitched. Particularly the pitch and roll angles are presented. In these two figures, the pipe symbol "|" is used to mark where stitching happens. This marking method is used in other portions of the thesis to identify stitching locations.

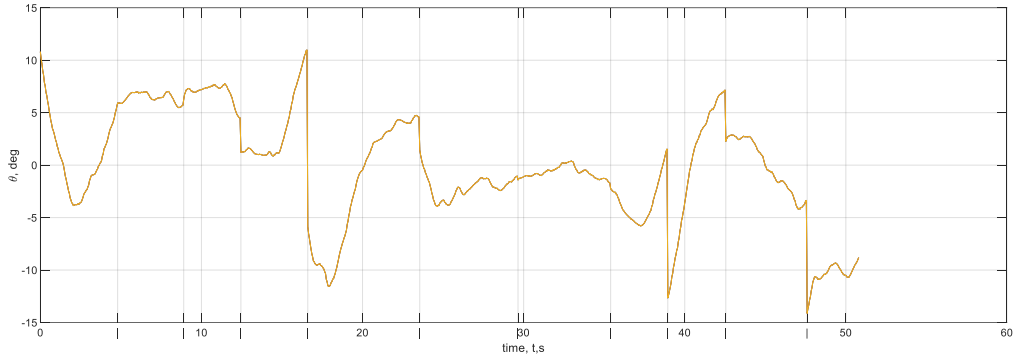

Figure 9-4: Plot of stitched flight portions obtained from Flight A. Plot shows pitch angle.

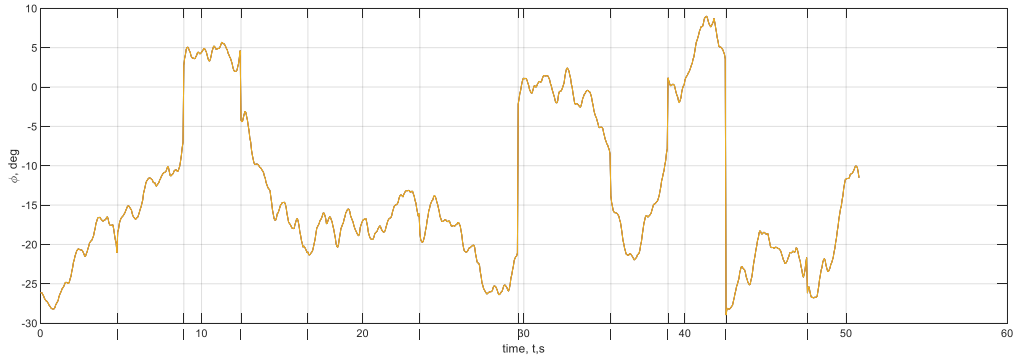

Figure 9-5: Plot of stitched flight portions obtained from Flight A. Plot shows roll angle.

9.3.2 Stitched data obtained from Flight B

The following figure shows the altitude plot of a SkyHunter 2 flight. This was a flight on April 26, 2018. This flight will be referred to as Flight B. In the figure, the green parts are the parts that were chosen for stitching. These were parts that matched set of criteria # 2 and were longer than 3 seconds. The following table shows the start and end times for each of the portions selected for stitching. The duration of each portion is presented in the table as well as the figure.

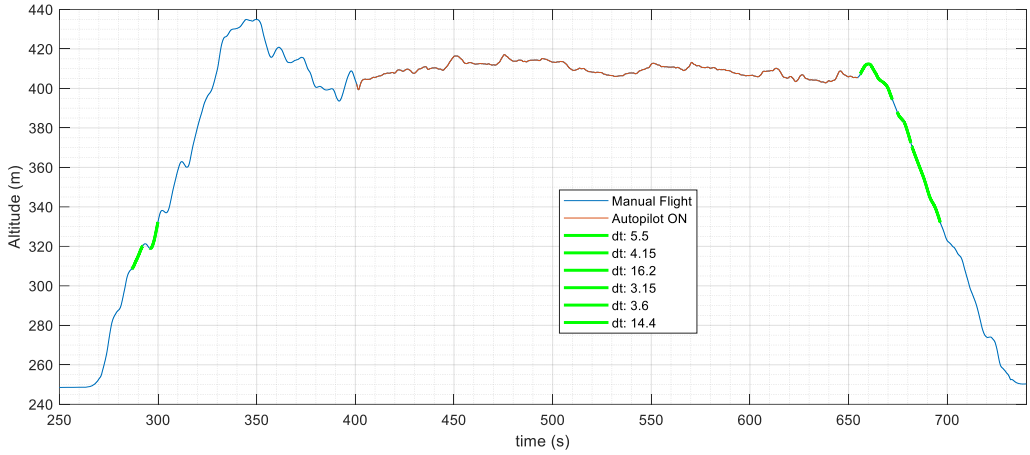

Figure 9-6: Altitude plot of Flight B. Green portions are the ones satisfying Criteria # 2 and used for stitching.

Table 9-2: Portions of Flight B satisfying Criteria #2 and used for stitching.

Part	**1**	**2**	**3**	**4**	**5**	**6**
Initial time, t_0	286.69	295.79	655.94	674.69	677.94	682.04
Final time, t_f	292.19	299.94	672.14	677.84	681.54	696.44
Duration, Δt	5.50	4.15	16.20	3.15	3.60	14.40

9.3.3 Stitched data obtained from Flight C

The following figure shows the altitude plot of another SkyHunter 2 flight. This was the second flight of the SkyHunter 2 on April 28, 2018. This flight will be referred to as Flight C. In the figure, the green parts are the parts that were chosen for stitching. These were parts that matched set of criteria # 2 and were longer than 3 seconds. The table following the figure shows the start and end times for each of the portions selected for stitching. The duration of each portion is presented in the table as well as the figure.

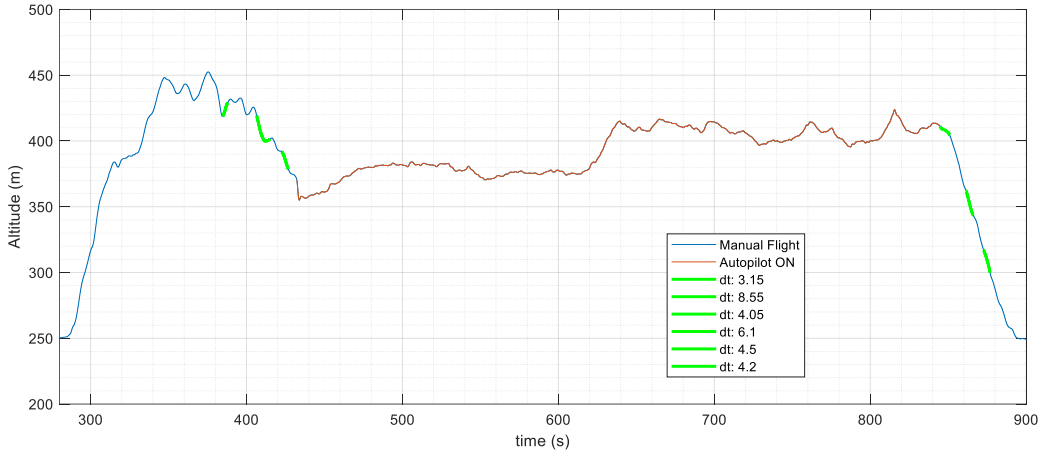

Figure 9-7: Altitude plot of Flight C. Green portions are the ones satisfying Criteria # 2 and used for stitching.

Table 9-3: Portions of Flight C satisfying Criteria #2 and used for stitching.

Part	**1**	**2**	**3**	**4**	**5**	**6**
Initial time, t_0	384.73	406.53	422.73	844.88	861.48	872.63
Final time, t_f	387.88	415.08	426.78	850.98	865.98	876.83
Duration, Δt	3.15	8.55	4.05	6.10	4.50	4.20

10 Adjusting the measurement noise covariance matrix

Some error was observed in the EKF state recreation in the initial system identification results for the SkyHunter. This can be seen in Section 6.1. Therefore, attention was given to adjusting the measurement noise covariance matrix. Tuning Extended Kalman Filters is important for obtaining meaningful and correct estimations. Tuning of Extended Kalman filters is commonly performed using trial-and-error as Reference [34] mentions.

Obtaining the process noise and measurement noise covariance matrices, Q and R, is part of that tuning. In this thesis, the process measurement noise was kept as it was obtained from Reference [8] and presented in Section 5.1.4. The measurement noise matrix was adjusted using trial-and-error as described below.

The process of adjusting the measurement noise matrix, R, started by using the measurement noise matrix used in the example of Reference [8]. Next, adjustments were made to the noise matrix one element at a time. After each adjustment, observation was made to see whether the change improved or worsened the EKF state propagation. When the EKF state propagation had a closer match to the measured states, this was regarded as an improvement in the EKF. When the EKF state propagation deviated more from the measured states, this was regarded as worsening of the EKF results.

Adjustments were made until the match between propagated states and measured states was very good. Knowing that accelerometers usually contain high noise, they were given a high noise variance in the matrix. The pitch rate derivative ($\dot{q}$) was also given a high noise variance since it is obtained by numerical differentiation of pitch rate measurements. Numerical differentiation would increase noise.

The following table shows the diagonal terms of the measurement noise matrix before adjustment and after adjustment. The measurement noise covariance matrix was defined to be a diagonal matrix as seen in Eq 10-1 below.

Table 10-1: Elements of measurement noise covariance before and after adjustment.

Term	**Corresponding Measurement**	**Original**	**Adjusted**
r_{11}	Airspeed, V	1.759E-02	1.759E-03
r_{22}	Angle of attack, α	9.902E-07	1.980E-07
r_{33}	Pitch angle, θ	1.977E-07	1.977E-08
r_{44}	Pitch rate, q	3.384E-07	3.384E-07
r_{55}	Time derivative of pitch rate, $\dot{q}$	3.168E-05	3.168E-01
r_{66}	Body x-axis acceleration, a_x	4.191E-04	4.191E-02
r_{77}	Body z-axis acceleration, a_z	2.020E-02	2.020E+00

$$R = \begin{bmatrix} r_{11} & 0 & 0 & 0 & 0 & 0 & 0 \\ 0 & r_{22} & 0 & 0 & 0 & 0 & 0 \\ 0 & 0 & r_{33} & 0 & 0 & 0 & 0 \\ 0 & 0 & 0 & r_{44} & 0 & 0 & 0 \\ 0 & 0 & 0 & 0 & r_{55} & 0 & 0 \\ 0 & 0 & 0 & 0 & 0 & r_{66} & 0 \\ 0 & 0 & 0 & 0 & 0 & 0 & r_{77} \end{bmatrix} \quad \text{Eq 10-1}$$

The following two sections show the improvement in state propagation obtained by adjusting the measurement noise matrix. The two sections are analyzing the same flight portion. The difference is that in Section 10.1, raw sensor data is given to the EKF. In Section, 10.2, the EKF is given data that was filtered to remove high frequency noise. It was observed that in both cases, the adjustments made to the measurement covariance matrix resulted in improved state propagation.

10.1EKF Results using adjusted measurement covariance. (Data not filtered)

The following table shows an example of how the state propagation results were before and after adjusting the measurement noise matrix. The EKF uses raw measurements (i.e. no filtering.) The improvement in match between propagated and measured states can be clearly seen.

Table 10-2: State propagation before and after adjusting the R matrix. Data not filtered.

State	Before adjusting measurement noise matrix, R	After adjusting measurement noise matrix, R
V	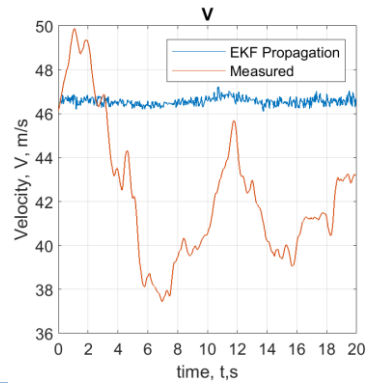	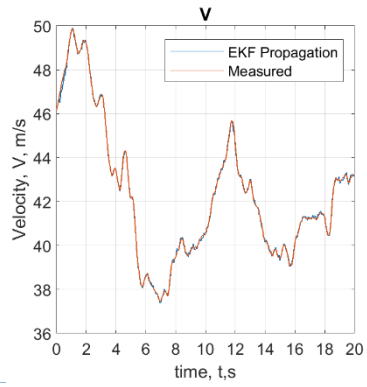
α	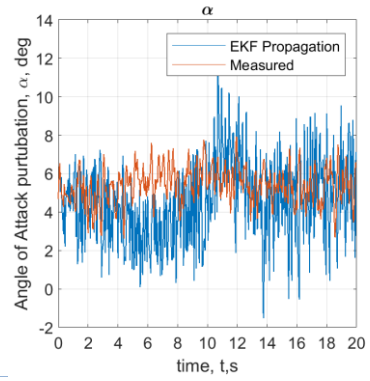	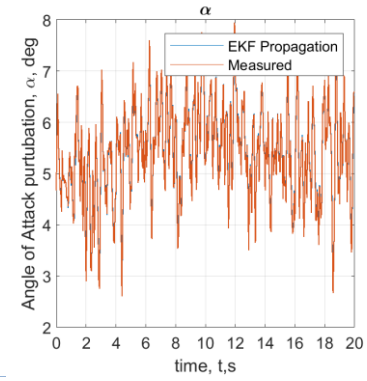
θ	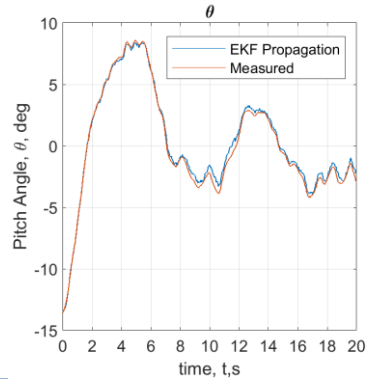	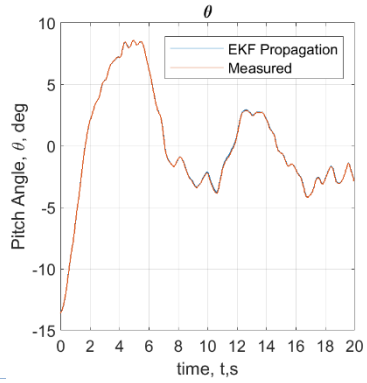
q	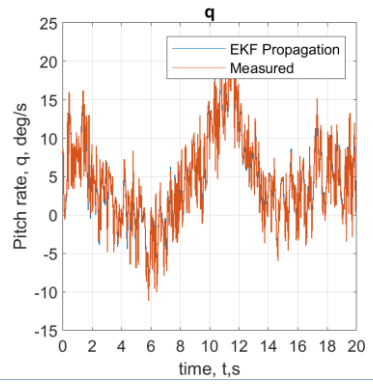	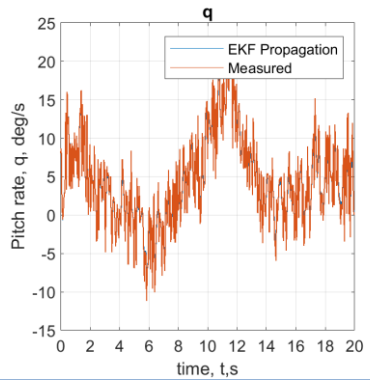

In the following table, the derivative estimates before and after adjustment are presented. The magnitude of several derivatives, $C_{D_0}, C_{D_V}, C_{L_0}, C_{L_V}, C_{m_0}, C_{m_V}$, became more reasonable after the adjustments. Some derivatives also got worse like C_{m_q} and $C_{m_{de}}$.

Table 10-3: Estimated derivatives before and after adjusting R. Data not filtered.

	AAA	EKF Before Adjusting R	EKF After Adjusting R
C_{D0}	0.0265	5.8332	-0.5446
C_{DV}	0.1139	-5.3345	0.4572
$C_{D\alpha}$	-0.346	1.5199	2.3224
C_{L0}	0.5046	72.9775	0.9829
C_{LV}	1.1735	-66.3542	-0.8642
$C_{L\alpha}$	5.8154	10.6520	9.6800
C_{m0}	0.0442	-51.8384	-3.7125
C_{mV}	0.0171	46.6911	1.5830
$C_{m\alpha}$	-0.9749	-4.1456	1.4927
C_{mq}	-15.233	-158.9880	-326.1934
C_{mde}	-1.0266	-6.3862	-14.7284

10.2 EKF Results using adjusted measurement covariance. (a_x, a_z, q Filtered)

The same comparison presented above is repeated here. This time some filtering is applied to remove high frequency noise from the data given to the EKF. Particularly, a_x, a_z and q are filtered using the Spencer 15 filter. It can be clearly seen that the adjusted measurement noise matrix resulted in improved state propagation.

Table 10-4: State propagation before and after adjusting the R matrix. a_x, a_z, q Filtered

State	Before adjusting measurement noise matrix, R	After adjusting measurement noise matrix, R
V	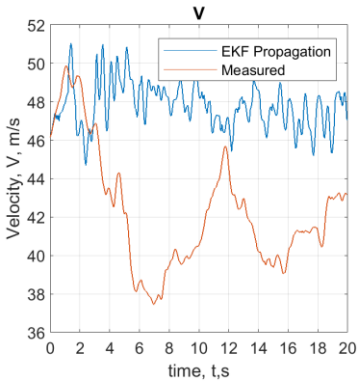	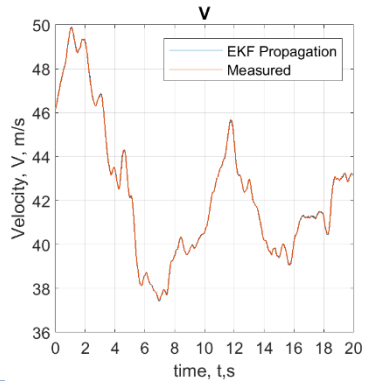
α	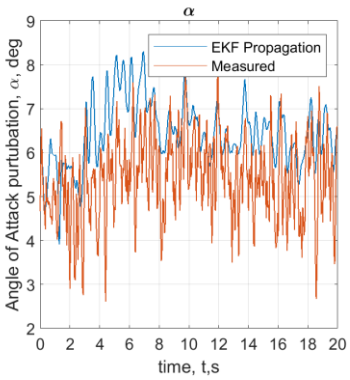	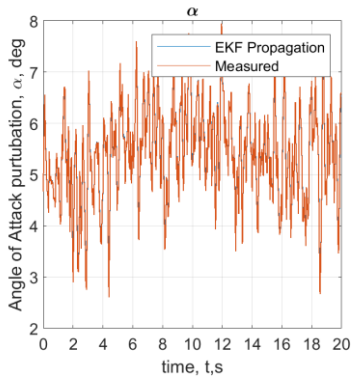
θ	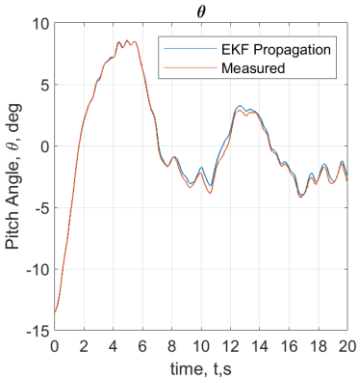	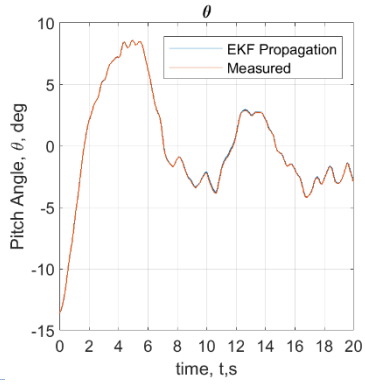
q	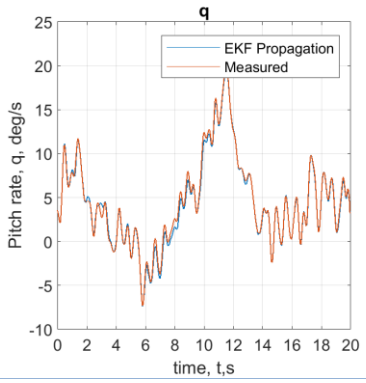	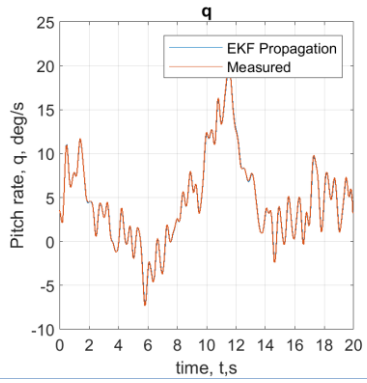

The following table shows the derivative estimates before and after adjusting R. The change in derivatives due to adjusting the R matrix is not as dramatic as in the previous section (when no data was filtered.) However, some derivatives that improved are: C_{L_0}, C_{L_V} and C_{L_α}.

Table 10-5: Estimated derivatives before and after adjusting R. a_x, a_z, q Filtered.

	AAA	EKF Before Adjusting R	EKF After Adjusting R
C_{D0}	0.0265	1.4416	-0.2309
C_{DV}	0.1139	-0.8512	0.3509
$C_{D\alpha}$	-0.346	-3.4250	0.1406
C_{L0}	0.5046	9.2235	1.2827
C_{LV}	1.1735	-6.8700	-0.7338
$C_{L\alpha}$	5.8154	-6.8264	5.5024
C_{m0}	0.0442	-1.5414	-0.1720
C_{mV}	0.0171	1.1201	0.0634
$C_{m\alpha}$	-0.9749	-1.0687	0.1774
C_{mq}	-15.233	-28.7661	-18.0905
C_{mde}	-1.0266	-2.9446	-0.7305

10.3 Summary

In summary, the measurement covariance matrix of the EKF, R, was adjusted in this Chapter. The state propagation of V, α, θ and q clearly improved after the adjustment. This is seen in that the EKF propagated states matched the measured states very closely when the R matrix was adjusted.

11 Improved SkyHunter System Identification Results

In this Chapter, the improved system identification results for the SkyHunter are presented. Initial system identification results and their short comings was discussed in Chapter 6. The steps taken to improve the results are summarized in Section 6.2 and detailed in Chapters 7 to 10.

The breakdown of this chapter is as follows:

1) First, Section 11.1 presents the way in which the results are interpreted and evaluated.
2) Section 11.2 presents system identification results based on flight portions matching set of criteria #1 (which was defined in Section 9.1.)
3) Section 11.3 presents system identification results based on flight portions matching set of criteria #2 (which was defined in Section 9.2.)
4) Section 11.4 presents system identification results based on stitched together flight portions (Stitching discussed in Section 9.3.)
5) Section 11.5 presents system identification results when two more derivatives (C_{L_q}&$C_{L_{de}}$) are estimated.
6) Section 11.6 makes overall observations from the previous results.
7) A summary is then provided in Section 11.7.

11.1Basis for evaluating system identification results

There are many results in this thesis. To evaluate these results,

1) Focus was placed on four derivatives out of the 11.
2) The obtained derivatives were compared to theoretical estimates from AAA.
3) The obtained derivatives were evaluated to see if they are in expected ranges.

The following subsections discuss these three points in more detail.

11.1.1 Focusing on four derivatives

In this thesis, 11 derivatives are being estimated. Comparing results obtained under different conditions for all 11 derivatives at once proved difficult. Therefore, attention was narrowed down to a fewer number of derivatives. This was done using the help of the following table. The table lists the relative importance of the different stability and control derivatives. It also lists the estimated accuracy of derivatives. This table was obtained from Reference [35].

Looking at the table, it can be seen that C_{L_α} has highest importance and estimated accuracy. C_{m_α} and C_{m_q} follow it in being less important and having lower estimated accuracy. Therefore, when evaluating the results in this thesis, highest attention was given to C_{L_α} results. After that, attention was given to C_{m_α}. Then, attention was given to C_{m_q} and $C_{m_{de}}$. Note: $C_{m_{de}}$ is not mentioned in the following table. However, attention was given to it more than the remaining derivatives.

Table 11-1: Relative importance and estimated accuracy of aircraft stability and control derivatives.[35]

Derivative	**Relative Importance[2]**	**Estimated Accuracy**
C_{L_α}	10	$\pm 5\%$
C_{m_α}	10	$\pm 10\%$
C_{m_q}	9	$\pm 20\%$
C_{m_u}	8	$\pm 20\%$
$C_{m_{\dot{\alpha}}}$	7	$\pm 40\%$
C_{D_u}	6	$\pm 20\%$
C_{D_α}	5	$\pm 10\%$
C_{L_u}	5	$\pm 20\%$
$C_{L_{\dot{\alpha}}}$	4	$\pm 40\%$
C_{L_q}	3	$\pm 20\%$
$C_{D_{\dot{\alpha}}}$	1	$\pm 50\%$
C_{D_q}	1	$\pm 30\%$

[2] The Importance Scale: 10=major, 5=minor, 0=negligible

Likewise, the previous table can be used to see the least important terms and the ones whose estimated accuracy is low. C_{L_u}, C_{D_α} and C_{D_u} are of low importance therefore not much attention was given to them.

Regarding $C_{m_{\dot{\alpha}}}$, despite its considerable importance, it is difficult to obtain this derivative using the EKF. To estimate these two derivatives special flight maneuvers would be needed. Reference [8] discusses this issue and mentions flight maneuvers and modification to the dynamic equations that can be made to estimate these derivatives.

11.1.2 Comparing the results to AAA theoretical models

The first way to evaluate the system identification results obtained from the EKF was to compare them to theoretical estimates from AAA. These estimates are presented in Section 3.3. Flight data from the SkyHunter were obtained from three different flights. All the flights were flown by SkyHunter 2. Thus, the dynamic models for SkyHunter 2 presented in Section 3.3 were the ones used as a base line for evaluating the EKF results. It is important to note that this comparison is a loose comparison. The dynamic models developed by AAA are not fault free. Theoretical estimation techniques such as those used by AAA are good for having an estimation, but they have errors which can even be large.

An important note needs to be made concerning the bias terms (i.e. C_{D_0}, C_{L_0} and C_{m_0}). These terms are not equivalent in meaning to those obtained from AAA. They are close in meaning but not the same. For example, C_{D_0} from AAA would be the value of C_D when the aircraft is flying in the trim condition defined in AAA (presented in Chapter 3). On the other hand, C_{D_0} obtained from the EKF is the linear extrapolation from the average α and V of the trim maneuver to the zero α and V point. [12] Therefore, minimal attention will be given to comparing the EKF results for C_{D_0}, C_{L_0} and C_{m_0} to the AAA estimates.

11.1.3 Comparing EKF results to expected ranges for them.

In addition to comparing EKF results to AAA estimates, the results were also evaluated to see if they lie in expected ranges. The following table shows what are the expected ranges for different stability and control derivatives. The information in this table is obtained from Chapter 3 of Reference [3].

It is important to note that the derivatives obtain from Reference [3] are not exactly equivalent in meaning to those being obtained from the EKF. One of the reasons for this was discussed in the previous section when talking about the bias terms. Another reason is that: the EKF uses simplified equations of motion as presented in Chapter 2 and Section 5.1. The equations assume we have only a limited number of derivatives (11 derivatives). Reference [3] is uses slightly different theory. It also uses models with more stability and control derivatives. Therefore, when the EKF estimates a certain derivative, it can be a combination of more than one derivative from the reference. For example, the EKF estimates C_{m_q} without estimating $C_{m_{\dot{\alpha}}}$.that may cause the estimate for C_{m_q} from the EKF to have some component of $C_{m_{\dot{\alpha}}}$ in it. However, despite knowing that, Table 11-2 was used to have some loose idea of what the expected ranges for the derivatives are.

Table 11-2: Expected ranges for stability and control derivatives. Ref.[3]

	Min	Max	Units
C_D	0.01	0.15	-
C_{D_a}	0	2	rad^{-1}
C_{D_u}	-0.01	0.3	-
C_{L_0}	-0.05	0.4	-
C_{L_a}	1	8	rad^{-1}
$C_{L_{ih}}$	0	1.2	rad^{-1}
$C_{L_{de}}$	0	0.6	rad^{-1}
C_{L_u}	-0.2	0.6	-
$C_{L_{\dot{\alpha}}}$	-5	15	rad^{-1}
C_{L_q}	0	30	rad^{-1}
C_{m_0}	0.15	-0.15	-
C_{m_α}	-4	1	rad^{-1}
$C_{m_{ih}}$	0	-8	rad^{-1}
$C_{m_{de}}$	0	-4	rad^{-1}
C_{m_u}	-0.4	0.6	-
$C_{m_{\dot{\alpha}}}$	0	-20	rad^{-1}
C_{m_q}	0	-90	rad^{-1}

11.2System identificaiton of portions matching set of criteria #1

All results in this section are based on flight data matching set of criteria #1 (presented in Section 9.1). First, Section 11.2.1 shows results from a single flight portion but: a) using several data filtering techniques and b) using several methods for estimating the aircraft angle of attack during flight. Then, Section 11.2.2 shows results from several flight portions and they are compared to see if they are consistent with each other.

11.2.1 Results from one flight portion with several modifications

A portion of flight from April 26th, 2018 Flight 1 for SkyHunter 2 was found to satisfy Criteria 1. The flight portion spanned from $t_0 = 676.6\ s$ to $t_f = 700\ s$. This section presents system identification results for that portion. In the results, several comparisons were made. The EKF was run under several modifications. This is why there are many results in this section

instead of just one set of stability and control derivatives. Comparing these results was desired to see which modification yields more acceptable results.

The explored modifications are

1) **Exploring which data is filtered to remove noise.** In one case, only the rotation rates and the linear accelerations were filtered. [Results from that case are presented in Table 11-4] In another case the rotation rates, the linear accelerations and the angle of attack were filtered. [Results from that case are presented in Table 11-5]
2) **Exploring which filter, of the filters presented in Chapter 7, is used.** Four different options were explored: no filtering, moving average filter, spencer filter and low pass filter.
3) **Exploring the effect of different angle of attack estimation.** Again, the SkyHunter does not have an airflow sensor to measure the angle of attack. Instead, as mentioned in Chapter 8, the angle of attack is estimated using an EKF. System identification results are presented for different versions of that $\alpha\beta$-EKF in the rows of Table 11-4 and Table 11-5.

Regarding the third point… As mentioned in Chapter 8, the $\alpha\beta$-EKF depends on an analytical dynamic model to estimate the current angle of attack of the SkyHunter. That analytical model has a specified trim angle of attack value and a specified trim elevator angle value. If these values change the estimated angle of attack during flight can be shifted higher or lower. Thus, different angle of attack flight data would be obtained depending on what trim values are used in the $\alpha\beta$-EKF. In the following system identification results, the $\alpha\beta$-EKF was set to have different trim angles of attack and elevator angles. Four different sets of trim values are used. The following table lists the different trim values. For the trim elevator angle in sets 2

to 4, a moving average filter is used to update the trim elevator angle depending on the commanded elevator angle during flight. This was discussed in Chapter 8.

Table 11-3: Four different trim values used to run the $\alpha\beta$-EKF

	α_{trim}	de_{trim}
First set	5.76°	−9.14°
Second set	5.76°	Moving average of commanded trim
Third set	6.38°	Moving average of commanded trim
Fourth set	7.00°	Moving average of commanded trim

With enough background information, the system identification results are now presented. Table 11-4 shows results where only a_x, a_z and q are filtered. Table 11-5, shows results where a_z, a_z, q and α are filtered. The rows of these tables show results based on different α_{trim} and de_{trim} values provided to the $\alpha\beta$-EKF. Results from different filters (No filter, moving average 21-point, Spencer 15-point and low pass) are presented in the different columns of the tables.

Table 11-4: Comparison of system identification results based on different α estimation and different filtering methods. Filters only applied to a_x, a_z, q.

$\alpha\beta$-EKF Version		System Identification Results (Only rotation rates and accelerations filtered)				
α_{trim}	de_{trim}					
5.76°	$-9.14°$		From AAA	NoFilter	MovAv21	Spenc15	LowPass
		CD0	0.0265	0.2934	0.2204	0.3599	0.3716
		CDV	0.1139	-0.0994	-0.0708	-0.1382	-0.1509
		CDa	-0.3460	0.5725	1.0924	0.2588	0.2143
		CL0	0.5046	1.7662	2.0248	2.3968	2.4151
		CLV	1.1735	-1.0266	-1.2687	-1.4093	-1.4324
		CLa	5.8154	4.5490	4.4889	1.8822	1.7600
		Cm0	0.0442	-3.9519	-0.0719	-0.2253	-0.2714
		CmV	0.0171	1.2440	0.0239	0.1015	0.1281
		Cma	-0.9749	-0.9212	0.0119	-0.3936	-0.4462
		Cmq	-15.2330	-335.6803	-8.3000	-15.5959	-18.2032
		Cmde	-1.0266	-18.2408	-0.3474	-1.0780	-1.2380
5.76°	Moving average of commanded trim		From AAA	NoFilter	MovAv21	Spenc15	LowPass
		CD0	0.0265	0.2922	0.2261	0.3534	0.3647
		CDV	0.1139	-0.0935	-0.0754	-0.1233	-0.1350
		CDa	-0.3460	0.5529	1.0816	0.2136	0.1658
		CL0	0.5046	2.0087	2.1919	2.4961	2.5101
		CLV	1.1735	-1.2354	-1.4244	-1.4881	-1.5059
		CLa	5.8154	3.9618	4.1234	1.5583	1.4349
		Cm0	0.0442	-3.9447	-0.0716	-0.2165	-0.2623
		CmV	0.0171	1.2649	0.0237	0.1073	0.1353
		Cma	-0.9749	-0.8759	0.0102	-0.3778	-0.4248
		Cmq	-15.2330	-336.2908	-8.2996	-15.5368	-18.1452
		Cmde	-1.0266	-18.0636	-0.3470	-0.9859	-1.1336
6.38°	Moving average of commanded trim		From AAA	NoFilter	MovAv21	Spenc15	LowPass
		CD0	0.0265	0.3060	0.2383	0.3793	0.3913
		CDV	0.1139	-0.1052	-0.0894	-0.1388	-0.1507
		CDa	-0.3460	0.5936	1.1063	0.2101	0.1600
		CL0	0.5046	1.9686	2.1453	2.4737	2.4889
		CLV	1.1735	-1.2393	-1.4220	-1.4829	-1.5007
		CLa	5.8154	3.9497	4.0928	1.5363	1.4128
		Cm0	0.0442	-3.9485	-0.0716	-0.2122	-0.2577
		CmV	0.0171	1.2648	0.0238	0.1071	0.1351
		Cma	-0.9749	-0.8864	0.0099	-0.3775	-0.4245
		Cmq	-15.2330	-338.5013	-8.2889	-15.5395	-18.1388
		Cmde	-1.0266	-18.1596	-0.3465	-0.9860	-1.1339
7.00°	Moving average of commanded trim		From AAA	NoFilter	MovAv21	Spenc15	LowPass
		CD0	0.0265	0.3187	0.2500	0.4053	0.4181
		CDV	0.1139	-0.1165	-0.1034	-0.1540	-0.1662
		CDa	-0.3460	0.6330	1.1291	0.2052	0.1529
		CL0	0.5046	1.9275	2.0991	2.4514	2.4679
		CLV	1.1735	-1.2421	-1.4192	-1.4774	-1.4950
		CLa	5.8154	3.9387	4.0595	1.5119	1.3884
		Cm0	0.0442	-3.9638	-0.0717	-0.2079	-0.2531
		CmV	0.0171	1.2658	0.0239	0.1068	0.1350
		Cma	-0.9749	-0.9028	0.0096	-0.3773	-0.4242
		Cmq	-15.2330	-342.0870	-8.2776	-15.5435	-18.1348
		Cmde	-1.0266	-18.3295	-0.3460	-0.9861	-1.1343

Table 11-5: Comparison of system identification results based on different α estimation and different filtering methods. Filters only applied to a_x, a_z, q, α.

$\alpha\beta$-EKF Version		System Identification Results (Rotation rates, accelerations & angle of attack filtered)					
α_{trim}	de_{trim}		From AAA	NoFilter	MovAv21	Spenc15	LowPass
5.76°	−9.14°	CD0	0.0265	0.2934	0.5713	0.4659	0.4026
		CDV	0.1139	-0.0994	-0.2676	-0.1894	-0.1518
		CDa	-0.3460	0.5725	-0.6716	-0.3666	-0.1591
		CL0	0.5046	1.7662	3.9571	3.3594	3.0978
		CLV	1.1735	-1.0266	-2.3583	-1.8887	-1.7275
		CLa	5.8154	4.5490	-4.9548	-3.5382	-2.6136
		Cm0	0.0442	-3.9519	-0.0531	-0.2316	-0.2797
		CmV	0.0171	1.2440	0.0077	0.0987	0.1230
		Cma	-0.9749	-0.9212	-0.2519	-0.4533	-0.4663
		Cmq	-15.2330	-335.6803	-6.8051	-16.5445	-19.3711
		Cmde	-1.0266	-18.2408	-0.4796	-1.1703	-1.3268
5.76°	Moving average of commanded trim		From AAA	NoFilter	MovAv21	Spenc15	LowPass
		CD0	0.0265	0.2922	0.5900	0.4561	0.3927
		CDV	0.1139	-0.0935	-0.2471	-0.1628	-0.1290
		CDa	-0.3460	0.5529	-0.9958	-0.4681	-0.2345
		CL0	0.5046	2.0087	4.0742	3.3601	3.1006
		CLV	1.1735	-1.2354	-2.3158	-1.8350	-1.6928
		CLa	5.8154	3.9618	-6.3962	-3.9370	-2.8922
		Cm0	0.0442	-3.9447	-0.0498	-0.2215	-0.2702
		CmV	0.0171	1.2649	0.0130	0.1058	0.1304
		Cma	-0.9749	-0.8759	-0.2224	-0.4288	-0.4440
		Cmq	-15.2330	-336.2908	-6.8930	-16.5188	-19.3874
		Cmde	-1.0266	-18.0636	-0.4143	-1.0583	-1.2190
6.38°	Moving average of commanded trim		From AAA	NoFilter	MovAv21	Spenc15	LowPass
		CD0	0.0265	0.3060	0.6470	0.4987	0.4281
		CDV	0.1139	-0.1052	-0.2722	-0.1820	-0.1456
		CDa	-0.3460	0.5936	-1.0791	-0.5249	-0.2781
		CL0	0.5046	1.9686	4.1281	3.3988	3.1259
		CLV	1.1735	-1.2393	-2.3098	-1.8348	-1.6914
		CLa	5.8154	3.9497	-6.3365	-3.9300	-2.8833
		Cm0	0.0442	-3.9485	-0.0473	-0.2172	-0.2659
		CmV	0.0171	1.2648	0.0129	0.1060	0.1306
		Cma	-0.9749	-0.8864	-0.2230	-0.4292	-0.4449
		Cmq	-15.2330	-338.5013	-6.8855	-16.5070	-19.3952
		Cmde	-1.0266	-18.1596	-0.4143	-1.0595	-1.2209
7.00°	Moving average of commanded trim		From AAA	NoFilter	MovAv21	Spenc15	LowPass
		CD0	0.0265	0.3187	0.7057	0.5426	0.4645
		CDV	0.1139	-0.1165	-0.2972	-0.2013	-0.1622
		CDa	-0.3460	0.6330	-1.1633	-0.5825	-0.3225
		CL0	0.5046	1.9275	4.1805	3.4364	3.1499
		CLV	1.1735	-1.2421	-2.3035	-1.8336	-1.6886
		CLa	5.8154	3.9387	-6.2779	-3.9258	-2.8776
		Cm0	0.0442	-3.9638	-0.0447	-0.2128	-0.2616
		CmV	0.0171	1.2658	0.0129	0.1062	0.1307
		Cma	-0.9749	-0.9028	-0.2235	-0.4296	-0.4458
		Cmq	-15.2330	-342.0870	-6.8778	-16.4957	-19.4031
		Cmde	-1.0266	-18.3295	-0.4142	-1.0605	-1.2226

Looking at Table 11-4 and focusing on C_{L_α}, it can be seen that:

1) The EKF with unfiltered measurements yielded C_{L_α} of 3.96 to 4.55 depending on the used angle of attack estimation. The EKF with data filtered using 21-point moving average yielded C_{L_α} between 4 and 4.5. The EKF using Spencer 15 filter and Low pass filter yielded lower C_{L_α} ranging between 1.5 to 1.9 and 1.4 to 1.8 respectively. The moving average filter has the closest value to AAA. (Note: this observation is true for the analyzed flight portion. It is not the general case for other flight portions.)
    a. Note: Although the "no filter" C_{L_α} results in the table are reasonable, they are not regarded when evaluating what value is closest to AAA. This is because results obtained without filtering were found to be inconsistent if different flight portions are analyzed. The EKF even failed sometimes when the data was not filtered.
2) Different angle of attack estimations did not result in much change in the estimated derivatives. The range of change in C_{L_α} mentioned in point (1) is not large.
3) There is a close match between results obtained using the Spencer filter and the low pass filter. This close match was observed repeatedly for different flight portions (as will be seen in the following sections). The close match is reasonable since both filters had a similar filtering effect when observing the power spectra presented in Section 7.3.
4) A close match between C_{L_α} results from no filtering and from the moving average filter is observed in the previous table. However, this is true for this table not for all results in this thesis presented in the following sections.

Looking at C_{m_α}, it can be seen that:

1) The moving average filter was resulting in a small positive C_{m_α}. This would indicate that the SkyHunter is unstable, which is not expected.

2) The Spencer and low pass filters had negative C_{m_α} on the other hand ranging between -0.377 to -0.393 and -0.424 to -0.446, respectively. The low pass filter therefore was closest to AAA.
3) Again, different angle of attack estimations did not result in much change in the estimation of C_{m_α}.

Looking at C_{m_q}, it can be seen that:

1) The unfiltered results yield a very large negative value which is not reasonable.
2) The filtered results yield more reasonable values. Comparing to AAA, the Spencer filter and the low pass filter have the closest values to AAA.
3) Different angle of attack estimations did not result in much change in the estimation of C_{m_q}.

Looking at $C_{m_{de}}$:

1) It has a value of -18 in the unfiltered case, which is too large in magnitude to be correct.
2) The filtered data produced better estimation. The estimates of the Spencer and low pass filters are closer to AAA than the estimate obtained using moving average filtering.
3) Different angle of attack estimations did not result in much change in the estimation of $C_{m_{de}}$.

Looking at Table 11-4:

To make a brief summary, there are 11 terms being estimated. Three of them we do not need to care about comparing to AAA values. These are the bias terms ($C_{D_0}, C_{L_0}, C_{m_0}$). The moving average filter has values closer to AAA for C_{L_α} and C_{m_V}. The spencer filter and the low pass filter both have similar estimates for all derivatives. They also have estimates closer to AAA for C_{m_α}, C_{m_q} & $C_{m_{de}}$. The remaining three terms (C_{D_V}, C_{D_α} & C_{L_V}) are not close to AAA. It was

observed that different angle of attack estimations did not results in much change in the estimation.

Looking at Table 11-5:

This is the table where α measurements were filtered too instead of just filtering a_x, a_z & q measurements. It can be summarized that comparing to results in Table 11-4:

1) A major decrease in the estimation was observed in C_{L_α} becoming negative when α was filtered.
2) Some derivatives went farther than AAA (C_{D_V}, C_{L_V}) when α was filtered.
3) Some derivatives went closer to AAA ($C_{D_\alpha}, C_{m_\alpha}$) when α was filtered.
4) Some derivatives were in a similar position compared to AAA ($C_{m_V}, C_{m_q}, C_{m_{de}}$). when α was filtered.

It will be clearer in the following sections that results obtained without filtering α were preferred. Here, this is supported by point 1 in the previous list.

11.2.2 Consistency evaluation for several flight portions complying to set of criteria # 1

The results obtained in the previous section are just from one flight portion. To evaluate the performance of the system identification EKF, several flight portions were used to obtain system identification results. These results were then compared to see if the derivatives consistently have the same values (or are in a similar range). The following tables shows system identification results obtained from 11 flight portions that comply to set of criteria #1. The different tables show the system identification results obtained when the measured accelerations and rotation rates were filtered before they were used in the EKF. The used filters are the low pass, Spencer 15-point and moving average 21-point filters presented in Section 7.2.

The second column in all the tables presents the derivative estimates obtained from AAA. They serve as loose baseline for evaluating the EKF estimates. The following 5 columns show results from flight portions obtained from a flight performed on April 26, 2018 (Flight B in Section 9.3.2). The next 6 columns show results from a different flight that took place on April 28, 2018 (Flight A in Section 9.3.1). The last three columns show the minimum, maximum and median of the estimates obtained from the 11 flight portions.

In the tables t0, tf and dt are the initial time, final time and duration of the flight portion being analyzed. The column heading indicates the month and day of the flight, the aircraft name and the flight number on that day. The format is Month_Day_Aircraft_FlightNumber.

Table 11-6: Results from portions matching criteria # 1. Low pass filtering applied to a_x, a_z & q.

	From AAA	04_26_Sky2_F1	04_26_Sky2_F1	04_26_Sky2_F1	04_26_Sky2_F1	04_26_Sky2_F1	04_28_Sky2_F1	04_28_Sky2_F1	04_28_Sky2_F1	04_28_Sky2_F1	04_28_Sky2_F1	Minimum	Maximum	Median
t0	NaN	657.6000	677	676.6000	677	685.8000	538.8000	562.8000	578.7000	606.8000	651	1095	NaN	NaN	NaN
tf	NaN	669.1000	705	700	700	700	548.2000	573.8000	589.5000	626.6000	664.4000	1106	NaN	NaN	NaN
Dt	NaN	11.5000	28	23.4000	23	14.2000	9.4000	11	10.8000	19.8000	13.4000	11	NaN	NaN	NaN
CD0	0.0265	-0.0614	0.4351	0.3913	0.4205	0.0838	-0.6707	-0.4372	-0.2400	0.1626	0.2791	0.2797	-0.6707	0.4351	0.1626
CDV	0.1139	0.2584	-0.1929	-0.1507	-0.1704	0.0525	0.5526	0.4539	0.3654	0.0221	-0.0733	-0.1033	-0.1929	0.5526	0.0221
CDa	-0.3460	-0.1252	0.1447	0.1600	0.0675	1.2260	1.6346	0.4963	0.1150	-0.5004	-0.6088	0.7805	-0.6088	1.6346	0.1447
CL0	0.5046	2.3623	2.6328	2.4889	2.7151	1.0206	0.5733	0.7450	0.9821	0.9911	2.0371	1.0460	0.5733	2.7151	1.0460
CLV	1.1735	-1.2417	-1.5707	-1.5007	-1.6248	-0.4282	-0.5819	-0.1887	-0.2902	-0.3960	-1.3330	-0.6877	-1.6248	-0.1887	-0.6877
CLa	5.8154	-0.4654	0.7883	1.4128	0.4849	5.7895	9.6575	3.9459	4.1127	3.8591	2.4127	5.3657	-0.4654	9.6575	3.8591
Cm0	0.0442	-0.5739	-0.1595	-0.2577	-0.2209	-0.2029	-0.0671	-0.0237	-0.2505	-0.1815	-0.1498	-0.0835	-0.5739	-0.0237	-0.1815
CmV	0.0171	0.1699	0.0390	0.1351	0.0905	0.0720	0.0054	-0.0985	0.0536	0.0987	0.0508	0.0319	-0.0985	0.1699	0.0536
Cma	-0.9749	0.3667	-0.4471	-0.4245	-0.4493	-0.1857	0.0985	-0.2967	-0.1787	-0.0558	-0.6213	-0.1279	-0.6213	0.3667	-0.1857
Cmq	-15.2330	-29.6904	-18.3168	-18.1388	-19.2735	-12.4703	-17.6604	-11.8867	-21.5731	-17.8085	20.1084	-16.2317	-29.6904	20.1084	-17.80...
Cmde	-1.0266	-2.4973	-1.1264	-1.1339	-1.1961	-1.0012	-0.4864	-1.1291	-1.5642	-0.7057	-1.1904	-0.5787	-2.4973	-0.4864	-1.1291

The previous table uses the low pass filter mentioned in Chapter 7 to filter a_x, a_z & q. Looking at the estimates in the previous table, it can be seen that:

1) there is a wide variation in the results. For example, the estimated C_{L_α} ranges from -0.47 to 9.7. This shows that there is a lack of consistency in the EKF estimation. The results are spread over a wide range.
2) The same can be said about the other derivatives too.
3) However, some weak consistency can be observed between derivatives from the same flight. This can be seen in:

a) Columns 4, 5 & 6 all having C_{L_α} around 1. (They are from the same flight and use common flight region)

b) Columns 9, 10 & 11 all having C_{L_α} close to 4. (They are from same flight and do not use common flight regions)

c) The consistency is weak, and it breaks down. This can be seen, for example in C_{L_α} of column 7. It is about 5.8 although it is from the same flight as columns 4, 5 & 6.

d) Similar comments can be made about C_{m_α}

4) The $C_{m_{de}}$ derivative shows a degree of consistency even between flights. The derivative repeatedly has values in the range [-0.5 to -1.6].

The following table uses the 15-point Spencer filter mentioned in Chapter 7 to filter a_x, a_z & q. Similar observation can be made in it as those made for the low pass filter results.

Table 11-7: Results from portions matching criteria # 1. 15-point Spencer filtering applied to a_x, a_z & q.

	From AAA	04_26_Sky2_F1	04_26_Sky2_F1	04_26_Sky2_F1	04_26_Sky2_F1	04_26_Sky2_F1	04_28_Sky2_F1	04_28_Sky2_F1	04_28_Sky2_F1	04_28_Sky2_F1	04_28_Sky2_F1	04_28_Sky2_F1	Minimum	Maximum	Median
t0	NaN	657.6000	677	676.6000	677	685.8000	538.8000	562.8000	578.7000	606.8000	651	1095	NaN	NaN	NaN
tf	NaN	669.1000	705	700	700	700	548.2000	573.8000	589.5000	626.6000	664.4000	1106	NaN	NaN	NaN
Dt	NaN	11.5000	28	23.4000	23	14.2000	9.4000	11	10.8000	19.8000	13.4000	11	NaN	NaN	NaN
CD0	0.0265	-0.0784	0.4185	0.3793	0.4017	0.0906	-0.6932	-0.4629	-0.2957	0.1386	0.2045	0.2837	-0.6932	0.4185	0.1386
CDV	0.1139	0.2598	-0.1807	-0.1388	-0.1563	0.0525	0.5716	0.4648	0.3906	0.0431	-0.0230	-0.1052	-0.1807	0.5716	0.0431
CDa	-0.3460	0.0460	0.2367	0.2101	0.1618	1.2092	1.6690	0.6715	0.4592	-0.4474	-0.3540	0.8247	-0.4474	1.6690	0.2367
CL0	0.5046	2.1237	2.5711	2.4737	2.6531	1.0056	0.5382	0.6905	0.8984	0.9556	1.8827	1.0274	0.5382	2.6531	1.0274
CLV	1.1735	-1.1872	-1.5316	-1.4829	-1.5879	-0.4059	-0.5221	-0.1337	-0.2303	-0.3586	-1.2242	-0.6759	-1.5879	-0.1337	-0.6759
CLa	5.8154	1.5113	1.1458	1.5363	0.8652	5.8750	9.5400	4.1215	4.5548	3.9982	2.9659	5.5923	0.8652	9.5400	3.9982
Cm0	0.0442	-0.4934	-0.1273	-0.2122	-0.1851	-0.1626	-0.0262	-0.0369	-0.2125	-0.1185	-0.1215	-0.0482	-0.4934	-0.0262	-0.1273
CmV	0.0171	0.1470	0.0279	0.1071	0.0769	0.0621	-0.0151	-0.0627	0.0373	0.0607	0.0317	0.0147	-0.0627	0.1470	0.0373
Cma	-0.9749	0.1904	-0.3985	-0.3775	-0.4014	-0.1448	0.0441	-0.2307	-0.1858	-0.0774	-0.4657	-0.1136	-0.4657	0.1904	-0.1858
Cmq	-15.2330	-24.5453	-15.1881	-15.5395	-16.2424	-9.9215	-13.3364	-11.0422	-18.3819	-12.6259	20.6756	-11.2477	-24.5453	20.6756	-13.33...
Cmde	-1.0266	-2.2330	-0.9553	-0.9860	-1.0185	-0.7794	-0.3652	-0.9305	-1.4120	-0.5344	-1.0084	-0.4004	-2.2330	-0.3652	-0.9553

Table 11-8: Results from portions matching criteria # 1. 21-point moving average filtering applied to a_x, a_z & q.

	From AAA	04_26_Sky2_F1	04_26_Sky2_F1	04_26_Sky2_F1	04_26_Sky2_F1	04_26_Sky2_F1	04_28_Sky2_F1	04_28_Sky2_F1	04_28_Sky2_F1	04_28_Sky2_F1	04_28_Sky2_F1	04_28_Sky2_F1	Minimum	Maximum	Median
t0	NaN	657.6000	677	676.6000	677	685.8000	538.8000	562.8000	578.7000	606.8000	651	1095	NaN	NaN	NaN
tf	NaN	669.1000	705	700	700	700	548.2000	573.8000	589.5000	626.6000	664.4000	1106	NaN	NaN	NaN
Dt	NaN	11.5000	28	23.4000	23	14.2000	9.4000	11	10.8000	19.8000	13.4000	11	NaN	NaN	NaN
CD0	0.0265	-0.0981	0.2783	0.2383	0.2636	0.1136	-0.6159	-0.5011	-0.4187	-0.0886	-0.0669	0.2892	-0.6159	0.2892	-0.0669
CDV	0.1139	0.2062	-0.1315	-0.0894	-0.1133	0.0170	0.4927	0.4691	0.4233	0.1778	0.1158	-0.1162	-0.1315	0.4927	0.1158
CDa	-0.3460	0.7671	1.1273	1.1063	1.0891	1.3234	1.7012	1.0808	1.4451	0.5058	0.9401	0.8827	0.5058	1.7012	1.0891
CL0	0.5046	1.5014	2.1831	2.1453	2.2502	1.0051	0.4055	0.6858	0.6102	0.4412	0.9222	1.1399	0.4055	2.2502	1.0051
CLV	1.1735	-1.0126	-1.4404	-1.4220	-1.4991	-0.5152	-0.3715	-0.1698	-0.1378	-0.0114	-0.5266	-0.8099	-1.4991	-0.0114	-0.5266
CLa	5.8154	5.9667	3.9897	4.0928	3.8553	6.9052	9.3196	4.6031	6.6533	5.7298	5.4474	5.8697	3.8553	9.3196	5.7298
Cm0	0.0442	-0.0553	-0.0322	-0.0716	-0.0635	-0.0168	0.0095	0.0585	0.0495	0.0231	-0.0263	0.0514	-0.0716	0.0585	-0.0168
CmV	0.0171	0.0342	0.0015	0.0238	0.0236	0.0132	-0.0116	-0.0496	-0.0616	-0.0221	0.0494	-0.0290	-0.0616	0.0494	0.0015
Cma	-0.9749	0.0495	0.0020	0.0099	0.0027	-0.0219	0.0533	0.0723	0.0254	0.0161	-0.0376	-0.0721	-0.0721	0.0723	0.0099
Cmq	-15.2330	-10.9840	-5.9775	-8.2889	-7.6660	-3.1604	-5.9042	0.9790	3.1297	-1.6586	-1.5974	4.1600	-10.9840	4.1600	-3.1604
Cmde	-1.0266	-0.1938	-0.2395	-0.3465	-0.3004	-0.0777	-0.0650	0.0456	-0.1048	-0.0280	0.1006	0.1500	-0.3465	0.1500	-0.0777

The previous table uses the 21-point moving average filter mentioned in Chapter 7 to filter a_x, a_z & q. Looking at the table it can be observed that:

1) Again, there is a spread in the derivative estimates. However, the spread is less than the low pass and Spencer filters. (I.e. there is a higher level of consistency between flight)
2) Many of the C_{L_α} estimates are in a range that is comparable to the AAA estimate (4 to 7).
3) C_{m_α} is mostly a positive estimate which would indicate an unstable aircraft. This is not expected.
4) C_{m_q} is smaller than it is expected to be and sometimes has unexpected sign (i.e. is positive)
5) The $C_{m_{de}}$ estimation is not widely spread. However, the estimate swings between being positive and negative. A positive $C_{m_{de}}$ would not be correct.

In general, the moving average filter had less spread in estimation (i.e. higher consistency). For C_{L_α} it was close to the AAA estimate. However, results for C_{m_q}, C_{m_α} and $C_{m_{de}}$ may be incorrectly falsified due to the use of the filter since they are smaller than expected/ have improper signs. Section 7.2 showed that the moving average filter changes the magnitude of low frequencies. Thus, the moving average filter may be falsifying the aircraft dynamics we are trying to identify.

Table 11-9: Results from portions matching criteria # 1. No filtering applied.

	From AAA	04_26_Sky2_F1	04_26_Sky2_F1	04_26_Sky2_F1	04_26_Sky2_F1	04_26_Sky2_F1	04_28_Sky2_F1	04_28_Sky2_F1	04_28_Sky2_F1	04_28_Sky2_F1	04_28_Sky2_F1	04_28_Sky2_F1	Minimum	Maximum	Median
t0	NaN	657.6000	677	676.6000	677	685.8000	538.8000	562.8000	578.7000	606.8000	651	1095	NaN	NaN	NaN
tf	NaN	669.1000	705	700	700	700	548.2000	573.8000	589.5000	626.6000	664.4000	1106	NaN	NaN	NaN
Dt	NaN	11.5000	28	23.4000	23	14.2000	9.4000	11	10.8000	19.8000	13.4000	11	NaN	NaN	NaN
CD0	0.0265	1.8113	0.2642	0.3060	0.2132	-0.4843	-0.8555	-0.5080	1.8853	0.0294	-14.6561	0.3224	-14.6561	1.8853	0.2132
CDV	0.1139	-0.3172	-0.0628	-0.1052	-0.0069	0.4206	0.6869	0.3915	-0.8197	-0.0854	14.0965	-0.1931	-0.8197	14.0965	-0.0628
CDa	-0.3460	-16.1665	0.6160	0.5936	0.5767	3.2972	2.1952	2.0353	-6.6902	1.9179	7.8488	1.4003	-16.1665	7.8488	1.4003
CL0	0.5046	-23.8677	2.2007	1.9686	2.2269	-0.1391	-0.9525	0.5445	-4.9634	-2.1034	-39.0919	1.2092	-39.0919	2.2269	-0.1391
CLV	1.1735	26.7677	-1.2807	-1.2393	-1.2936	0.1429	0.8855	-0.5413	7.4086	2.2891	38.5361	-1.1958	-1.2936	38.5361	0.1429
CLa	5.8154	-9.3246	2.2281	3.9497	2.0657	11.5677	10.1714	10.3855	-22.0346	8.4063	17.7478	9.5812	-22.0346	17.7478	8.4063
Cm0	0.0442	17.0829	-2.9408	-3.9485	-3.3208	-2.6684	-4.5435	-4.2745	-0.0454	-6.0035	-47.9698	-1.1283	-47.9698	17.0829	-3.3208
CmV	0.0171	-5.3957	1.0774	1.2648	1.2754	1.2302	2.6643	1.6668	-0.5509	3.3484	44.6507	0.5625	-5.3957	44.6507	1.2648
Cma	-0.9749	16.3661	-0.3699	-0.8864	-0.6538	1.1860	6.5072	1.0946	36.9204	1.9300	20.7307	1.3048	-0.8864	36.9204	1.3048
Cmq	-15.2330	-714.0246	-274.0696	-338.5013	-282.6534	-190.2927	-429.2495	-389.3033	-716.0290	-458.7322	-230.3610	-144.8514	-716.0290	-144.8514	-338.5...
Cmde	-1.0266	94.7551	-12.4467	-18.1596	-13.8402	-8.5331	-10.5896	-18.7228	10.4566	-18.5430	-11.1229	-4.2447	-18.7228	94.7551	-11.12...

It can be seen from the previous table that if no filtering is done: 1) the results change a lot from flight portion to another. 2) the derivatives in many cases have improper magnitudes and signs. For example, looking at C_{L_α}, it ranges from 9.6 to -22! C_{m_q} consistently has very large

magnitudes and ranges from -145 to -716! C_{m_α}, $C_{m_{de}}$ and the other derivatives also show these improper estimates. Therefore, the use of filtering before giving raw measurements to the EKF is needed.

Table 11-10: Results from portions matching criteria # 1. Low pass filtering applied to a_x, a_z, q & α.

	From AAA04_26_Sky2_F1	04_26_Sky2_F1	04_26_Sky2_F1	04_26_Sky2_F1	04_26_Sky2_F1	04_28_Sky2_F1	04_28_Sky2_F1	04_28_Sky2_F1	04_28_Sky2_F1	04_28_Sky2_F1	Minimum	Maximum	Median
t0	NaN	657.6000	677	676.6000	677	685.8000	538.8000	562.8000	578.7000	606.8000	651	1095	NaN	NaN	NaN
tf	NaN	669.1000	705	700	700	700	548.2000	573.8000	589.5000	626.6000	664.4000	1106	NaN	NaN	NaN
Dt	NaN	11.5000	28	23.4000	23	14.2000	9.4000	11	10.8000	19.8000	13.4000	11	NaN	NaN	NaN
CD0	0.0265	0.1075	0.5054	0.4281	0.4959	0.2315	-0.6406	-0.4144	0.0148	0.3479	0.5030	0.2882	-0.6406	0.5054	0.2882
CDV	0.1139	0.1789	-0.2181	-0.1456	-0.2006	-0.0343	0.5327	0.4508	0.2683	-0.0949	-0.1805	-0.1032	-0.2181	0.5327	-0.0949
CDa	-0.3460	-1.0748	-0.3260	-0.2781	-0.4061	0.6290	1.5421	0.2361	-1.6401	-1.2734	-1.8394	0.6803	-1.8394	1.5421	-0.3260
CL0	0.5046	3.5906	3.5371	3.1259	3.6696	2.7006	1.1403	0.9813	2.1539	2.4455	3.4059	1.0915	0.9813	3.6696	2.7006
CLV	1.1735	-1.7287	-1.9842	-1.6914	-2.0819	-1.3643	-0.9552	-0.2865	-0.7946	-1.2860	-1.9166	-0.7093	-2.0819	-0.2865	-1.3643
CLa	5.8154	-7.9916	-4.0436	-2.8833	-4.4136	-1.3011	7.6136	2.3496	-3.1116	-2.0595	-5.3730	5.2566	-7.9916	7.6136	-2.8833
Cm0	0.0442	-0.6418	-0.1464	-0.2659	-0.2032	-0.1928	-0.0647	-0.0300	-0.2277	-0.2041	-0.1039	-0.0880	-0.6418	-0.0300	-0.1928
CmV	0.0171	0.1869	0.0322	0.1306	0.0819	0.0715	0.0029	-0.0981	0.0479	0.1235	0.0426	0.0364	-0.0981	0.1869	0.0479
Cma	-0.9749	0.6983	-0.4811	-0.4449	-0.4603	-0.1711	0.1984	-0.2914	-0.2632	-0.0174	-0.5404	-0.0897	-0.5404	0.6983	-0.2632
Cmq	-15.2330	-30.5964	-17.2029	-19.3952	-17.7887	-11.9909	-17.0278	-12.6773	-21.1350	-18.4996	21.4921	-16.9645	-30.5964	21.4921	-17.20...
Cmde	-1.0266	-2.6297	-1.0991	-1.2209	-1.1355	-0.9276	-0.4291	-1.1652	-1.4927	-0.6655	-0.8429	-0.5495	-2.6297	-0.4291	-1.0991

In the previous table, the low pass filter was used again like in Table 11-6. However, this time, filtering was applied to a_z, a_z, q and α. This table was made to verify whether it is preferred to filter α or not. Comparing each row in the above table with Table 11-6, it can be seen that: filtering the angle of attack caused C_{L_α} and C_{D_α} to be negative in many flights. Which is not an expected sign for these derivatives. This is the main outcome of the comparison since other derivatives did not change much or the changes are less significant in importance. (For example, C_{D_0} did change much between both tables. However, as discussed in section 11.1.2 we do not care much about the value of C_{D_0} from the EKF.) Therefore, for the rest of the thesis, filtering will not be applied to α.

In summary, focusing on C_{L_α}, consistency between flights is not observed for the low pass and Spencer filters. The results from the filters low pass and Spencer filters have some weak consistency for portions from the same flight. It was decided not to use the moving average filter in the rest of the thesis since it may be falsifying the aircraft dynamics. It was also decided not to filter α but only filter a_x, a_z & q since filtering α yielded negative C_{L_α} and C_{D_α}. Thus, not filtering α is yielding more reasonable results.

11.3Consistency evaluation for several flight portions complying to set of criteria # 2

Comparison of system identification results for several flight portions complying to set of criteria # 2 is presented in this section. Set of criteria # 2 was presented in Section 9.2. In the following tables:

- Columns 3-6 show system identification results for flight portions obtained from Flight B. This flight took place on April 26, 2018.
- Columns 7-9 show system identification results for flight portions obtained from Flight A. This flight took place on April 28, 2018.
- Column 10 shows system identification results for a flight portion obtained from Flight C. This flight took place on April 28, 2018.

Thus, data from three flights was analyzed. The obtained flight portions mostly complied to set of criteria # 2. However, there were brief durations where not all the criteria applied. This was accepted since it was not possible to find long flight portions that perfectly applied to the criteria. a_x, a_z and q were filtered using the low pass filter in Table 11-11, the Spencer 15-point in Table 11-12 and the moving average 21-point in Table 11-13.

Table 11-11: Results from portions matching criteria # 2. Low pass filtering applied to a_x, a_z & q.

	From AAA	04_26_Sky2_F1	04_26_Sky2_F1	04_26_Sky2_F1	04_26_Sky2_F1	04_28_Sky2_F1	04_28_Sky2_F1	04_28_Sky2_F1	04_28_Sky2_F2	Minimum	Maximum	Median
t0	NaN	655.9000	682	655.9000	674.7000	536.1000	578.1000	614.5000	406.5000	NaN	NaN	NaN
tf	NaN	672.1000	696.4000	696.4000	696.4000	545.3000	592	624	415.1000	NaN	NaN	NaN
Dt	NaN	16.2000	14.4000	40.5000	21.7000	9.2000	13.9000	9.5000	8.6000	NaN	NaN	NaN
CD0	0.0265	0.1537	0.4761	0.3357	0.4396	-0.6272	-0.1522	-0.1502	-0.3493	-0.6272	0.4761	0.0018
CDV	0.1139	0.0625	-0.2641	-0.1232	-0.2064	0.5055	0.3507	0.3978	0.4094	-0.2641	0.5055	0.2066
CDa	-0.3460	-0.3096	0.4454	0.1211	0.1986	1.3727	-0.7212	-1.1150	1.2131	-1.1150	1.3727	0.1599
CL0	0.5046	2.3121	3.4206	2.1273	2.3272	1.0548	1.0792	0.3519	2.7839	0.3519	3.4206	2.2197
CLV	1.1735	-1.3226	-2.4642	-1.1422	-1.3500	-0.7068	-0.3951	0.0936	-1.8506	-2.4642	0.0936	-1.2324
CLa	5.8154	0.4972	1.8757	0.8482	1.3379	6.2073	4.1963	5.2585	1.9851	0.4972	6.2073	1.9304
Cm0	0.0442	-0.4664	-0.3917	-0.2936	-0.3723	-0.2894	-0.2554	-0.2266	-0.0742	-0.4664	-0.0742	-0.2915
CmV	0.0171	0.1191	0.1533	0.1056	0.1516	0.1293	0.0820	0.1391	-0.0081	-0.0081	0.1533	0.1242
Cma	-0.9749	0.0603	-0.3395	-0.2198	-0.4586	0.1701	-0.1308	-0.0531	0.8172	-0.4586	0.8172	-0.0919
Cmq	-15.2330	-22.0357	-22.5891	-22.3884	-28.4936	-24.0337	-19.7700	-16.7824	-20.3365	-28.4936	-16.7824	-22.21...
Cmde	-1.0266	-2.1671	-1.7208	-1.3332	-1.7210	-0.9545	-1.2692	-0.6456	-0.1072	-2.1671	-0.1072	-1.3012

Table 11-12: Results from portions matching criteria # 2. Spencer 15-point filtering applied to a_x, a_z & q.

	From AAA	04_26_Sky2_F1	04_26_Sky2_F1	04_26_Sky2_F1	04_26_Sky2_F1	04_28_Sky2_F1	04_28_Sky2_F1	04_28_Sky2_F1	04_28_Sky2_F2	Minimum	Maximum	Median
t0	NaN	655.9000	682	655.9000	674.7000	536.1000	578.1000	614.5000	406.5000	NaN	NaN	NaN
tf	NaN	672.1000	696.4000	696.4000	696.4000	545.3000	592	624	415.1000	NaN	NaN	NaN
Dt	NaN	16.2000	14.4000	40.5000	21.7000	9.2000	13.9000	9.5000	8.6000	NaN	NaN	NaN
CD0	0.0265	0.0933	0.4854	0.3057	0.4116	-0.6803	-0.2184	-0.1805	-0.3595	-0.6803	0.4854	-0.0436
CDV	0.1139	0.1068	-0.2698	-0.1016	-0.1856	0.5359	0.3827	0.4169	0.4240	-0.2698	0.5359	0.2447
CDa	-0.3460	-0.1110	0.4563	0.2481	0.3166	1.6065	-0.3283	-0.9837	1.1953	-0.9837	1.6065	0.2823
CL0	0.5046	2.1343	3.4564	1.9977	2.3016	0.9709	0.9928	0.2805	2.7015	0.2805	3.4564	2.0660
CLV	1.1735	-1.2652	-2.4937	-1.0572	-1.3455	-0.6598	-0.3314	0.1699	-1.7963	-2.4937	0.1699	-1.1612
CLa	5.8154	1.9233	1.9589	1.4789	1.6787	6.7833	4.6211	5.3617	2.5452	1.4789	6.7833	2.2520
Cm0	0.0442	-0.4228	-0.3299	-0.2405	-0.3165	-0.2457	-0.2061	-0.1894	-0.0122	-0.4228	-0.0122	-0.2431
CmV	0.0171	0.1073	0.1280	0.0832	0.1241	0.1102	0.0498	0.1181	-0.0430	-0.0430	0.1280	0.1088
Cma	-0.9749	-0.0491	-0.2899	-0.2300	-0.3887	0.1581	-0.1203	-0.0656	0.6358	-0.3887	0.6358	-0.0929
Cmq	-15.2330	-17.1942	-18.3735	-17.9380	-24.8379	-19.6505	-15.7793	-13.4396	-13.9777	-24.8379	-13.4396	-17.56...
Cmde	-1.0266	-2.0233	-1.4502	-1.1338	-1.4852	-0.7860	-1.1368	-0.5323	-0.0161	-2.0233	-0.0161	-1.1353

Table 11-13: Results from portions matching criteria # 2. Moving average 21-point filtering applied to a_x, a_z & q.

	From AAA	04_26_Sky2_F1	04_26_Sky2_F1	04_26_Sky2_F1	04_26_Sky2_F1	04_28_Sky2_F1	04_28_Sky2_F1	04_28_Sky2_F1	04_28_Sky2_F2	Minimum	Maximum	Median
t0	NaN	655.9000	682	655.9000	674.7000	536.1000	578.1000	614.5000	406.5000	NaN	NaN	NaN
tf	NaN	672.1000	696.4000	696.4000	696.4000	545.3000	592	624	415.1000	NaN	NaN	NaN
Dt	NaN	16.2000	14.4000	40.5000	21.7000	9.2000	13.9000	9.5000	8.6000	NaN	NaN	NaN
CD0	0.0265	0.1209	0.4781	0.2457	0.2300	-0.6972	-0.4041	-0.2417	-0.3142	-0.6972	0.4781	-0.0604
CDV	0.1139	0.0469	-0.2950	-0.0930	-0.0888	0.5270	0.4401	0.3408	0.4074	-0.2950	0.5270	0.1939
CDa	-0.3460	0.2098	0.7594	0.7583	1.1464	1.9103	1.0927	0.4032	0.8486	0.2098	1.9103	0.8040
CL0	0.5046	1.9879	3.3317	1.6710	1.9028	0.7772	0.5168	0.2084	2.2639	0.2084	3.3317	1.7869
CLV	1.1735	-1.3621	-2.5646	-0.9525	-1.1930	-0.5872	-0.1127	0.0774	-1.5651	-2.5646	0.0774	-1.0728
CLa	5.8154	4.3895	3.7855	3.7210	4.0316	8.1433	7.4052	7.0569	5.0408	3.7210	8.1433	4.7152
Cm0	0.0442	-0.0831	-0.0750	-0.0297	-0.1506	-0.0244	-0.0053	-0.0933	0.0921	-0.1506	0.0921	-0.0524
CmV	0.0171	0.0132	0.0297	-0.0069	0.0550	0.0068	-0.0267	0.0580	-0.0736	-0.0736	0.0580	0.0100
Cma	-0.9749	-0.0038	-0.0651	0.0154	-0.0148	0.0525	0.0271	-0.0128	-0.0470	-0.0651	0.0525	-0.0083
Cmq	-15.2330	0.5637	-3.8666	-1.2818	-11.3378	-0.9399	1.4845	-5.3390	4.6960	-11.3378	4.6960	-1.1108
Cmde	-1.0266	-0.3690	-0.2862	-0.1619	-0.5900	-0.0102	-0.1397	-0.2226	0.1510	-0.5900	0.1510	-0.1923

Focusing on C_{L_α} results,

In the low pass filtering case, the estimation of C_{L_α} showed large variation with estimates ranging from 0.5 to 6.2. However, the results from each flight have a smaller range. The first flight (columns 3-6) has range from 0.5 to 1.9. The second flight (columns 7 to 9) has range from 4.2 to 6.2. The third flight (column 10) is ~2.0. To summarize,

1) The estimates vary widely in the results. There is inconsistency in the EKF results.
2) However, in the same flight, the estimates from different flight portions showed some weak consistency.
3) This same observation can be seen in C_{L_α} estimates when the 15-point Spencer filter or 21-point moving average filter were used

4) The AAA estimation lies in the range of the EKF estimates seen in each of the three tables.

Focusing on C_{m_α} results,

1) The estimates vary widely in the results ranging from -0.46 to 0.82. There is inconsistency in the EKF results.
2) However, in the same flight, the estimates from different flight portions showed some slight signs of weak consistency. These slight signs are that estimate from a given flight were in a smaller range than the range mentioned in point (1). For flight B, three results were in the range from -0.22 to -0.46. For Flight A, two results (-0.13 & -0.05) had reasonable sign and were close to each other.
3) The same could be said for the results obtained from the spencer filter.
4) The AAA estimate is always much more negative than the EKF results for C_{m_α} in each of the three tables.

Focusing on C_{m_q} results,

1) In low pass filter results: the estimates vary widely in the results ranging from -28 to -17. There is inconsistency in the EKF results.
2) In low pass filter results: a slight sign of consistency seen in Flight B results. $C_{m_q} \approx -22$ is repeated in Flight B result more than once.
3) The C_{m_q} estimation is closer to AAA when the low pass filter or the Spencer filter are used.
4) When the moving average filter is used the C_{m_q} estimation is smaller in magnitude than the other two filters and the AAA estimate and, in some instances, has an incorrect sign.

Again, the moving average filter may be falsifying the aircraft dynamics as mentioned in Section 11.2.2.

Focusing on $C_{m_{de}}$ results,

1) For the low pass filter: the results ranged from -2.2 to -0.1. This is a large variation. Most results however were in the range -1.7 to -0.6. This is still a large variation. Thus, there is inconsistency in the EKF results.
2) The AAA estimate is within the ranges mentioned above. And the above ranges are also within the limits of expected results seen in Section 11.1.3. Thus, the obtained results have reasonable values.
3) For the Spencer filter, results are frequently within the range: -1.49 to -0.78. This is similar to the low pass results range.
4) For the moving average filter, the estimation is repeatedly in the range between -0.14 to -0.59. This is a lower range than the other two filters and the AAA estimate does not lie in this range.

11.4Stitching of flight data and EKF results

As mentioned previously, it is difficult to obtain long flight portions that match criteria #2. Therefore, flight data were stitched together to obtain long portions that match criteria #2. Section 9.3 discusses this issue. In this section, EKF results for stitched flight portions is presented.

11.4.1 System identification results from stitched portions from Flight B

In this portion system identification results are presented when several flight portions are stitched from Flight B. All the flight portions match set of Criteria #2. Section 9.3.2 shows where

these flight portions occur during flight. To continue evaluation of the different filters, results are presented in the following table based on:

1) Low pass filtering of a_x, a_z & q.
2) 15-point Spencer filtering of a_x, a_z & q.
3) 21-point moving average filtering of a_x, a_z & q.

Table 11-14: System Identification using the Stitched flight portions from Flight B mentioned in Section 9.3.2.

Low Pass			15-point Spencer			21-point moving average		
	From AAA	04_26_Sky2_F1		From AAA	04_26_Sky2_F1		From AAA	04_26_Sky2_F1
CD0	0.0265	-0.4369	CD0	0.0265	-0.4608	CD0	0.0265	-0.4742
CDV	0.1139	0.2985	CDV	0.1139	0.3191	CDV	0.1139	0.2962
CDa	-0.3460	3.3246	CDa	-0.3460	3.3894	CDa	-0.3460	3.7701
CL0	0.5046	2.1749	CL0	0.5046	2.1574	CL0	0.5046	2.0422
CLV	1.1735	-1.3709	CLV	1.1735	-1.3493	CLV	1.1735	-1.3427
CLa	5.8154	2.8396	CLa	5.8154	2.9404	CLa	5.8154	4.0520
Cm0	0.0442	-0.1665	Cm0	0.0442	-0.1477	Cm0	0.0442	-0.0787
CmV	0.0171	0.1086	CmV	0.0171	0.0948	CmV	0.0171	0.0270
Cma	-0.9749	-0.3064	Cma	-0.9749	-0.2841	Cma	-0.9749	-0.0923
Cmq	-15.2330	-21.2736	Cmq	-15.2330	-17.2698	Cmq	-15.2330	-7.6524
Cmde	-1.0266	-0.6634	Cmde	-1.0266	-0.6117	Cmde	-1.0266	-0.4702

The following can be observed:

1) C_{L_α} from the low pass and Spencer filters are both about 2.9. The moving average filter has C_{L_α} of 4.05. These are all reasonable values for C_{L_α}.
2) C_{m_α} from the low pass and Spencer filters yield a value of about -0.3 while the moving average filter yields a value of -0.1. The results are lower in magnitude than AAA estimate but they are in an acceptable range.
3) C_{m_q} and $C_{m_{de}}$ estimates are also reasonable for all three filters. The low pass and Spencer filters are closer to the AAA estimate.

11.4.2 Comparison of stitched flight portions from Flights A, B & C

In the section, comparison is made between system identification results obtained when data is stitched from three flights. The results are presented in the following table. The columns of the table show results when all flight portions matching set of criteria # 2 in Flight A, B and C,

respectively, are analyzed. These portions are identified in Sections 9.3.1, 9.3.2 and 9.3.3. The rows of the table indicate the filtering on a_x, a_z and q measurements.

Table 11-15: Results from stitched data from three flights.

Filtering	Stitched portions from Flight A		Stitched portions from Flight B		Stitched portions from Flight C	
Low Pass	From AAA04_28_Sky2_F1		From AAA04_26_Sky2_F1		From AAA04_28_Sky2_F2	
CD0	0.0265	-0.2975	0.0265	-0.4369	0.0265	-0.0523
CDV	0.1139	0.2829	0.1139	0.2985	0.1139	0.0854
CDa	-0.3460	1.3602	-0.3460	3.3246	-0.3460	1.8934
CL0	0.5046	0.7308	0.5046	2.1749	0.5046	2.4940
CLV	1.1735	-0.4099	1.1735	-1.3709	1.1735	-1.4939
CLa	5.8154	7.1489	5.8154	2.8396	5.8154	-1.1302
Cm0	0.0442	-0.1383	0.0442	-0.1665	0.0442	-0.1417
CmV	0.0171	0.0472	0.0171	0.1086	0.0171	0.0066
Cma	-0.9749	-0.0889	-0.9749	-0.3064	-0.9749	0.2253
Cmq	-15.2330	-19.7883	-15.2330	-21.2736	-15.2330	-29.1779
Cmde	-1.0266	-0.8061	-1.0266	-0.6634	-1.0266	-0.8852
Spencer	From AAA04_28_Sky2_F1		From AAA04_26_Sky2_F1		From AAA04_28_Sky2_F2	
CD0	0.0265	-0.3261	0.0265	-0.4608	0.0265	-0.0660
CDV	0.1139	0.2972	0.1139	0.3191	0.1139	0.0954
CDa	-0.3460	1.5348	-0.3460	3.3894	-0.3460	1.9819
CL0	0.5046	0.6832	0.5046	2.1574	0.5046	2.5069
CLV	1.1735	-0.3749	1.1735	-1.3493	1.1735	-1.4901
CLa	5.8154	7.4590	5.8154	2.9404	5.8154	-1.1619
Cm0	0.0442	-0.1164	0.0442	-0.1477	0.0442	-0.1320
CmV	0.0171	0.0369	0.0171	0.0948	0.0171	0.0057
Cma	-0.9749	-0.0983	-0.9749	-0.2841	-0.9749	0.1831
Cmq	-15.2330	-17.0030	-15.2330	-17.2698	-15.2330	-26.3365
Cmde	-1.0266	-0.7226	-1.0266	-0.6117	-1.0266	-0.8496
Moving Average	From AAA04_28_Sky2_F1		From AAA04_26_Sky2_F1		From AAA04_28_Sky2_F2	
CD0	0.0265	-0.4138	0.0265	-0.4742	0.0265	-0.0986
CDV	0.1139	0.3107	0.1139	0.2962	0.1139	0.1137
CDa	-0.3460	2.3340	-0.3460	3.7701	-0.3460	2.1270
CL0	0.5046	0.5408	0.5046	2.0422	0.5046	2.4397
CLV	1.1735	-0.3433	1.1735	-1.3427	1.1735	-1.3893
CLa	5.8154	8.6403	5.8154	4.0520	5.8154	-1.4372
Cm0	0.0442	-0.0379	0.0442	-0.0787	0.0442	-0.0621
CmV	0.0171	0.0068	0.0171	0.0270	0.0171	0.0098
Cma	-0.9749	-0.0405	-0.9749	-0.0923	-0.9749	-0.0535
Cmq	-15.2330	-8.9941	-15.2330	-7.6524	-15.2330	-11.8307
Cmde	-1.0266	-0.3211	-1.0266	-0.4702	-1.0266	-0.4646

Looking at the previous table, it can be seen that:

1) For the low pass filter, different flights yield different estimates for many derivatives. For example, C_{L_α} estimates in the three flights are very different. In one flight is 2.84, in another it is 7.15 while the third flight yields -1.13, a negative value.
2) The spencer filter and moving average filter also show a variation in the C_{L_α} estimate.
3) Looking at $C_{m_{de}}$ where the low pass filter is used, it can be seen that the estimates are in a certain range, between -0.885 and -0.663.

11.4.3 Further Comparison of stitched flight portions from Flights A, B & C

To continue evaluating the consistency in the EKF results, the following tables shows more system identification results. Results are presented for stitched flight portions from Flights A, B and C, again. The same flight portions used in the previous section are used. These are the flight portions mentioned in Sections 9.3.1, 9.3.2 and 9.3.3. However, this time, comparison is made between using all the flight portions or a smaller number of portions. For example, Flight B has 6 portions that match Set of Criteria #2, as can be seen in Section 9.3.2. Comparison will be made between running the EKF on all 6 sections or on a smaller number of sections.

For brevity, only the low pass filter is used. It was chosen since it is better at preserving the low frequencies than the moving average filter as discussed in Sections 7.3 and 11.2.2. The Spencer filter could have been chosen instead under that same reasoning. Also, for brevity, the discussion in the following paragraphs focuses mostly on C_{L_α} with little discussion about other derivatives. Similar reasoning can be used to investigate the other derivatives. The row containing C_{L_α} results is highlighted to make discussion easier.

Table 11-16: Results obtained from running the EKF on different sections from Flight A.[3]

Section #	AAA	All	1-10	1-9	1-8	1-7	2-11	3-11	4-11	5-11	1,5-11	1,2,5-11
Total Duration	-	**50.95**	**47.7**	**42.65**	**39**	**35.45**	**46.2**	**42.05**	**38.55**	**34.35**	**39.1**	**43.25**
CD0	0.0265	-0.2975	-0.1905	-0.1928	-0.3094	-0.3126	-0.6162	-0.3796	-0.1958	-0.1814	0.1999	-0.206
CDV	0.1139	0.2829	0.2498	0.2579	0.3069	0.316	0.5467	0.3974	0.3215	0.3139	0.0298	0.2375
CDa	-0.346	1.3602	0.4605	0.371	0.9907	0.8767	2.0617	1.2819	0.2375	0.2514	-0.9442	0.9625
CL0	0.5046	0.7308	0.6389	0.5916	0.5538	0.512	0.6064	0.8987	1.0557	1.1521	1.2906	0.756
CLV	1.1735	-0.4099	-0.3276	-0.2751	-0.2692	-0.2379	-0.2248	-0.4075	-0.4871	-0.556	-0.6728	-0.4277
CLa	5.8154	7.1489	7.2606	7.0745	7.4195	7.5857	6.4548	5.4819	4.7802	4.5676	4.3537	7.1639
Cm0	0.0442	-0.1383	-0.1265	-0.1253	-0.1239	-0.1314	-0.146	-0.1602	-0.1762	-0.1776	-0.1528	-0.146
CmV	0.0171	0.0472	0.0268	0.0195	0.0195	0.0218	0.0484	0.0603	0.072	0.0818	0.0598	0.0581
Cma	-0.9749	-0.0889	-0.1177	-0.1491	-0.1855	-0.2208	-0.0772	-0.0754	-0.0425	-0.0226	-0.0342	-0.0508
Cmq	-15.233	-19.7883	-18.615	-18.6249	-19.1675	-20.0135	-19.8889	-20.7736	-21.6605	-21.6762	-21.0735	-20.7594
Cmde	-1.0266	-0.8061	-0.8814	-0.9474	-0.9594	-1.016	-0.8452	-0.8636	-0.8739	-0.7997	-0.7844	-0.7606

[3] Section numbers are as defined in Section 9.3.1

Table 11-17: Results obtained from running the EKF on different sections from Flight B.[4]

Section #	AAA	All	1-5	1-4	2-6	3-6	3,5,6	1,2,4,5,6	1,2,3,5,6	1,2,3,4,6	1,2	1,2,3	4,5,6	1,3-6
Total Duration	-	**47.00**	**32.60**	**29.00**	**41.50**	**37.35**	**34.20**	**30.80**	**43.85**	**43.40**	**9.65**	**25.85**	**21.15**	**42.85**
CD0	0.0265	-0.4369	-0.5353	-0.5547	-0.2763	0.2323	0.2335	-0.693	-0.4247	-0.4588	-0.5045	-0.5443	0.3363	-0.2277
CDV	0.1139	0.2985	0.4139	0.4167	0.1957	-0.0524	-0.0659	0.5305	0.2735	0.2972	0.6081	0.4006	-0.1047	0.1471
CDa	-0.346	3.3246	2.9816	3.0839	2.8164	0.4053	0.508	3.6457	3.4109	3.5267	-1.1889	3.0299	0.1933	2.7681
CL0	0.5046	2.1749	2.1046	2.2047	1.8223	2.3843	2.5671	1.8775	2.3218	2.2384	1.1738	2.3548	2.2077	2.5867
CLV	1.1735	-1.3709	-1.2428	-1.3391	-1.132	-1.5069	-1.643	-1.1064	-1.5041	-1.4424	-0.8531	-1.4914	-1.31	-1.5714
CLa	5.8154	2.8396	2.0053	1.9739	3.7284	1.9854	1.6813	3.4025	2.8216	2.9584	10.4224	2.1689	1.9651	0.8368
Cm0	0.0442	-0.1665	-0.181	-0.1919	-0.2236	-0.2235	-0.2116	-0.1346	-0.1457	-0.1699	-0.0735	-0.1504	-0.1933	-0.1908
CmV	0.0171	0.1086	0.1185	0.1186	0.1119	0.1189	0.1121	0.0846	0.0995	0.1077	0.0431	0.1027	0.0957	0.1244
Cma	-0.9749	-0.3064	-0.2386	-0.1247	-0.293	-0.2601	-0.3072	-0.4183	-0.3446	-0.2458	-0.7468	-0.1754	-0.4021	-0.2426
Cmq	-15.233	-21.2736	-22.0924	-21.9372	-23.25	-22.5671	-23.1738	-18.7713	-21.4749	-20.7959	-18.4481	-21.5898	-20.4495	-21.8144
Cmde	-1.0266	-0.6634	-0.6654	-0.6727	-1.0087	-0.937	-0.9318	-0.659	-0.6119	-0.6555	-0.6718	-0.5418	-0.9629	-0.674

Table 11-18: Results obtained from running the EKF on different sections from Flight C.[5]

Section #	AAA	All	2-6	3-6	3,4,5	1-5	1,3-6
Total Duration	-	**30.55**	**27.4**	**18.85**	**14.65**	**26.35**	**22**
CD0	0.0265	-0.0523	0.0227	0.1051	0.0582	-0.0809	0.0245
CDV	0.1139	0.0854	-0.0097	-0.0826	-0.0495	0.1125	0.0286
CDa	-0.346	1.8934	2.1457	2.1255	2.1657	1.8116	1.7788
CL0	0.5046	2.494	2.5574	2.2556	2.4222	2.5946	2.1875
CLV	1.1735	-1.4939	-1.4708	-1.2886	-1.3904	-1.5873	-1.2652
CLa	5.8154	-1.1302	-1.882	-1.1979	-1.4445	-0.8455	-0.8552
Cm0	0.0442	-0.1417	-0.1228	-0.1351	-0.1509	-0.1575	-0.1498
CmV	0.0171	0.0066	0.0152	0.0226	0.03	0.0128	0.0084
Cma	-0.9749	0.2253	0.1353	0.0133	-0.0375	0.1639	0.1692
Cmq	-15.233	-29.1779	-22.6975	-21.0307	-22.6199	-32.2928	-30.776
Cmde	-1.0266	-0.8852	-0.7461	-0.874	-0.9598	-0.991	-0.9729

Looking at the C_{L_α} results, it can be seen that the estimation is reasonable in many cases. However, the values vary significantly from flight to flight. Also, as it was mentioned in previous sections, the variation in results from the same flight data is smaller. For example, for Flight B results shown in Table 11-17, the estimated C_{L_α} varies depending on the flight portions used. However, all the columns show C_{L_α} around 0.8 to 3.7 except one column. This is a smaller range of variation than the range in which results from all flights occur (-1.88 to 7.59).

That one column that has a value much further than the rest in Table 11-17 is column 12. It has $C_{L_\alpha} = 10.4\, rad^{-1}$. It is noticed that the flight data used for this estimation has a short

[4] Section numbers are as defined in Section 9.3.2
[5] Section numbers are as defined in Section 9.3.3

duration (~ 10 sec.). Looking at the C_{L_α} estimation as time progresses, it can be seen that the EKF did not converge on a value as seen in the following figure.

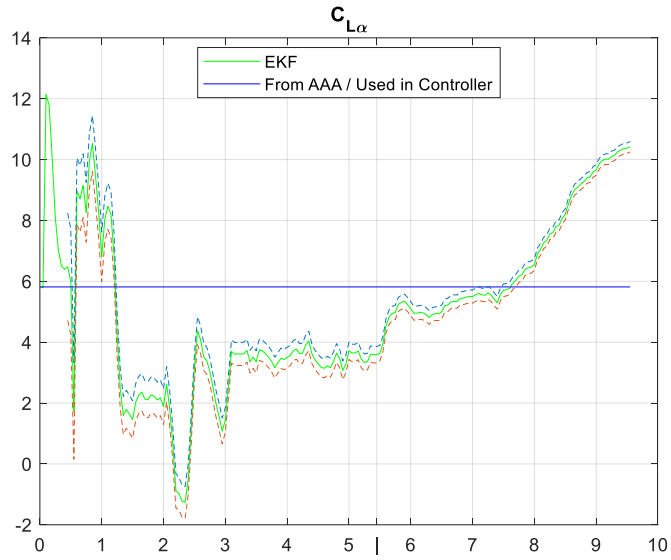

Figure 11-1: C_{L_α} estimation over time for flight data from column 12 of Table 11-17.

Loosely speaking, it could be said that Flight A results show $C_{L_\alpha} = 6.3 \pm 1.95\ rad^{-1}$, Flight B results show $C_{L_\alpha} = 2.36 \pm 1.53\ rad^{-1}$ and Flight C results show $C_{L_\alpha} = -1.23 \pm 0.66\ rad^{-1}$. These variations are not small. However, they are much smaller than the variation if results from all Flights are used. If the results from all flights are used, we would get $C_{L_\alpha} = 3.11 \pm 5\ rad^{-1}$! The way these estimates are made is by evaluating the average, minimum and maximum values for the data. These statistics are shown in the following table.

Table 11-19: Statistics for C_{L_α} results in this section.

	Min.	***Max.***	***Avg.***	$\|Avg - min\|$	$\|Avg - max\|$	**Estimate**
Flight A	4.35	7.59	6.30	1.95	1.29	6.30±1.95
Flight B	0.84	3.73	2.36	1.53	1.36	2.36±1.53
Flight C	-1.88	-0.85	-1.23	0.66	0.38	-1.23±0.66
All Flights	-1.88	7.59	3.11	5.00	4.47	3.11±5.00

This shows that results from each flight was in a different region than the other flight. Thus, overall, the results are not consistent. On the other hand, some weak consistency is seen within results from the same flight. This weak consistency is over a wide region, however.

One observation was made concerning how the EKF functions while preparing this section. It was observed that the EKF estimates depended largely on the initial seconds of data given to the EKF. On the other hand, the effect of the data towards the end on the estimates is smaller. This is reasonable since the EKF covariance matrix, P, is large at the beginning and it gets smaller and smaller with time. This makes the EKF very responsive at the beginning since it is expecting that the estimated derivatives have large errors. As time proceeds, and the P matrix elements get smaller, the EKF is expecting that the error in the estimates is smaller. Thus, the EKF still changes the estimated derivatives but with a much lower sensitivity.

This was noticed while preparing this section as follows: It was observed that the initial data sections dictated to a noticeable degree the system identification results. Therefore, when data sections were removed from the end of the stitched data, they did not affect the system identification results as much as when data sections were removed from the initial seconds. This can be seen in Table 11-16. In columns 3 to 7, the initial sections were the same, and the resulting system identification results were similar. C_{L_α}, for example, was consistently around $7\ rad^{-1}$. However, in columns 7-11, where the initial sections were changed, the estimated derivatives changed more noticeably. For example, C_{L_α} went from around 7.5 to around 6.5 to 5.5 to 4.8 to 4.6.

11.5Estimation of two more stability and control derivatives ($C_{L_{\delta e}}$ and C_{L_q})

Experimentation with estimating two more stability and control derivatives was performed. These two derivatives are C_{L_q} and $C_{L_{\delta e}}$. The following tables show the results

obtained when the $C_{L_{de}}$ derivative alone is added and when both derivatives were added. Adding the derivatives simply meant adding them in the C_L equation used in the EKF. For example:

$$C_L = C_{L0} + C_{LV}\frac{V}{V_0} + C_{L\alpha}\alpha + C_{Lq}\frac{q\bar{c}}{2V_0} + C_{L\delta_e}\delta_e \qquad \text{Eq 11-1}$$

To simplify the presentation of results, only the results from the low pass filter are presented. (only a_x, a_z & q are filtered. Results are presented for Flights A, B and C in the following tables. The stitched flight data mentioned in Sections 9.3.1 to 9.3.3 were used from these flights.

Table 11-20: Derivative estimation when two more derivatives are added. Results for Flight A.

	AAA	**Original**	**$C_{L_{de}}$ added**	**$C_{L_{de}}$ &C_{L_q} added**
C_{D0}	0.0265	-0.2975	-0.3128	-0.3207
C_{DV}	0.1139	0.2829	0.2941	0.2971
$C_{D\alpha}$	-0.346	1.3602	1.3943	1.4454
C_{L0}	0.5046	0.7308	0.124	-0.4467
C_{LV}	1.1735	-0.4099	-0.7349	-0.4238
$C_{L\alpha}$	5.8154	7.1489	4.6005	4.9683
C_{Lq}	6.337	~	~	-66.8437
C_{Lde}	0.2931	~	-8.1603	-9.9263
C_{m0}	0.0442	-0.1383	-0.1396	-0.1388
C_{mV}	0.0171	0.0472	0.0497	0.0498
$C_{m\alpha}$	-0.9749	-0.0889	-0.0778	-0.0806
C_{mq}	-15.233	-19.7883	-19.8732	-19.6375
C_{mde}	-1.0266	-0.8061	-0.7905	-0.7859

Table 11-21: Derivative estimation when two more derivatives are added. Results for Flight B.

	AAA	Original	$C_{L_{de}}$ added	$C_{L_{de}}$ &C_{L_q} added
C_{D0}	0.0265	-0.4369	-0.3976	-0.3992
C_{DV}	0.1139	0.2985	0.2472	0.2491
$C_{D\alpha}$	-0.346	3.3246	3.3818	3.3795
C_{L0}	0.5046	2.1749	-0.7681	-0.7974
C_{LV}	1.1735	-1.3709	-1.0404	-1.0178
$C_{L\alpha}$	5.8154	2.8396	5.9611	5.937
C_{Lq}	6.337	~	~	-5.4711
C_{Lde}	0.2931	~	-14.6503	-14.716
C_{m0}	0.0442	-0.1665	-0.1592	-0.1593
C_{mV}	0.0171	0.1086	0.109	0.1089
$C_{m\alpha}$	-0.9749	-0.3064	-0.3249	-0.3243
C_{mq}	-15.233	-21.2736	-21.6982	-21.6702
C_{mde}	-1.0266	-0.6634	-0.6275	-0.6285

Table 11-22: Derivative estimation when two more derivatives are added. Results for Flight C.

	AAA	Original	$C_{L_{de}}$ added	$C_{L_{de}}$ &C_{L_q} added
C_{D0}	0.0265	-0.0523	-0.0461	-0.0472
C_{DV}	0.1139	0.0854	0.0569	0.0579
$C_{D\alpha}$	-0.346	1.8934	2.1257	2.1253
C_{L0}	0.5046	2.494	0.427	0.3818
C_{LV}	1.1735	-1.4939	-1.1333	-1.1143
$C_{L\alpha}$	5.8154	-1.1302	-0.9233	-0.9399
C_{Lq}	6.337	~	~	-11.8039
C_{Lde}	0.2931	~	-11.9392	-12.1617
C_{m0}	0.0442	-0.1417	-0.1507	-0.1511
C_{mV}	0.0171	0.0066	0.005	0.0048
$C_{m\alpha}$	-0.9749	0.2253	0.2227	0.2239
C_{mq}	-15.233	-29.1779	-29.4757	-29.6461
C_{mde}	-1.0266	-0.8852	-0.9652	-0.9685

Analyzing the results in the previous three tables, it was seen that the estimated C_{L_q} and $C_{L_{de}}$ estimates always had improper sign. They were always negative. As for the effect of adding these two derivatives on the overall system identification, it was observed that C_{L_α} derivative in the first two tables changed notably but not in the third table. Other derivatives mostly did not change much. In Table 11-20, C_{L_α} was 7.14 and it decreased to about 4.6 or 5 after adding the

two additional derivatives. In Table 11-21, the derivative increased from 2.8 to about 5.9. C_{L_α} remained about the same in the third table at about -1.

Thus, C_{L_α} came closer to AAA in two flights and the estimates from both flights agreed. The third flight, however, has an unreasonable estimate for C_{L_α}. At this point, these changes may or may not be an improvement in getting C_{L_α}. It is not certain since we do not know the true value of C_{L_α}.

One important thing to note is that this investigation is made only on three sets of data. It is not in depth, but it is an initial look at the effect of adding these two derivatives. In summary:

1) The estimates for the two added derivatives are not reasonable.
2) Adding the two derivatives affected mostly C_{L_α} but not the other derivatives.
3) C_{L_α} estimates may or may not have improved. It is not clear since not all three flights agree, and we do not know the true value of C_{L_α}

11.6Overall observations

This section makes overall observations regarding the consistency in the EKF results. These observations are made with the aid of Figure 11-2 on page 141. In that figure, system identification results from Sections 11.2.2, 11.3 and 11.4.3 for the derivatives $C_{L_\alpha}, C_{m_\alpha}, C_{m_q}$ & $C_{m_{de}}$ are collected and presented visually. These are the results obtained when the low pass filter is used to filter a_x, a_z & q. In the figure, the results obtained from each flight is put on a different row and given a different color. For comparison, the AAA estimates for these derivatives, which were presented in Table 3-4, are plotted. Estimates from two AAA models are presented.

Looking at the C_{L_α} estimates in the figure, it can be seen that:

1) The results are spread over a very wide range (i.e. inconsistency). They range from about -2 to about 10.5.
2) The majority of results from individual flights are in smaller ranges. Flight A estimates mostly lie between 4 and 8, Flight B estimates mostly between 0 and 4, Flight C estimates mostly between -1 and -2. Individual flights have considerable inconsistency, but it is lower than the inconsistency in all the flights combined.
3) Several of the estimates are reasonable compared to AAA and the expected ranges.
4) Flight A estimates are mostly higher than Flight B estimates which are mostly higher than Flight C estimates.
5) The AAA estimate from the model using the GEO 438 airfoil is at the center of the estimates from Flight A. The estimate from the ClarkY airfoil is at the lower and upper boundaries of results from Flight A and B respectively.
6) Most estimates from Flight C are unreasonable since they are negative.

Looking at the C_{m_α} estimates:

1) Again, there is a large spread in the results. (i.e. inconsistency). They range from about -1 to 0.4.
2) The majority of results from individual flights are in smaller ranges. Flight A estimates mostly lie between -0.3 and 0, Flight B estimates mostly between -0.5 and -0.1, Flight C estimates mostly between -0.05 and 0.25. Individual flights have considerable inconsistency, but it is lower than the inconsistency in all the flights combined.
3) The results are in the expected range given in Section 11.1.3.
4) Flight A estimates are centered at a lower magnitude than Flight B.

5) The AAA estimates are higher in magnitude than all EKF estimate except for one result. Most results are at least 0.4 rad^{-1} lower in magnitude than AAA.
6) Most estimates from flight C are positive. This is not expected since it would indicate the SkyHunter is unstable.

Looking at the C_{m_q} estimates.

1) The results are spread over a very wide range (i.e. inconsistency). They range from about -34 to about -10. There is one estimate at 20 which is unreasonable.
2) The majority of results from individual flights are in a smaller region. Flight A estimates mostly lie between -22 and -16, Flight B estimates mostly between -24 and -18. This can be seen more clearly in the zoomed in plot in Figure 11-3. The limited estimates from Flight C are spread out.
3) Most the results are comparable to the theoretical estimate from AAA and are in the expected range presented in Section 11.1.3.
4) Estimates from flights A are centered at a lower magnitude than Flight B.
5) The AAA estimates are mostly lower in magnitude than the EKF estimation.

Looking at the $C_{m_{de}}$ estimates:

1) The results are spread over a very wide range (i.e. inconsistency). They range from about -2.5 to about -0.5.
2) Many results are reasonable and are in the expected range presented in Section 11.1.3. Some results are comparable to the theoretical estimate from AAA.
3) Estimates from Flight B has similar inconsistency to estimates from all Flights combined.
4) Estimates from Flight B have higher inconsistency (i.e. are more spread out) than estimates from Flight A.

5) AAA estimates are comparable to the higher magnitude results obtained from the EKF.

In Summary,

1) There is considerable inconsistency in the EKF results
2) Results from individual flights is considerably inconsistent. However, for some derivatives, the inconsistency in individual flights is lower than that in all flights combined.
3) The results are reasonable in several cases.
4) The majority of results lie in the expected ranges presented in Section 11.1.3.
5) The AAA estimates are:
    a. Comparable to some EKF results for C_{L_α}
    b. Higher in magnitude than EKF results for C_{m_α}
    c. Lower in magnitude than most EKF results for C_{m_q}
    d. Comparable to some of the higher magnitude EKF results for $C_{m_{de}}$.

Overall, the EKF estimates, were reasonable in several cases. However, the estimates from different flight portions, have considerable inconsistency. Chapter 12 discusses several reasons for this inconsistency.

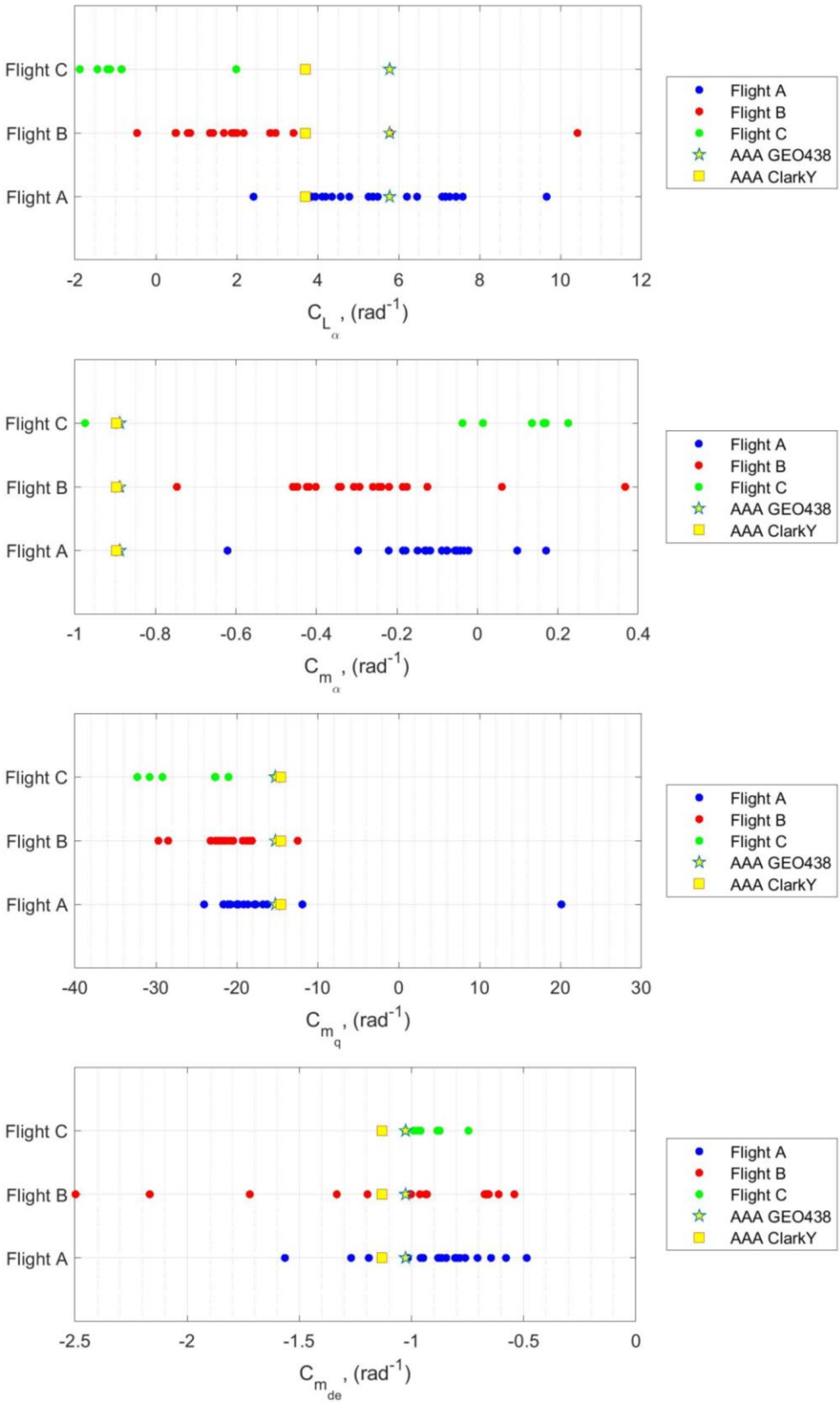

Figure 11-2: Summary of obtained $C_{L_\alpha}, C_{m_\alpha}, C_{m_q}$ & $C_{m_{de}}$ estimates from the different flights and flight portions. Low pass filtering used on a_x, a_z and q.

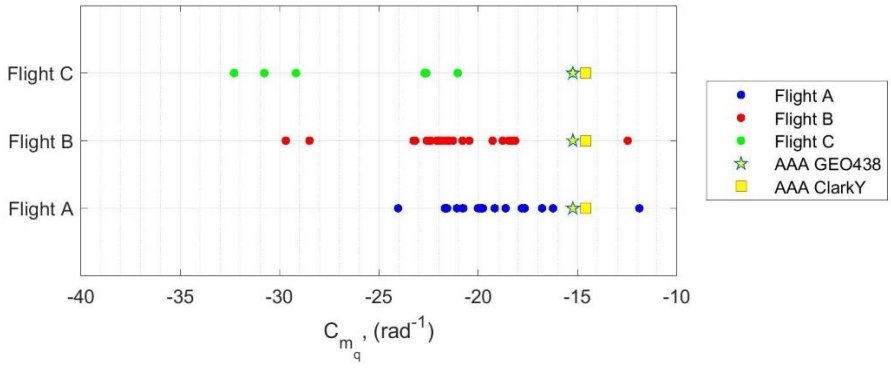

Figure 11-3: Zoomed in view of C_{m_q} estimates after removing the single outlying positive estimate.

11.7Summary

To recap, in this chapter, several system identification results were presented. Results were presented for[6]:

1) Flight portions following set of criteria #1
2) Flight portions following set of criteria #2
3) Flight portions obtained by stitching several portions matching set of criteria #2. This was done since flight portions matching set of criteria #2 were of short duration.

In addition to analyzing different flight portions, results were obtained when:

1) Different filters were used on the data. (Low pass filter, Spencer filter, moving average filter and no filter)
2) Different measurements were filtered. In some cases, a_x, a_z & q only were filtered. In other cases, a_x, a_z, q & α were filtered.
3) Different angle of attack estimation was used.
4) Two more stability and control derivatives were estimated. $C_{L_{de}}$ & C_{L_q}.

[6] Both sets of criteria were defined in Chapter 9.

It was observed that:

1) Filtering the data to remove noise yielded much more reasonable results. Without filtering, unacceptable results were obtained. This can be seen in Sections 11.2.1 and 11.2.2.
2) Filtering a_x, a_z & q but not α measurements yielded more reasonable results for C_{L_α}. This can be seen in Sections 11.2.1 and 11.2.2.
3) Results from the low pass filter and Spencer filter had much closer agreement with each other than the results from the moving average filter. This can be seen throughout the thesis results.
4) The moving average filter may be falsifying the aircraft dynamics. This was seen in the C_{m_α}, C_{m_q} & $C_{m_{de}}$ results in Sections 11.2.2 and 11.3. The estimated derivatives were smaller than expected and/or had improper signs repeatedly. This agrees with the discussion in Section 7.2 where it was mentioned that the moving average filter may falsify the aircraft dynamics. Basis for that claim was that the filter changed the magnitude of low frequencies when applied to a signal.
5) The EKF results were reasonable in many cases. They lie in expected ranges presented in Section 11.1.3.
6) There is very noticeable inconsistency in the EKF results. Using different flight portions yields widely varying derivative results. This can be seen clearly in Section 11.6 and throughout the thesis results.
7) The inconsistency is reduced for flight portions from the same flight, but it is still significant. This can be seen clearly in Section 11.6 and throughout the thesis results.

Overall, the EKF estimates, were reasonable in several cases. However, the estimates from different flight portions, have considerable inconsistency. Chapter 12 discusses several reasons for this inconsistency.

12 Discussion of Inconsistency in system Identification results

As seen in the EKF results and summarized in Section 11.7, there was significant inconsistency in system identification results. Using different flight portions yielded varying stability and control derivative estimates. This chapter focuses on discussing several sources that are resulting in this inconsistency. The different sources would have varying levels of how much they affect the results and cause inconsistency. Much of the discussion presented in this section is also applicable to UAS system identification in general not just for the SkyHunter.

12.1 The airframe

The SkyHunter is a **very light aircraft**. It weighs only 8-10 pounds. Thus, during flight, it is very **susceptible to disturbances** due to wind and wind gusts. This in turn affects the consistency of system identification results. It also makes it hard for pilots to fly the aircraft close to the desired trim condition (or according to the desired maneuvers). This issue is made worse since the SkyHunter flies at low at altitudes. Atmospheric disturbances are known to be high in low altitudes.

Command of the SkyHunter is also performed with the pilot on the ground. The pilot flies the aircraft based on their vision. They cannot sense any of the aircraft accelerations or rotations. This makes it even harder to fly the SkyHunter in steady flight conditions or according to specific flight maneuvers.

The SkyHunter is a small aircraft. **Proximity of aircraft components** causes them to have an influence on the aerodynamics of each other. For example, the wing would have an effect on the horizontal tail aerodynamics. The propeller slip stream would also have an effect on the horizontal tail. This is especially the case for the SkyHunter where the aircraft uses a pusher propulsion configuration with the propeller being directly in front of the empennage. As a result,

the propeller slip stream “blows” at the empennage. As a result of that, the horizontal tail performance is affected. This is discussed in more detail in Chapter 14.

Additionally, the SkyHunter airframe is prone to **aeroelasticity effects** especially at the empennage area. During flight, it was observed that the horizontal tail and vertical tail can oscillate. This would cause some variation in the aerodynamics of the empennage. As a result, aerodynamics of the aircraft as a whole would change to some degree. Thereby affecting system identification results.

12.2Unsteady Aerodynamics

An important factor affecting the consistency of system identification is **unsteady aerodynamics**. One way to quantify unsteadiness in aircraft dynamics is to calculate the reduced frequency. This was done and is presented in Chapter 13. If the reduced frequency is above 0.04, this is an indicator of unsteady aerodynamics. It is shown in Chapter 13 that the reduced frequency was higher than 0.04 in several flight portions. Thus, this is an indicator that the SkyHunter was encountering unsteady aerodynamics. The unsteady aerodynamics would cause the aircraft derivatives to vary with time. Therefore, making the EKF yield different results for different flight portions. The work is Chapter 14 also addresses unsteady aerodynamics.

12.3Nonlinear aerodynamics

Another important factor affecting the inconsistency is nonlinear aerodynamics, the EKF algorithm used in this thesis is not capable of capturing some of the non-linear aerodynamics. This is due to two reasons:

- First, the equations of motion used in the EKF are **simplified equations of motion**. This can be seen in Chapter 2. These equations cannot capture all actual aircraft dynamics. The equations have been decoupled from lateral aircraft motion states. In actual flight

lateral motion variables affect aircraft longitudinal motion. Also, the equations are used to estimate a limited number of derivatives. Therefore, the equations are suitable for analyzing specific flights. To have an algorithm that is suitable for analyzing more flights less simplifications should be made to the equations of motion. This may come at some cost of added complexity and possibly issues related to inability to identify a larger number of parameters.

- Second, the Extended Kalman Filter has some error due to depending on a **first order linearization** during the calculation of Jacobeans in Eq 5-22 and Eq 5-27. Some of the nonlinear dynamic are lost in these steps.

12.4Noise in sensors

The sensors used in this thesis, as for many UASs, are low cost sensors as discussed in Section 3.2. Their cost is close to 174 USD as estimated in Table 3-3. Thus, they are prone to have low accuracy and **high noise to signal ratio**. This in turn has major effect on system identification results which are based of the sensor data. The high noise in the sensor data is discussed in Chapter 7. Attempts were made to filter noise as mentioned in the previous chapters. However, noise still exists in the data. Moreover, low frequency noise is hard, or even impossible, to be filtered out since if we filter it, we corrupt the aircraft dynamics that lie in these low frequencies as well.

12.5Other sources of error

Since this work is based on experiments, several other factors can be causing inconsistency in the results. Examples of these errors are: improperly calibrated sensors, errors in data logging, time delays in logged data, inconsistency in flight preparation procedures, etc.

13 Calculation of reduced frequency

As mentioned in Section 12.2, one important source of inconsistency in the EKF results is unsteady aerodynamics. The presence of unsteady aerodynamics would cause the derivatives to vary with time. Thus, the estimation obtained using different flight portions would be inconsistent. One way to quantify unsteady aerodynamics is through the calculation of reduced frequency [36], [37]. Calculation of reduced frequency for Flight B of the SkyHunter is presented in this Chapter.

13.1 Calculation Methodology

For longitudinal motion, the reduced frequency can be calculated using the time history of the angle of attack (α). This is done as explained in the following paragraphs. The methodology is based on Reference [36].

The first step in the process, is to fit a sinusoidal curve to the angle of attack time history. This is done in a piecewise manner. I.e. a sinusoidal curve is fitted to every 21 data points. Fitting the data points to a sinusoidal curve is done using optimization. The goal of optimization would be to take the 21 data points and obtain a curve that first them a has the following form.

$$\alpha(t) = \bar{\alpha} + \Delta\alpha \cos(\omega t + \psi) \qquad \text{Eq 13-1}$$

$$\dot{\alpha}(t) = -\Delta\alpha\omega \sin(\omega t + \psi) \qquad \text{Eq 13-2}$$

The equations describe sinusoidal curves for the angle of attack, α, and its derivative, $\dot{\alpha}$. In these equations, $\bar{\alpha}$ is the mean angle of attack around which the sinusoidal curve, $\alpha(t)$, oscillates. $\Delta\alpha$ is the magnitude with which the sinusoidal curve oscillates. ω and ψ are the oscillation frequency and phase shift. Note: the number 21 was chosen to be similar to Reference [36], which uses 20 points. In this thesis, 21 points were chosen to have a symmetric number of points before and after the current data point.

The angle of attack is available in flight data. The angle of attack derivative can be calculated using numerical differentiation. Thus, these variables are known. Time steps, t, are also known. The purpose of optimization is to calculate the terms $\bar{\alpha}, \Delta\alpha, \omega$ and ψ. Optimization was perfumed using MATLAB function "lsqnonlin" which is part of the MATLAB Optimization toolbox[38]. The function was set to use Levenberg-Marquardt method for optimization.

After obtaining these four quantities the reduced frequency, k_1, can be calculated using the following equation.

$$k_{1_i} = \frac{\omega_i \bar{c}}{2V_i} \qquad \text{Eq 13-3}$$

In the equation, $\bar{c}$ is the wing mean geometric chord and V is the airspeed. The subscript i stands for the ith time instant.

13.2 Testing Optimization on a simplified made-up data

This section presents some made-up angle of attack data and shows the reduced frequency for this data. The main goal of making the calculations presented in this section was to verify that the developed code works properly. Since this section uses simulated data, we know the correct answers and thus can verify that the code works properly. In flight data, we would not know the correct answers.

The made-up angle of attack data was created by assuming values for the parameters $\bar{\alpha}, \Delta\alpha, \omega$ and ψ. Then, using Eq 13-1 and Eq 13-2, 50 seconds of data were generated. The data was generated at time steps of 0.05 s. This matches the SkyHunter sampling rate (20 Hz). Assuming that, $\bar{\alpha} = 3°$, $\Delta\alpha = 1°$, $\omega = 4.2\ rad/s$ and $\psi = 0°$, the angle of attack and angle of attack derivative time histories shown in the following figure were obtained.

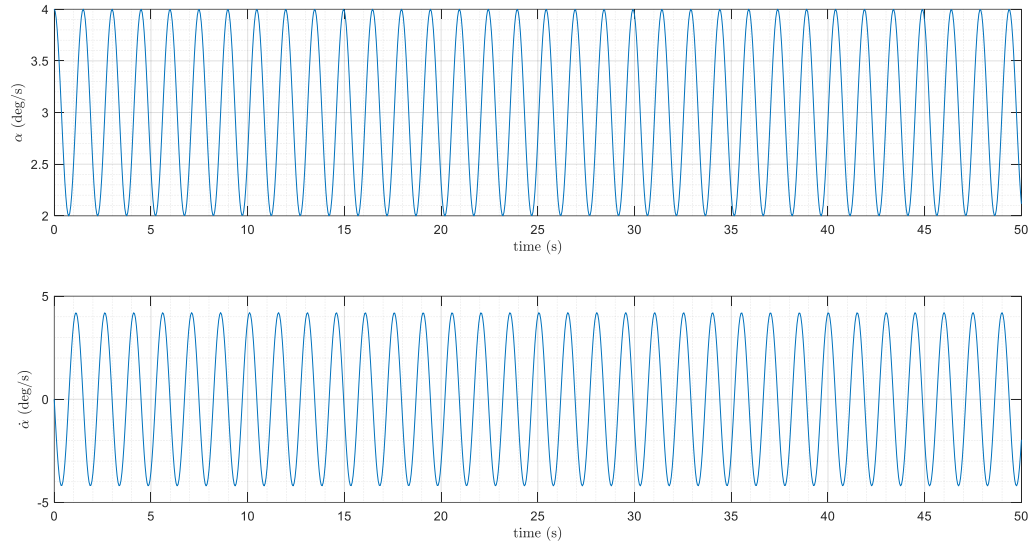

Figure 13-1: Made-up α & $\dot{\alpha}$ time histories.

The following figure shows the ω obtained using least squares optimization. It can be seen that the optimization worked properly to obtain $\omega = 4.2\, rad/s$ for the majority of the time history. There were a few portions where the optimization failed though. This was regarded as acceptable.

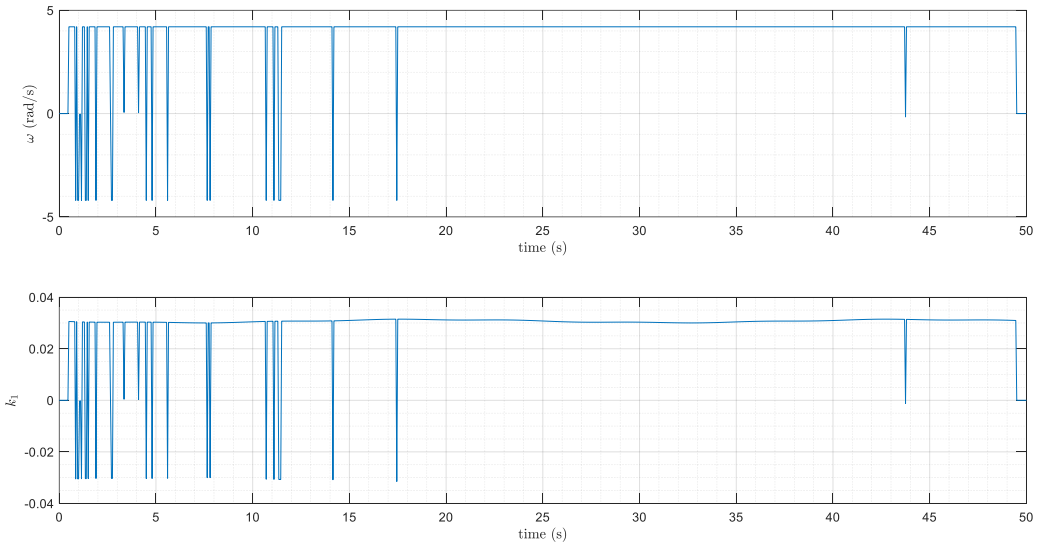

Figure 13-2: Calculated ω & k_1 for the made-up data.

The reduced frequency plot is presented in the previous figure. It was calculated using the mean geometric chord of the SkyHunter ($\bar{c} = 0.7317\ ft$). A made-up airspeed time history was also created and used to calculate the reduced frequency. The made-up airspeed has a mean value of 50 ft/s. It also has two sinusoidal curves superimposed to that value in order to have some variation. Thus, the equation used to create an airspeed time history was:

$$V(t) = 50 + 0.25\sin(t) + \sin(t/4) \qquad \text{Eq 13-4}$$

13.2.1 Adding noise to the made-up angle of attack time history

To further test the capability of the optimization, some noise was added to the made-up angle of attack and angle of attack derivative time histories. The added noise was chosen to be a random sinusoidal noise with frequency similar to that of an engine with rotation speed of 7260 rpm (121 Hz). The magnitude of the noise was set to be 20% of $\Delta\alpha$. The time histories of the created α and $\dot{\alpha}$ signals with the added noise are presented in the following figure. The figure also presents the no noise α and $\dot{\alpha}$ signals and presents the noise individually.

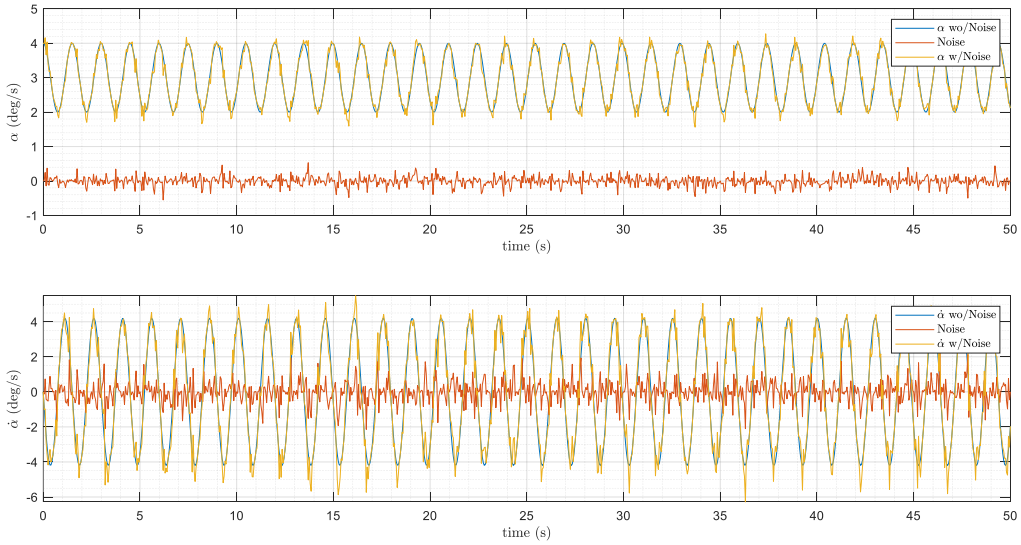

Figure 13-3: Made-up α & $\dot{\alpha}$ signals with added sinusoidal random noise.

The optimization results for the signals with added noise are presented in the following figure. It can be seen that the optimization again worked well in estimating the known ω except for a few instances. The fact that the estimated ω is not exactly 4.2 is expected since the addition of noise changed the original signal. The reduced frequency, k_1, is also plotted in the figure.

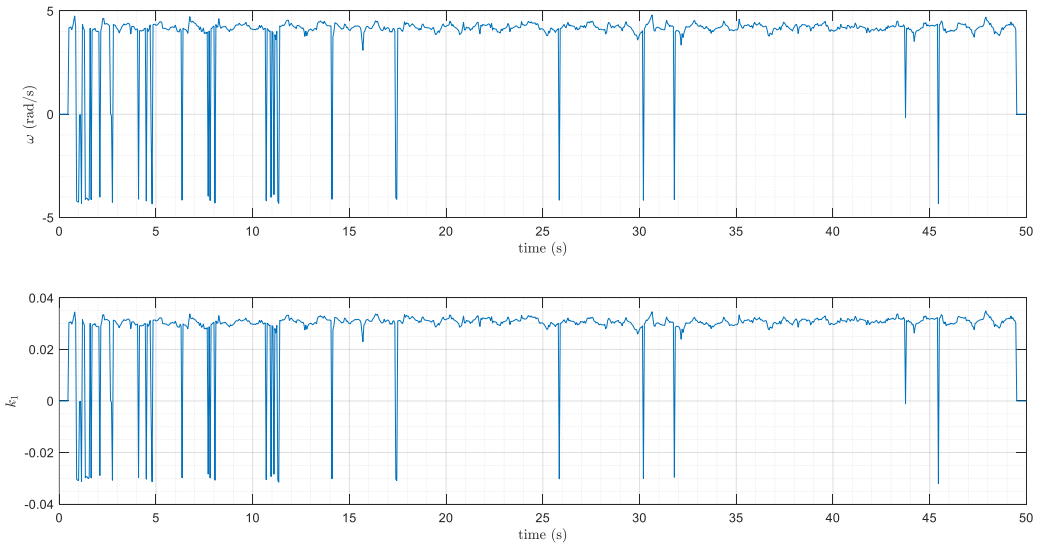

Figure 13-4: Calculated ω & k_1 for the made-up signals with added noise.

13.3Reduced Frequency for SkyHunter

Having verified that the optimization works well, the reduced frequency was calculated for one of the SkyHunter flights. The following figure shows the plot of the reduced frequency. A maximum value of 0.18 is observed. The value is larger than 0.04 for several time instances. This is an indicator that the SkyHunter was encountering unsteady aerodynamics, which would result in inconsistent system identification results.

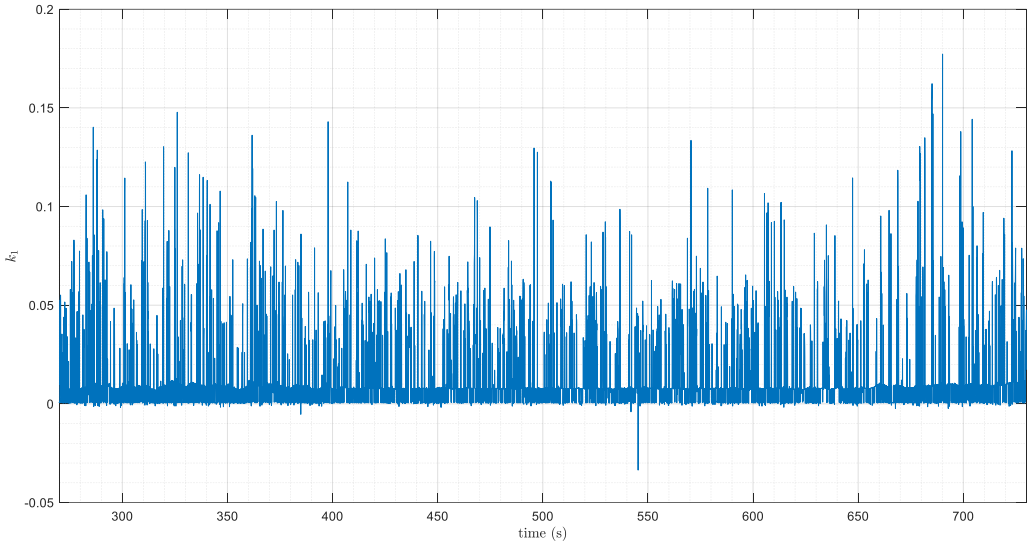

Figure 13-5: Reduced frequency plot for a SkyHunter Flight.

The following figure shows an enlarged view of the reduced frequency from t= 650s to t= 710s. The green portion is data that was used for system identification. It can be seen that the data contains several portions higher than 0.04. The data used for system identification also contains the highest peak in the flight, which is close to 0.18.

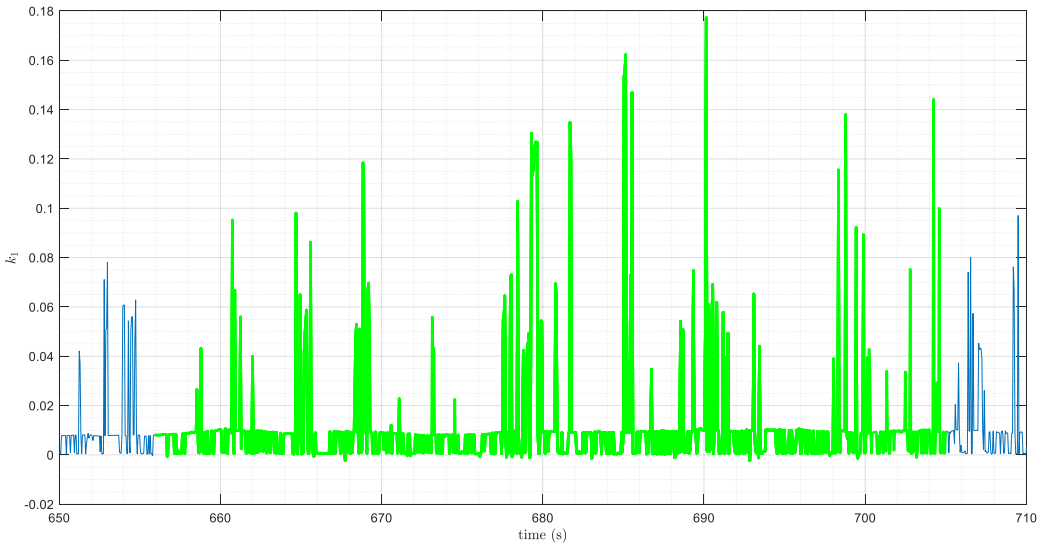

Figure 13-6: Reduced frequency plot for SkyHunter plot. A zoomed in view. Green portion is flight portion used in system identification.

The following sections show how the reduced frequency correlates with other flight data.

13.3.1 Correlation between k_1 and $\frac{\dot{\alpha}\bar{c}}{2V}$

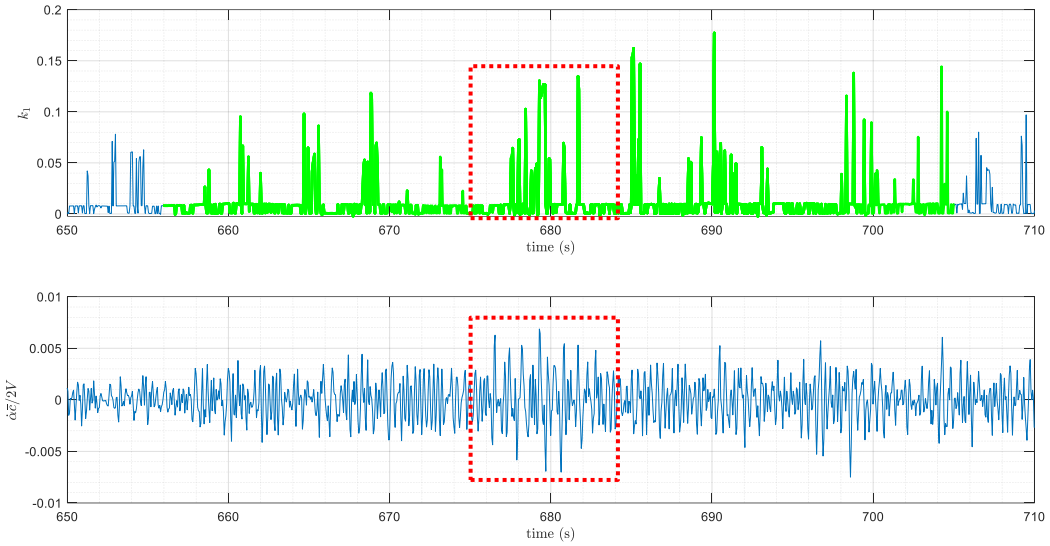

Figure 13-7: Correlation between reduced frequency and $\frac{\dot{\alpha}\bar{c}}{2V}$

Strong correlation between k_1 and $\frac{\dot{\alpha}\bar{c}}{2V}$ could not be observed. However, the middle section which is identified in the previous plots does show a region where large oscillations in $\frac{\dot{\alpha}\bar{c}}{2V}$ were related with large k_1.

13.3.2 Correlation between k_1 and rotation rates

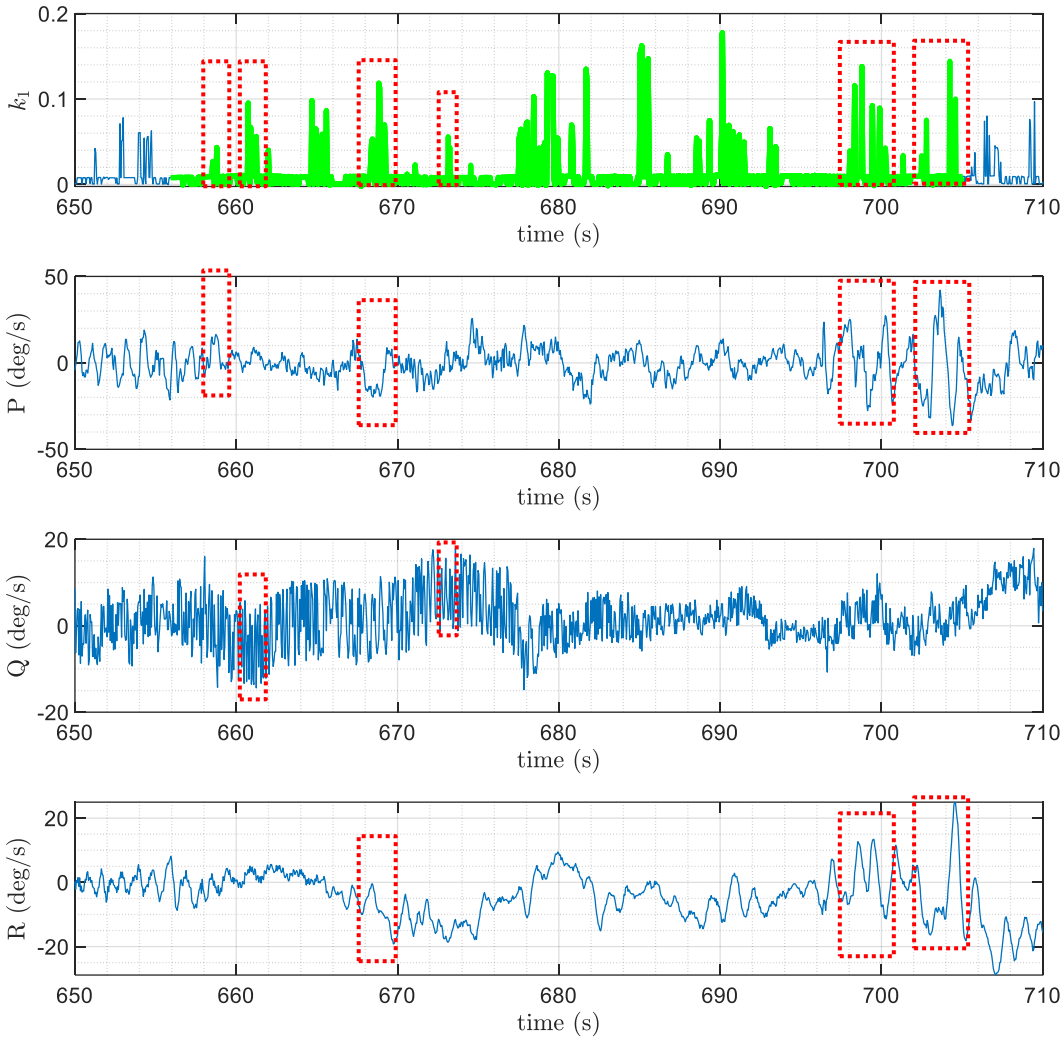

Figure 13-8: Correlation between reduced frequency and rotation rates.

There are several places where high roll and yaw rates were occurring at the same time the reduce frequency had a pike. The reduced frequency particularly had spikes when the roll/yaw rates were changing. Strong correlation between pitch rate and reduced frequency could not be observed. Perhaps, the strong noise in the pitch rate signal is making observation of a correlation difficult.

13.3.3 Correlation between k_1 and Euler angles

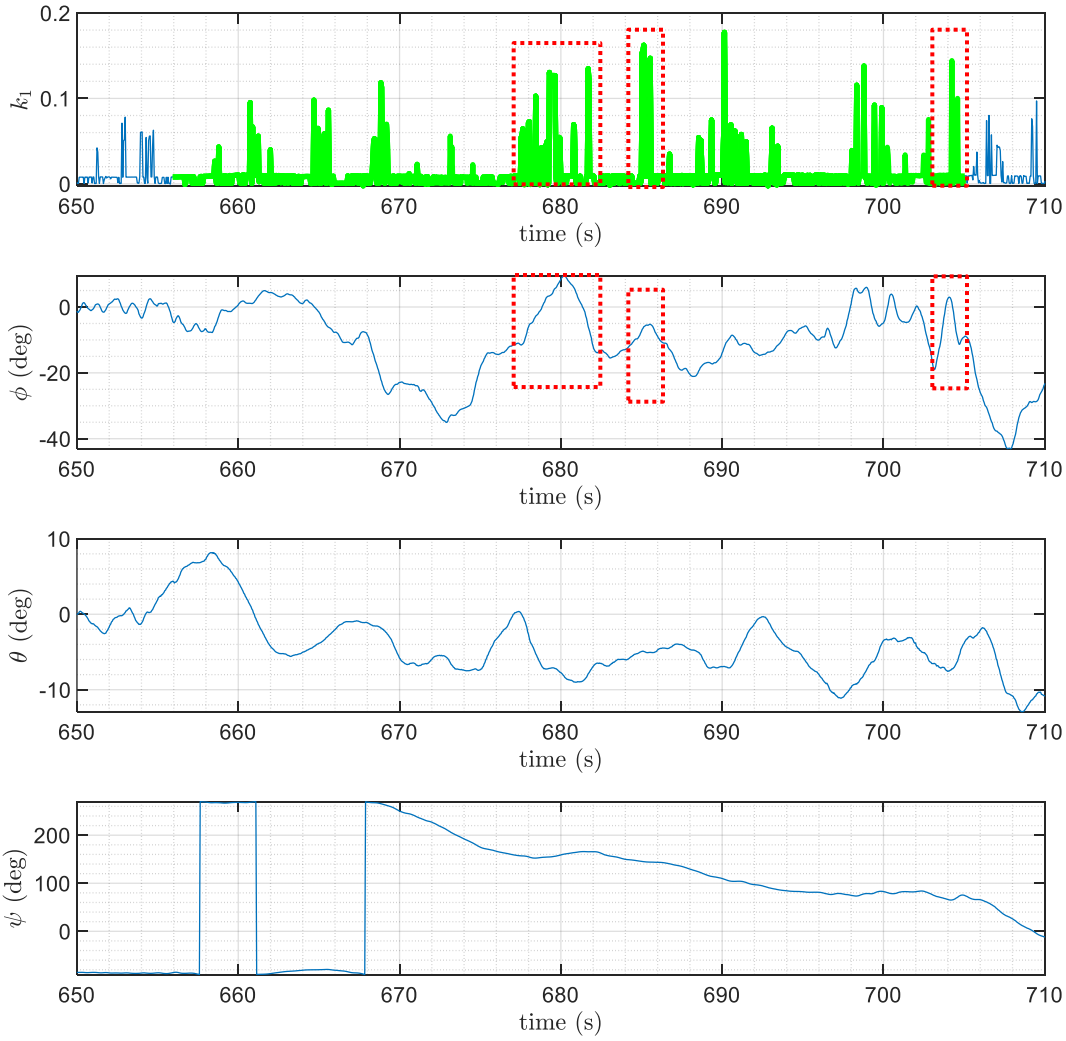

Figure 13-9: Correlation between reduced frequency and Euler Angles

In several locations, it was observed that when ϕ had a trend of going up then going down, the reduced frequency had an increased value. This can be observed in the identified regions in the previous figure. Correlation between θ or ψ and reduced frequency could not be observed.

14 Discussion of dynamic pressure and derivatives estimation

The theoretical methods of obtaining stability and control derivatives for an aircraft available in [3], [4] depend on the component buildup method. Meaning, that a derivative for an aircraft is estimated based on contributions from the different components of the aircraft. This results in the aircraft derivatives being dependent on the horizontal and vertical tail dynamic pressure ratios (η_h and η_v). For example, the aircraft lift curve slope, C_{L_α}, depends on contributions from the wing, fuselage, and horizontal tail as seen in the following equation. The equation shows that C_{L_α} depends on η_h.

$$C_{L_\alpha} = C_{L_{\alpha_{wf}}} + C_{L_{\alpha_h}} \boldsymbol{\eta_h} \frac{S_h}{S}\left(1 - \frac{d\epsilon}{d\alpha}\right) \quad \text{Eq 14-1}$$

In the equation, $C_{L_{\alpha_{wf}}}$ is the wing-fuselage contribution to the aircraft C_{L_α}, $C_{L_{\alpha_h}}$ is the horizontal tail lift curve slope, η_h is the horizontal tail dynamic pressure ratio. S_h and S are the horizontal tail and main wing planform areas respectively. $\frac{d\epsilon}{d\alpha}$ is the down wash gradient with respect to the angle of attack.

In a likewise manner, the dependence of other aircraft derivatives on η_h and η_v can be seen in Reference [3]. Some of the longitudinal derivatives that depend on η_h are presented below. Reference [3] can be consulted for details on the meaning of the different terms.

$$C_{L_0} = C_{L_{0_{wf}}} - C_{L_{\alpha_h}} \boldsymbol{\eta_h} \frac{S_h}{S} \epsilon_0 + C_{L_{0_h}} \quad \text{Eq 14-2}$$

$$C_{m_0} = C_{m_{ac_{wf}}} + C_{L_{0_{wf}}}\left(\bar{x}_{cg} - \bar{x}_{ac_{wf}}\right) + C_{L_{\alpha_h}} \boldsymbol{\eta_h} \frac{S_h}{S}\left(\bar{x}_{ac_h} - \bar{x}_{cg}\right)\epsilon_0 \quad \text{Eq 14-3}$$

$$C_{m_\alpha} = C_{L_{\alpha_{wf}}}\left(\bar{x}_{cg} - \bar{x}_{ac_{wf}}\right) - C_{L_{\alpha_h}} \boldsymbol{\eta_h} \frac{S_h}{S}\left(\bar{x}_{ac_h} - \bar{x}_{cg}\right)\left(1 - \frac{d\epsilon}{d\alpha}\right) \quad \text{Eq 14-4}$$

$$C_{m_{de}} = -C_{L_{\alpha_h}} \boldsymbol{\eta_h} \frac{S_h}{S}\left(\bar{x}_{ac_h} - \bar{x}_{cg}\right)\tau_e \quad \text{Eq 14-5}$$

If the dynamic pressure ratio changes during flight, this would mean that the stability and control derivatives would change as well. This would lead to some inconsistency in the system

identification results. Experimentation was made to measure η_h from flight data at different locations along the empennage. The results of this experimentation are presented in this chapter. Section 14.1 discusses the experiment setup and procedures. Section 14.2 then presents the experiment results. Section 14.3 makes a comparison between results obtained from this experiment and another experiment performed using CFD. It was observed that the results from these two experiments agreed. Finally, Section 14.4, discusses the relevance of the experiment results to the system identification results.

14.1Experiment setup and procedure

The SkyHunter was equipped with two pitot-static tubes for experiments in this Chapter. One was placed at the conventional nose location to measure free stream conditions. The other one was placed either at the horizontal or the vertical tail. This allowed measurement of freestream air speed as well as air speed at the horizontal or vertical tail. Thus, the dynamic pressure ratio at the horizontal or vertical tail could be easily calculated using:

$$\eta_h = \frac{\frac{1}{2}\rho V_h^2}{\frac{1}{2}\rho V^2} = \frac{V_h^2}{V^2} \qquad \text{Eq 14-6}$$

$$\eta_v = \frac{\frac{1}{2}\rho V_v^2}{\frac{1}{2}\rho V^2} = \frac{V_v^2}{V^2} \qquad \text{Eq 14-7}$$

With the current electronics and software on board the SkyHunter, it was only possible to install 2 pitot tubes on the SkyHunter. However, it was desired to obtain dynamic pressure measurements at different locations on the empennage. Therefore, several flights were made, and the location of the empennage pitot tube was changed from flight to flight. The following diagram shows where the empennage pitot tube was placed during the different flights. Figure 14-2 and Figure 14-3 show the SkyHunter equipped with both pitot tubes.

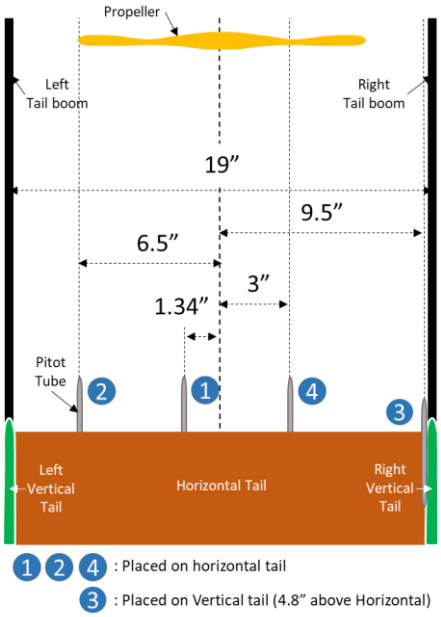

Figure 14-1 Diagram showing location of Empennage Pitot tube during different flights

Figure 14-2: SkyHunter Equipped with two pitot tubes: One at nose, One on vertical tail.

Figure 14-3:SkyHunter Equipped with two pitot tubes: One at nose, One on vertical tail. (Side View)

The procedures of the experiment were simple. The pilot took-off then flew the aircraft in a racetrack to collect data with the aircraft flying in different headings. Then the pilot landed. Flying in different headings would help in reducing the effect of a prevailing wind in the measured airspeeds. The prevailing wind would be averaged out since some flight portions will encounter head wind while others would encounter tail wind.

14.2 Experiment results

The following figures show the measured airspeed from the nose and tail pitot tubes as well as the dynamic pressure ratio. The figures show the data collected when the empennage pitot tube was placed at different locations as specified in Figure 14-1.

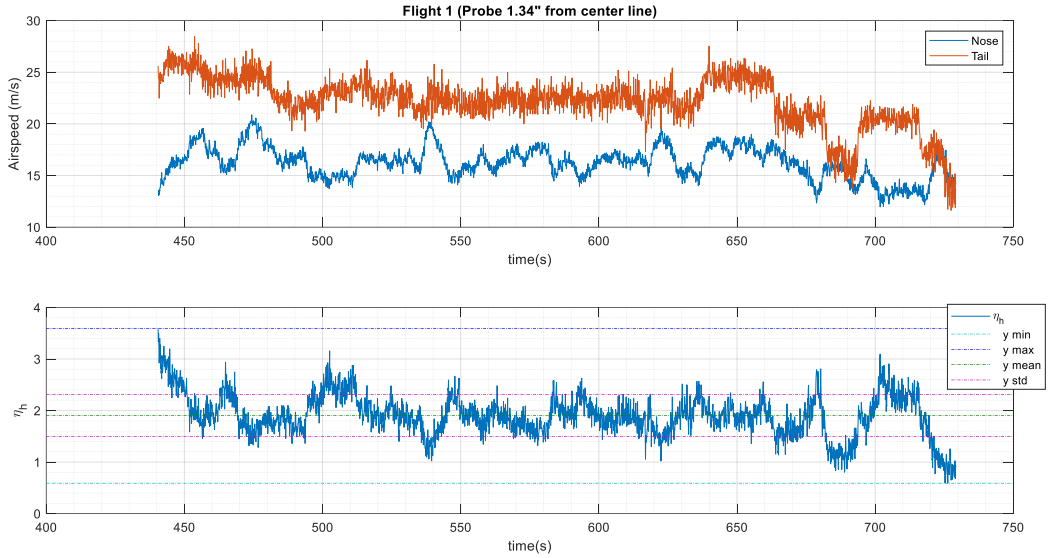

Figure 14-4: Data from first flight. $\eta_{avg} = 1.9, std.div. = 0.41$

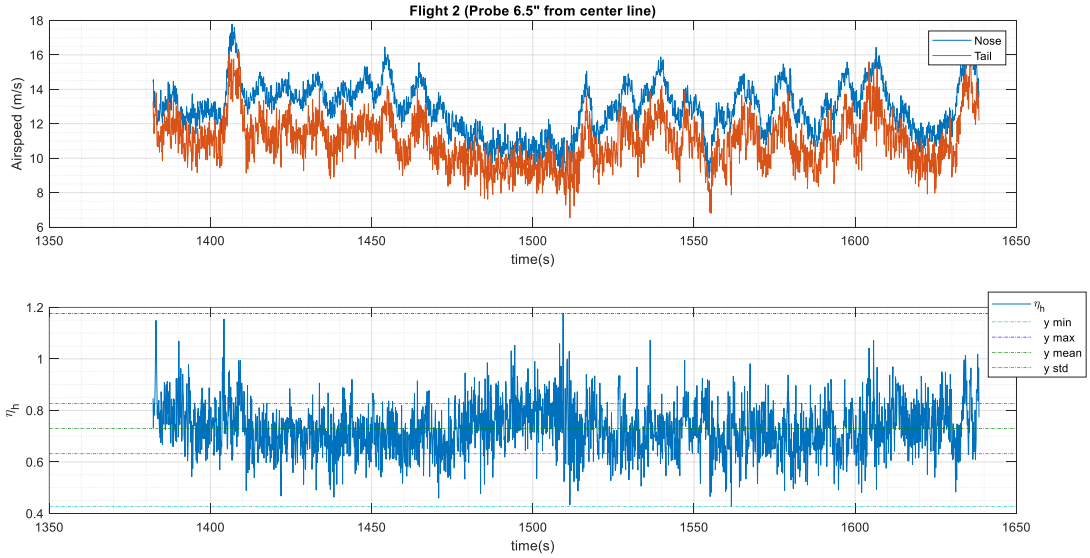

Figure 14-5: Data from second flight. $\eta_{avg} = 0.73, std.div. = 0.098$

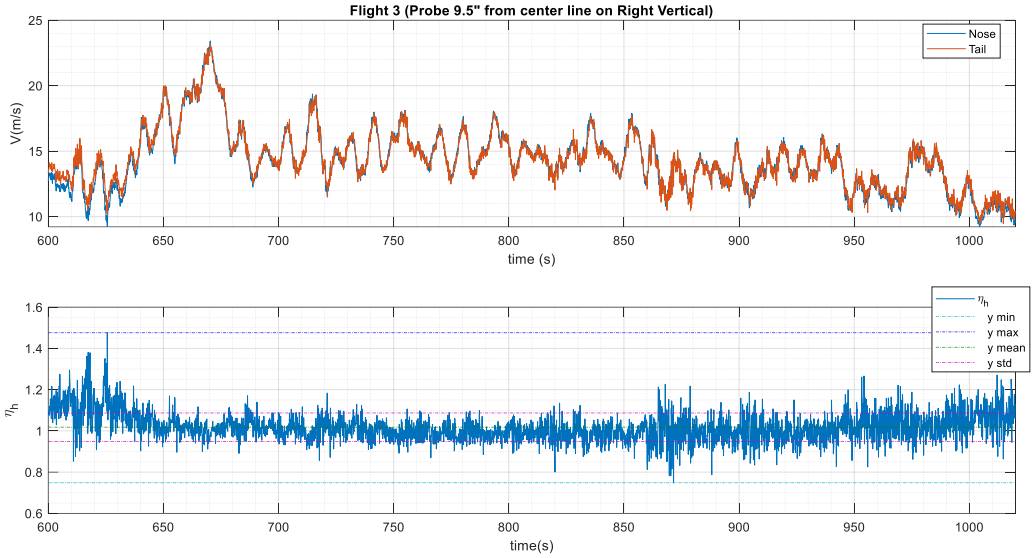

Figure 14-6: Data from third flight. $\eta_{avg} = 1.02, std.div. = 0.0687$

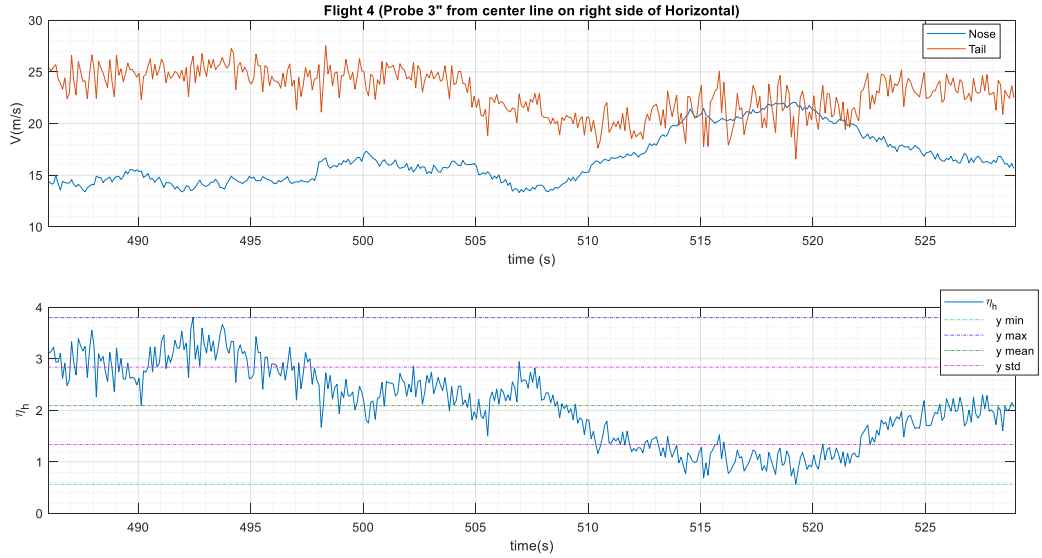

Figure 14-7: Data from fourth flight. $\eta_{avg} = 2.09, std.div. = 0.75$

It can be clearly seen that the dynamic pressure ratio varies considerably during flight. For example, Figure 14-4 for the first flight shows that the dynamic pressure ratio had a minimum value of 0.59 and a maximum value of 3.59. The average value was 1.9 and the

standard deviation was 0.41. This variation may result in a change in the stability and control derivatives to some extent.

It can also be observed that the dynamic pressure ratio varies depending on the location along the horizontal tail. This can be seen easily in the following table which summarizes some statistics obtained from the four flights.

Table 14-1: Summary of dynamic pressure experiment results

Quantity	V_{nose} (m/s)		V_{tail} (m/s)		η_h				**Pitot location from center line (in)**
Statistic	Mean	Std. div.	Mean	Std. div.	Mean	Std. div.	Min	Max	~
Flight 1	16.24	1.537	22.16	2.456	**1.9**	0.41	0.59	3.59	1.34 (left)
Flight 2	12.92	1.48	11	1.417	**0.73**	0.098	0.43	1.18	6.5 (left)
Flight 3	14.30	2.31	14.39	2.20	**1.02**	0.0687	0.75	1.48	9.5 (right vertical)
Flight 4	16.60	2.46	22.99	2.12	**2.09**	0.75	0.57	3.80	3 (right)

The following figure shows how the dynamic pressure changes with pitot tube location. It can be seen that the dynamic pressure is higher closer to the center. However, it is not possible to make a claim about the distribution of dynamic pressure over the horizontal tail. This is due to three reasons: (1) Only four data points are used. (2) Two flights had the pitot tube on the left of the centerline and two flights had it on the right. The rotation of the propeller may result in different distributions on either side of the centerline. (3) One of the flights had the pitot tube located on the vertical tail 4.8” above the other three flights. A better study can be made if more data points are gathered on both sides of the center line and in several locations on the vertical tail. Despite these limitations however, the obtained results matched the observations of an investigation performed using CFD [18]. This is presented in the following section.

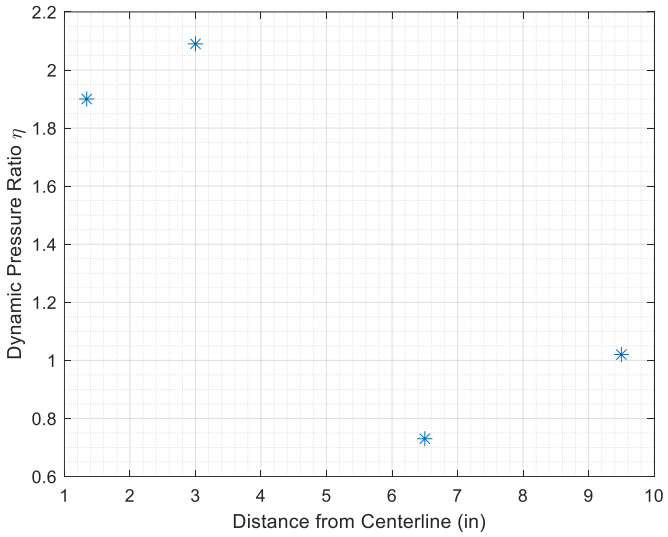

Figure 14-8: Average dynamic pressure at different locations along the horizontal tail

14.3Comparison of obtained results with another reference

In Reference [18], CFD simulations were performed on a 4m wing span UAS called the DG808s. This study is especially relevant to the SkyHunter since the DG808s has a similar propulsion system to the SkyHunter. The electric motor for both aircraft is placed directly in front of the horizontal tail. Thus, the propeller slipstream would be reaching the horizontal tail.

Figure 14-9: 4m wingspan version of the DG808s UAS used in Reference [18]

In one of the CFD simulations, 22 probes were placed at 22 equidistant sections along the span of the horizontal tail. The probes were used to measure axial velocity magnitude. The

observed axial velocity distribution plot is reproduced in the following figure. It can be seen that the velocity measured closer to the center of the horizontal tail is higher than that at the tip. This is similar to the observation presented in Figure 14-8 for the SkyHunter.

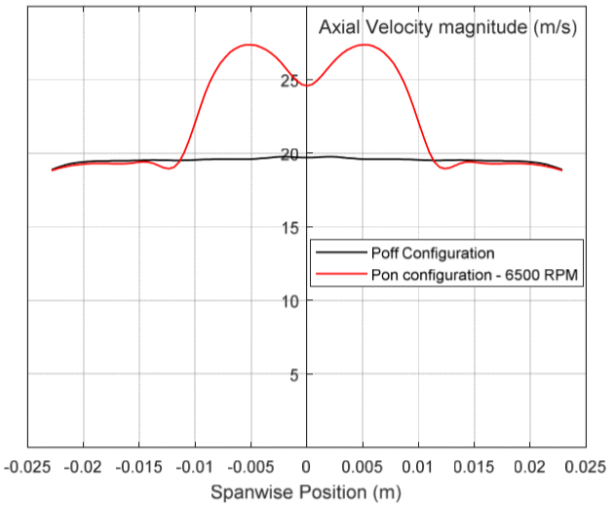

Figure 14-10: CFD results of the velocity distribution along the horizontal tail of the DG808s. Results given for power on and power off conditions. Reference [18]

14.4Relevance of results in relation to system identification

It was observed that the dynamic pressure ratio is constantly changing during flight. Many reasons can result in these changes. One of the likely reasons is changes in throttle. When the throttle changes the propeller slip stream would likely affect the horizontal tail aerodynamics differently. Such change in aerodynamics would result in a change in the aircraft derivatives. Thus, different flight portions would have different derivatives as it is observed in this thesis.

Also, it was observed that the horizontal tail dynamic pressure ratio changes along the span of the horizontal tail. This would result in different aerodynamic forces along the span of the horizontal tail. Since the SkyHunter tail is made out of foam, the variation in force along the span may cause aeroelasticity. In fact, aeroelasticity has been observed at the horizontal tail. Aeroelasticity would change the aerodynamics of the horizontal tail and therefore the aircraft, leading to inconsistency in the system identification results.

15 Conclusions

The following can be concluded:

1) In this thesis, the classical approach to system identification that has been used over the past 40-50 years on manned aircraft was applied to the SkyHunter UAS. Data was analyzed from three different flights. Several portions from each of the flights were analyzed.
2) Reasonable stability and control derivatives were obtained in several cases.
3) However, depending on which flight portion was used in system identification, the obtained results varied widely (i.e. showed inconsistency.)
4) Several reasons for this inconsistency were identified and are listed below. Much of the discussion in the list is applicable to UAS system identification in general not just the SkyHunter.
    a. Unsteady aerodynamics. It was shown that the reduced frequency was higher than 0.04 at several time instances in the flight data. This is an indicator that the SkyHunter was encountering unsteady aerodynamics, which would result in inconsistency in the EKF results.
    b. Since the SkyHunter is small, compared to full sized aircraft, its components are in close proximity. Therefore, the aerodynamics of the aircraft components are affected by neighboring ones, in a possibly different way than full sized aircraft. For example, the location of the propeller in front of the empennage is changing the aerodynamics of the horizontal and vertical tails. Flying at different throttle levels likely results in different aerodynamics at the empennage. Thus, affecting the aerodynamics of the aircraft as a whole.

c. The SkyHunter aircraft is very light. Therefore, it is susceptible to atmospheric disturbances, which are particularly high in the low altitudes that the SkyHunter flies at.

d. High noise in sensor measurements. The SkyHunter uses low cost sensors. Although filtering is applied, there still remains low frequency noise, some unfiltered high frequency noise and sensor inaccuracies in the data.

e. The EKF algorithm may not be capable of capturing the aircraft dynamics properly since it is using simplified equations of motion. Effort has been made to use flight data that satisfy the simplifying assumptions of the equations. However, the lateral-directional motion variables are still present in the flight data (i.e. p, r, ϕ & β are not zero) and are likely affecting the dynamics.

f. The EKF algorithm uses first order linearization in two calculations at every time stamp. Non-linear aerodynamics are therefore lost in these steps.

5) Filtering the flight data from high frequency noise improved the consistency of the EKF results noticeably. Before filtering, the results varied dramatically from each other and, in many cases, did not make sense.

16 Recommendations

The following is recommended:

1) Repeating the same work done in this thesis, with the same sensors, but using a larger and heavier UAS. The larger aircraft would preferably have the same configuration as the SkyHunter. Especially have the propeller directly in front of the empennage like the SkyHunter. This recommendation aims at reducing the susceptibility to external disturbance by increasing the mass of the aircraft. The same sensors are used to maintain similar sensor noise level. This can help at evaluating how much external disturbances are contributing to the inconsistency is EKF results.
2) Repeating the same work on the SkyHunter but using high cost sensors. This recommendation aims at reducing the effect of sensor noise on the EKF results. Comparison can then be made to see how much the sensor noise contributed to the inconsistency in system identification results observed in this thesis.
3) Exploring the use of less simplified equations of motion. This way more of the aircraft dynamics are captured by the equations. Adding lateral-directional motion variables can be done by just using their measured values while running the EKF. This would be simpler than adding them as states and having to estimate longitudinal and lateral-directional motion simultaneously.
4) Using higher order versions of the EKF can be explored.
5) Flying the SkyHunter in specially designed system identification maneuvers such as the ones presented in Chapter 4. Special attention would be needed however on how to apply such maneuvers since their timing is very difficult for a human pilot to achieve with repeatability.

6) Increasing pilot situational awareness of the UAS (i.e. find tools that allow the pilot to sense the aircraft accelerations and rotations.) This can increase the pilot's ability to fly the aircraft in steady level flight and according to desired maneuvers. Using first person view (FPV) or using wearable technology that vibrate or make sounds are possible ideas for increasing the situational awareness.

17 References

[1] G. H. Bryan, *Stability in aviation*. London: Macmillan and Co., 1911.

[2] P. G. Hamel and R. V. Jategaonkar, "Evolution of flight vehicle system identification," *Journal of Aircraft*, vol. 33, no. 1, pp. 9–28, Jan. 1996.

[3] J. Roskam, *Airplane flight dynamics and automatic flight controls*. Lawrence, KS: DARcorporation, 2011.

[4] M. R. Napolitano, *Aircraft dynamics: from modeling to simulation*. Hoboken, NJ: J. Wiley, 2012.

[5] R. D. Finck, "USAF (United States Air Force) Stability and Control DATCOM (Data Compendium)," MCDONNELL AIRCRAFT CO ST LOUIS MO, Apr. 1978.

[6] *Advanced Aircraft Analysis (AAA)*. DARcorporation, http://www.darcorp.com/Software/AAA/.

[7] "AVL." [Online]. Available: http://web.mit.edu/drela/Public/web/avl/. [Accessed: 04-Jan-2019].

[8] R. V. Jategaonkar, *Flight vehicle system identification: a time-domain methodology*, Second edition. Reston, Va: AIAA, American Institute of Aeronautics and Astronautics, 2015.

[9] V. Klein and E. A. Morelli, *Aircraft system identification: theory and practice*. Reston, VA: American Institute of Aeronautics and Astronautics, 2006.

[10] E. A. Morelli and V. Klein, *Aircraft system identification: theory and practice*. Williamsburg, VA: Sunflyte Enterprises, 2016.

[11] M. B. Tischler and R. K. Remple, *Aircraft and rotorcraft system identification: engineering methods with flight test examples*, 2nd ed. Reston, VA: American Institute of Aeronautics and Astronautics, 2012.

[12] R. E. Maine and K. W. Iliff, "Application of parameter estimation to aircraft stability and control: The output-error approach - NASA-RP-1168," Jun. 1986.

[13] M. R. Napolitano and J. M. Spagnuolo, "Determination of the stability and control derivatives of the NASA F/A-18 HARV using flight data," NASA-CR-194838, Dec. 1993.

[14] N. V. Hoffer, C. Coopmans, A. M. Jensen, and Y. Chen, "Small low-cost unmanned aerial vehicle system identification: A survey and categorization," in *2013 International Conference on Unmanned Aircraft Systems (ICUAS)*, 2013, pp. 897–904.

[15] A. G. Kallapur, S. S. Ali, and S. G. Anavatti, "Application of Extended Kalman Filter Towards UAV Identification," in *Autonomous Robots and Agents*, vol. 76, S. C. Mukhopadhyay and G. S. Gupta, Eds. Berlin, Heidelberg: Springer Berlin Heidelberg, 2007, pp. 199–207.

[16] S. Brunke and M. Campbell, "Estimation architecture for future autonomous vehicles," in *Proceedings of the 2002 American Control Conference (IEEE Cat. No.CH37301)*, 2002, vol. 2, pp. 1108–1114 vol.2.

[17] J. Evans, G. Elkaim, S. Lo, and B. Parkinson, "System Identification of an Autonomous Aircraft using GPS," in *Proceedings of the 10th International Technical Meeting of the Satellite Division of The Institute of Navigation (ION GPS 1997)*, Kansas City, MO, 1997, pp. 1065–1071.

[18] Y. Chandra, "Investigation of the Aerodynamic Performance of a DG808s UAS in Propeller Slipstream Using Computational Fluid Dynamics," M.S. Thesis, University of Kansas, United States -- Kansas, 2017.

[19] R. F. Stengel, *Flight dynamics*. Princeton, NJ: Princeton University Press, 2004.

[20] "Pixhawk 1 · PX4 User Guide." [Online]. Available: https://docs.px4.io/en/flight_controller/pixhawk.html. [Accessed: 14-Oct-2018].

[21] E. A. Morelli, "Estimating noise characteristics from flight test data using optimal Fourier smoothing," *Journal of Aircraft*, vol. 32, no. 4, pp. 689–695, Jul. 1995.

[22] DARcorporation, "AAA Physics-Based Methods." [Online]. Available: http://www.darcorp.com/Software/AAA/Physics-Based/. [Accessed: 06-Nov-2018].

[23] "GOE 438 AIRFOIL (goe438-il)." [Online]. Available: http://airfoiltools.com/airfoil/details?airfoil=goe438-il. [Accessed: 11-Jan-2019].

[24] "WASP (smoothed) (waspsm-il)." [Online]. Available: http://airfoiltools.com/airfoil/details?airfoil=waspsm-il. [Accessed: 11-Jan-2019].

[25] "NACA M5 AIRFOIL (m5-il)." [Online]. Available: http://airfoiltools.com/airfoil/details?airfoil=m5-il. [Accessed: 11-Jan-2019].
[26] "Airfoil Tools." [Online]. Available: http://airfoiltools.com/.
[27] "CLARK Y AIRFOIL (clarky-il)." [Online]. Available: http://airfoiltools.com/airfoil/details?airfoil=clarky-il. [Accessed: 11-Jan-2019].
[28] E. Plaetschke and G. Schulz, "Practical input signal design," *AGARD Lecture Series*, vol. 104, 1979.
[29] J. Spencer, "On the Graduation of the Rates of Sickness and Mortality Presented by the Experience of the Manchester Unity of Oddfellows during the period 1893-97," *Journal of the Institute of Actuaries (1886-1994)*, vol. 38, no. 4, pp. 334–343, 1904.
[30] J. Spencer, "Some Illustrations of the Employment of Summation Formulas in the Graduation of Mortality Tables," *Journal of the Institute of Actuaries (1886-1994)*, vol. 41, no. 3, pp. 361–408, 1907.
[31] *MATLAB Digital Filter Design*. MathWorks, https://www.mathworks.com/help/signal/filter-design.html.
[32] *MATLAB Signal Processing Toolbox*. MathWorks, https://www.mathworks.com/products/signal.html.
[33] E. Morelli, "Real-Time Aerodynamic Parameter Estimation Without Air Flow Angle Measurements," in *AIAA Atmospheric Flight Mechanics Conference*, Toronto, Ontario, Canada, 2010.
[34] H. Fang, N. Tian, Y. Wang, M. Zhou, and M. A. Haile, "Nonlinear Bayesian estimation: from Kalman filtering to a broader horizon," *IEEE/CAA Journal of Automatica Sinica*, vol. 5, no. 2, pp. 401–417, Mar. 2018.
[35] "University of Kansas, Aerospace engineering short courses."
[36] C.-T. E. Lan, S. Keshmiri, and R. Hale, "Fuzzy-Logic Modeling of a Rolling Unmanned Vehicle in Antarctica Wind Shear," *Journal of Guidance, Control, and Dynamics*, vol. 35, no. 5, pp. 1538–1547, Sep. 2012.
[37] R. L. Bisplinghoff, H. Ashley, and R. L. Halfman, *Aeroelasticity*, Dover ed. New York: Dover Publications, 1996.
[38] *MATLAB Optimization Toolbox*. MathWorks, https://www.mathworks.com/products/optimization.html.

18 Appendix A

To simplify the presentation in Chapter 2, some of the intermediate derivations are presented in this appendix.

18.1 Inserting the non-dimensional coefficients in the polar form of the equations of motion.

18.1.1 The $\dot{V}$ equation

Expanding Eq 2-80, and plugging Eq 2-83 to Eq 2-85 in it yields:

$$\begin{aligned}\dot{V} = \frac{\bar{q}SC_X}{m}cos\alpha cos\beta + \frac{\bar{q}SC_Z}{m}sin\alpha\, cos\beta + \frac{\bar{q}SC_Y}{m}sin\beta - gsin\Theta cos\alpha cos\beta \\ + gcos\Phi cos\Theta sin\alpha\, cos\beta + gsin\Phi cos\Theta sin\beta \\ + \frac{F_{T_X}cos\alpha cos\beta}{m} + \frac{F_{T_Y}}{m}sin\beta + \frac{F_{T_Z}}{m}sin\alpha\, cos\beta\end{aligned} \quad \text{Eq 18-1}$$

Regrouping the terms yields:

$$\begin{aligned}\dot{V} = \frac{\bar{q}S}{m}\left((C_X cos\alpha + C_Z sin\alpha)\, cos\beta + C_Y sin\beta\right) - gsin\Theta cos\alpha cos\beta \\ + gcos\Phi cos\Theta sin\alpha\, cos\beta + gsin\Phi cos\Theta sin\beta \\ + \frac{F_{T_X}cos\alpha cos\beta}{m} + \frac{F_{T_Y}}{m}sin\beta + \frac{F_{T_Z}}{m}sin\alpha\, cos\beta\end{aligned} \quad \text{Eq 18-2}$$

Using Eq 2-90 yields:

$$\begin{aligned}\dot{V} = \frac{\bar{q}S}{m}(-C_D\, cos\beta + C_Y sin\beta) - gsin\Theta cos\alpha cos\beta \\ + gcos\Phi cos\Theta sin\alpha\, cos\beta + gsin\Phi cos\Theta sin\beta \\ + \frac{F_{T_X}cos\alpha cos\beta}{m} + \frac{F_{T_Y}}{m}sin\beta + \frac{F_{T_Z}}{m}sin\alpha\, cos\beta\end{aligned} \quad \text{Eq 18-3}$$

Using Eq 2-91 yields

$$\begin{aligned}\dot{V} = -\frac{\bar{q}S}{m}C_{D_{wind}} - gsin\Theta cos\alpha cos\beta + gsin\Phi cos\Theta sin\beta \\ + gcos\Phi cos\Theta sin\alpha\, cos\beta + \frac{F_{T_X}}{m}cos\alpha cos\beta + \frac{F_{T_Y}}{m}sin\beta \\ + \frac{F_{T_Z}}{m}sin\alpha\, cos\beta\end{aligned} \quad \text{Eq 18-4}$$

18.1.2 The $\dot{\alpha}$ equation

Expanding Eq 2-81, and plugging Eq 2-83 to Eq 2-85 in it yields:

$$\dot{\alpha} = \frac{1}{Vcos\beta}\left(\frac{\bar{q}SC_Z}{m}cos\alpha + \frac{F_{T_Z}}{m}cos\alpha + gcos\Phi cos\Theta cos\alpha - \frac{\bar{q}SC_X}{m}sin\alpha - \frac{F_{T_X}}{m}sin\alpha + gsin\Theta sin\alpha\right) + q - tan\beta\,(p\,cos\alpha + r\,sin\alpha) \quad \text{Eq 18-5}$$

Rearranging the terms, we get:

$$\dot{\alpha} = \frac{1}{Vcos\beta}\left(\frac{\bar{q}S}{m}(C_Z cos\alpha - C_X sin\alpha) + gcos\Phi cos\Theta cos\alpha + gsin\Theta sin\alpha + \frac{F_{T_Z}}{m}cos\alpha - \frac{F_{T_X}}{m}sin\alpha\right) + q - tan\beta\,(p\,cos\alpha + r\,sin\alpha) \quad \text{Eq 18-6}$$

Using Eq 2-89, we get:

$$\dot{\alpha} = \frac{1}{Vcos\beta}\left(-\frac{\bar{q}S}{m}C_L + gcos\Phi cos\Theta cos\alpha + gsin\Theta sin\alpha + \frac{F_{T_Z}}{m}cos\alpha - \frac{F_{T_X}}{m}sin\alpha\right) + q - tan\beta\,(p\,cos\alpha + r\,sin\alpha) \quad \text{Eq 18-7}$$

18.1.3 The $\dot{\beta}$ equation

Expanding Eq 2-82, yields:

$$\dot{\beta} = \frac{1}{V}\left(\frac{F_{A_Y}}{m}cos\beta + \frac{F_{T_Y}}{m}cos\beta + gsin\Phi cos\Theta cos\beta - \frac{F_{A_Z}}{m}sin\alpha sin\beta - \frac{F_{T_Z}}{m}sin\alpha sin\beta - gcos\Phi cos\Theta sin\alpha sin\beta - \frac{F_{A_X}}{m}cos\alpha sin\beta - \frac{F_{T_X}}{m}cos\alpha sin\beta + gsin\Theta cos\alpha sin\beta\right) + psin\alpha - rcos\alpha \quad \text{Eq 18-8}$$

Plugging Eq 2-83 to Eq 2-85 we get:

$$\dot{\beta} = \frac{1}{V}\left(\frac{\bar{q}S}{m}C_Y cos\beta - \frac{\bar{q}S}{m}C_Z sin\alpha sin\beta - \frac{\bar{q}S}{m}C_X cos\alpha sin\beta + gsin\Phi cos\Theta cos\beta - gcos\Phi cos\Theta sin\alpha sin\beta + gsin\Theta cos\alpha sin\beta - \frac{F_{T_Z}}{m}sin\alpha sin\beta + \frac{F_{T_Y}}{m}cos\beta - \frac{F_{T_X}}{m}cos\alpha sin\beta\right) + psin\alpha - rcos\alpha \quad \text{Eq 18-9}$$

Rearranging we get:

$$\dot{\beta} = \frac{1}{V}\left(\frac{\bar{q}S}{m}(C_Y cos\beta - (C_Z sin\alpha + C_X cos\alpha)sin\beta) + gsin\Phi cos\Theta cos\beta - gcos\Phi cos\Theta sin\alpha sin\beta + gsin\Theta cos\alpha sin\beta - \frac{F_{T_Z}}{m}sin\alpha sin\beta + \frac{F_{T_Y}}{m}cos\beta - \frac{F_{T_X}}{m}cos\alpha sin\beta\right) + psin\alpha - rcos\alpha \quad \text{Eq 18-10}$$

Using Eq 2-90 we get:

$$\dot{\beta} = \frac{1}{V}\left(\frac{\bar{q}S}{m}(C_Y cos\beta + C_D sin\beta) + gsin\Phi cos\Theta cos\beta - gcos\Phi cos\Theta sin\alpha sin\beta + gsin\Theta cos\alpha sin\beta - \frac{F_{T_Z}}{m} sin\alpha sin\beta + \frac{F_{T_Y}}{m} cos\beta - \frac{F_{T_X}}{m} cos\alpha sin\beta\right) + psin\alpha - rcos\alpha \quad \text{Eq 18-11}$$

Using Eq 2-92 we get:

$$\dot{\beta} = \frac{1}{V}\left(\frac{\bar{q}S}{m} C_{Y_{wind}} + gsin\Phi cos\Theta cos\beta - gcos\Phi cos\Theta sin\alpha sin\beta + gsin\Theta cos\alpha sin\beta - \frac{F_{T_Z}}{m} sin\alpha sin\beta + \frac{F_{T_Y}}{m} cos\beta - \frac{F_{T_X}}{m} cos\alpha sin\beta\right) + psin\alpha - rcos\alpha \quad \text{Eq 18-12}$$